

MSc thesis

Argon Laser-Plasma Thruster

Design and Test of a Laboratory Model

Emmanuel Duplay



Space Track
Faculty of Aerospace Engineering

Master's thesis

Argon Laser-Plasma Thruster

Design and Test of a Laboratory Model

Submitted to fulfill the requirements of the degree of Master of Science at the Delft University of Technology

Emmanuel Duplay
5468515
MSc Aerospace Engineering
Space Track
Space Exploration Profile

January 30, 2024

The work in this thesis was performed in part at the Mechanical Engineering Department of McGill University, in Montreal, Canada.

Internal supervisor:	Ir. B.T.C. Zandbergen	Delft University of Technology
External supervisor:	Prof. A.J. Higgins	McGill University
Thesis committee :	Prof. A. Menicucci	Delft University of Technology
	Prof. A. Cervone	Delft University of Technology



The code used for this project (including the \LaTeX source) is available on
<https://github.com/eeduplay/MScThesis> (latest)
<https://doi.org/10.4121/e0d30ad2-cdca-45a6-84d6-34d95db49b2c> (archive)

All experimental data associated with this thesis are available on
<https://doi.org/10.4121/04ad8110-e3c4-4971-99ce-8a6c537166d6>
This includes the list of LSPs, high-speed footage, pressure data, and spectra.

Cover image: Composite photograph approximating (with some artistic license) the appearance of the laser-thermal thruster model operating in the laboratory.

PREFACE

My interest in laser-thermal propulsion began long before I started this master's thesis. It was in fact my introduction to academia, through an undergraduate research experience. This experience proved to be quite successful, as it led to my first journal publication in 2022, which demonstrated the potential of this concept for rapid-transit missions to Mars.

By that point, I had already begun my master's degree at TU Delft, in search of new fields of study that would pique my interest. While Delft allowed me to learn more than I could have ever hoped about all fields of astronautical engineering, none captivated my imagination quite like laser-thermal propulsion. I was thus excited to have the opportunity to return to my alma mater to kick-off laser-sustained plasma and laser-thermal propulsion experiments at McGill. Although the results of this project are a little different from what I had first (perhaps too ambitiously) envisioned, I am proud of the progress made within a year, and I am confident that my work will provide a valuable base that future students can build upon.

My name may be alone on the cover page, but this thesis could not have been completed without the valuable support of my mentors, my colleagues, my friends, and my family. I would first like to thank Andrew Higgins, who provided all the guidance and support I could have hoped for, both during my undergraduate studies and this thesis project. Thank you to Barry Zandbergen for supervising me through this project and providing valuable insight and comments which greatly improved the quality of this thesis. Thank you to all the attendees of my midterm review, who all provided useful advice on this project's modeling and experimental work. Thank you to my parents, who have done their best to support me during my studies and especially while writing this report. Thank you to John Kokkalis for offering your apparatus for this experiment. I also want to thank all the students of the Interstellar Flight Experimental Research Group (and a few other labs) for making all of this experience not only enjoyable but also memorable—I would likely have lost my mind otherwise. Last but not least, I want to thank Gabriel and Siera for their hands-on help and for putting up with me for months. I could not have asked for better research partners, and I hope you take this project beyond all our expectations.

As I write these lines, Gabriel is hard at work preparing a conference presentation (cited below) on the work discussed here. Good luck!

G. R. Dubé *et al.*, "Laser-Sustained Plasma for Deep Space Propulsion: Initial LTP Thruster Results," in *2024 AIAA Science and Technology Forum and Exposition (AIAA SciTech Forum)*, Orlando, FL: American Institute of Aeronautics and Astronautics, Jan. 2024

Contents

Preface	ii
List of Figures	vii
List of Tables	viii
Nomenclature	ix
Abstract	xi
1 Introduction	1
2 Background	4
2.1 Working principle	4
2.2 Laser-Sustained Plasma	7
2.3 Past facilities	10
2.3.1 University of Illinois Urbana-Champaign (UIUC)	10
2.3.2 University of Tennessee Space Institute (UTSI)	11
2.3.3 Japanese experiments	11
2.3.4 Other LSP facilities	13
2.4 Takeaways and research objectives	15
3 Facility design	16
3.1 Existing hardware and OTS components	16
3.1.1 Laser system	17
3.1.2 Instrumentation	18
3.2 Design process	21
3.2.1 Test section	21
3.2.2 Laser window mount	24
3.2.3 UV-grade side windows	25
3.2.4 Spark-ignition system	26
3.2.5 Thrust stand	29
3.3 Integration and test	30

3.3.1	Pressure testing	30
3.3.2	Laser power tests	32
3.3.3	Thrust stand testing	34
3.3.4	System integration	35
4	Modelling	39
4.1	Absorption	39
4.2	LSP size estimate	43
4.3	Test-section heating	45
4.3.1	Failed ignition	46
4.3.2	Successful ignition	46
4.4	Thrust modelling	49
4.4.1	Cold-flow conditions	50
4.4.2	Hot-fire conditions	52
4.4.3	Limitations	54
5	Experiments	56
5.1	Preliminary ignition tests	57
5.1.1	Spark ignition	57
5.1.2	Wire ignition	60
5.1.3	Early LSP observations	60
5.2	Power threshold	64
5.2.1	Methodology	64
5.2.2	Results	64
5.3	Laser Absorption	68
5.3.1	Methodology	68
5.3.2	Results	68
5.4	Heat deposition	70
5.4.1	Methodology	70
5.4.2	Results	71
5.5	Spectroscopic temperature measurement	76
5.5.1	Boltzmann plot method	77
5.5.2	Temperature calculation	78
5.6	Flowing experiments	80
6	Conclusion and further work	83
6.1	Further work	85
	References	87
A	YLR-300/3000-QCW-MM-AC calibration report	96
B	P30 collimator calibration report	103
C	Test section apparatus drawings	105
D	Laser window mount drawings	112
E	Instrumentation datasheets and calibration reports	121

F	Calculation examples	125
F.1	Absorption coefficient	125
F.1.1	Electron density calculation	125
F.1.2	Absorption coefficient	126
G	LSP shot procedure	129
H	Laser Pulse Shapes	134
I	Properties of relevant substances	135

List of Figures

1.1	Comparison of various space propulsion systems	2
1.2	DEP architecture for an LTP mission to Mars with a 45-day transit time. . . .	3
2.1	Overview of a CW laser-plasma LTP system	6
2.2	Theoretical specific impulse attained for a given hydrogen temperature . . .	7
2.3	Dependence of LSP on pressure and flow velocity	9
2.4	UIUC experimental configurations	10
2.5	UTSI LSP apparatus	12
2.6	University of Tokyo LSP apparatus	13
2.7	Recent argon LSP generator designs	14
2.8	IB absorption coefficient for CO ₂ - and fiber-laser radiation	14
3.1	LTP Experiment subsystems	17
3.2	Laser system used for this project	18
3.3	Laser ionization test section	22
3.4	Laser window mounts	25
3.5	Transmission profile of JGS1 fused silica	26
3.6	Spark-ignition circuit diagram	27
3.7	Exploration of spark-gap size in argon with Paschen's law	28
3.8	Test section mounted on the delivered thrust stand	29
3.9	Pressure leak tests on the test section	31
3.10	CW laser output power test results	33
3.11	Qualitative diagram of laser power losses throughout the test section. . . .	34
3.12	Diagram of cable system used to relieve thruster weight from the thrust stand	35
3.13	Signal timing diagram of an experimental run	36
3.14	Overview of the experimental setup	38
4.1	Computation of electron density n_e of argon	41
4.2	Calculation of the Coulomb logarithm, 10 bar	42
4.3	Inverse bremsstrahlung absorption coefficient of argon, 1070-nm radiation .	43
4.4	LSP sizing model	44
4.5	Thermodynamic properties of argon at 10 bar	44
4.6	LSP dimension estimate for 30 J pulse, assuming conical volume	45
4.7	Effect of pulse LSP on test-section conditions	48
4.8	Expected flow temperature at nozzle inlet	49
4.9	Cold gas thruster parameters	51
4.10	Change in operating parameters between cold (1) and hot (2) flow	53
4.11	Thrust and exhaust velocity, hot-fire conditions	54

5.1	Static configuration of the test section	56
5.2	Composite photos made during a typical spark–laser alignment procedure .	58
5.3	High-speed footage frames of first successful LSP ignition	59
5.4	Third successful LSP test ignited by arc discharge	59
5.5	LSP ignition via tungsten wire	61
5.6	LSP growth throughout 10-ms-laser pulse	63
5.7	Typical stepped-pulse profile: 05L33_15	65
5.8	Pressure-Power LSP threshold exploration	67
5.9	LSP adjusting to step-down in power	67
5.10	Estimated energy absorption of LSP, 20 bar	69
5.11	Length estimation of LSP	69
5.12	Denoising of pressure data and comparison to other sources of heat	71
5.13	Effect of varying initial pressure on pressure rise resulting from LSP	72
5.14	Effect of varying laser pulse energy on pressure rise resulting from LSP	73
5.15	Detailed analysis of pressure rise profile	74
5.16	Heat-deposition efficiency of LSP	75
5.17	Major losses in the overall heat deposition. Diagram to scale.	76
5.18	Detection of Ar I emission lines in LSP50_X7 in static argon	77
5.19	Boltzmann plots of selected LSP sustained at 3 kW	79
5.20	Flowing configuration of the test section	80
5.21	Comparison of LSP under forced flow (top) and static LSP (bottom)	81
5.22	Pressure change and heat-deposition efficiency in flowing LSP	82

List of Tables

3.1	Summary of nominal laser specifications	17
3.2	Summary of nominal laser power meter specifications	19
3.3	Top-level design requirements for the LTP laboratory model	21
3.4	Verification of LTTLM requirements for the cavitation apparatus	23
3.5	Top-level design requirements for the thrust stand	30
3.6	Pressure leak tests on test section	32
3.7	Optical power loss test summary	34
3.8	Timeline of one experimental run	36
4.1	Operating scenarios for the LTTLM	49
4.2	Cold-flow exhaust velocities	52
5.1	Overview of experiments/tests, goals, and success criteria	57
5.2	LSP energy absorption data	68
5.3	Ar I transitions used to generate Boltzmann plot	78
5.4	Specifications for choked orifice nozzles used for flowing tests	81
H.1	Programmed pulse specifications	134
I.1	Thermodynamic and mechanical properties of selected substances	135

Nomenclature

Physical Constants

Symbol	Name	Value	Unit	Ref.
c	Speed of light in a vacuum	$2.997\,92 \times 10^8$	m s^{-1}	[1]
e	Elementary charge	$1.602\,18 \times 10^{-19}$	C	[1]
g_0	Standard gravity	9.806 65	m s^{-2}	[1]
\hbar	Reduced Planck constant	$1.054\,57 \times 10^{-34}$	J s	[1]
k_B	Boltzmann constant	$1.380\,65 \times 10^{-23}$	J K^{-1}	[1]
m_e	Electron mass	$9.109\,38 \times 10^{-31}$	kg	[1]
N_A	Avogadro's number	$6.022\,14 \times 10^{23}$	mol^{-1}	[1]
R_u	Universal gas constant	8.314 46	$\text{J K}^{-1} \text{mol}^{-1}$	[1]
ϵ_0	Permittivity of free space	$8.854\,19 \times 10^{-12}$	F m^{-1}	[1]

Abbreviations

CW	Continuous-Wave
DEP	Directed-Energy Propulsion
FDL (McGill)	Fluid Dynamics Laboratory
IB	Inverse Bremsstrahlung
IFERG	Interstellar Flight Experimental Research Group
LSP	Laser-Sustained Plasma
LTP	Laser-Thermal Propulsion
LTTLM	Laser-Thermal Thruster Laboratory Model
NEP	Nuclear-Electric Propulsion
NTP	Nuclear-Thermal Propulsion
OTS	Off-The-Shelf
SEP	Solar-Electric Propulsion
STP	Solar-Thermal Propulsion
TTL	Transistor-to-Transistor Logic

Latin symbols

A	Einstein coefficient, or area
A	Empirically derived parameter A for Paschen's law
B	Empirically derived parameter B for Paschen's law
c_p	Specific heat of enthalpy
c_v	Specific heat of internal energy
D	Diameter
d	Distance
E	Energy
g	Degeneracy of atomic energy level
h	Enthalpy
I	Local laser flux
I_{sp}	Specific impulse
K_m	Choked-mass-flow parameter

NOMENCLATURE

k	Thermal conductivity
L	Leak rate
ℓ	Relative power loss
m	Mass
\mathcal{M}	Molar mass
N	Number of moles
N_f	F-number
n	Number density
n_{sp}	Laser setpoint
P	Power
p	Pressure
Q	Heat
q	Charge
R_g	Specific gas constant
r	Radius
T	Temperature
T_E	Temperature in energy units
t	Time
V	Volume
V_B	Breakdown Voltage
v	Velocity
Z	Ion charge state
\mathcal{Z}	Partition function

Greek symbols

α	Radiation absorption coefficient
γ	Specific heat ratio
γ_{se}	Secondary-electron-emission coefficient

ϵ	Integrated line emission intensity
η	Efficiency
Λ_{th}	Thermal DeBroglie wavelength
λ	Wavelength
ν	Frequency
ρ	Density
ρ_{min}	Electron-ion collision minimum impact parameter
σ	Normal stress

Subscripts

a	Ambient
c	Thrust chamber
e	Electron
ex	Exhaust
eq	Equivalent (exhaust velocity)
f	Focusing length
i	Lower atomic energy level
in	Input
ion	Ionization
k	Upper atomic energy level
l	Lens
m	Measured
r	Laser receiver, or reference
T	Thrust
t	Throat
w	Window

ABSTRACT

A laser-sustained plasma (LSP) generator capable of operating as a laser-thermal thruster was designed and tested. The apparatus was powered by a 3-kW 1070-nm fiber-optic laser and was operated with argon gas at pressures of 3 bar to 20 bar. This thesis documents its design process and early test results. The laser absorption, radiated spectrum, and change in static pressure were recorded, and high-speed video footage of the LSP was acquired. Of special interest is the heat-deposition efficiency into the working gas resulting from LSP ignition, which was estimated by tracking the pressure change in the test section. Laser transmission through the absorbing plasma was also measured to estimate the magnitude of two energy loss mechanisms: incomplete laser absorption and radiation of heat to the walls of the test section. Characterizing and minimizing these losses would be critical in the realization of a practical and efficient laser-thermal propulsion (LTP) thruster, as most of the laser energy should be deposited as heat in the propellant to maximize thrust chamber temperature and therefore thruster specific impulse.

This report first introduces the concept of laser-thermal propulsion, highlighting its potential as a high-specific impulse, high-thrust deep-space propulsion system competing with proposed nuclear-thermal thruster concepts. A brief summary of past literature on LTP is provided: first imagined in the 1970s, and studied intensively over the following two decades along with the physical mechanism powering the concept—laser-sustained plasma. Although LSP has been tested experimentally before, most studies used CO₂ lasers operating at 10.6 μm , while current thinking on directed-energy propulsion favors 1.06- μm fiber lasers. Furthermore, previous LTP prototypes have demonstrated the concept without attempting to optimize thruster performance to a level that could be deemed competitive. Updating experimental research with fiber-optic lasers and resuming LTP studies with the aim to maximize thruster performance is thus identified as a research gap. This study aimed to design a facility to study LSP and LTP in the lab and to establish a baseline heat-deposition efficiency measure against which further improvements and facility iterations can be compared.

The design process of the test facility is first documented in detail, discussing available laser equipment and diagnostics apparatus. Top-level requirements for the test section and thrust stand are given. The apparatus built for an unrelated experiment and left unused is identified as a suitable candidate for retrofitting as an LSP generator, speeding up the realization of an experimental setup. Retrofitting, integration, test, and calibration activities are all described in detail. A discussion of LSP absorption modelling is given to provide a deeper understanding of the relevant parameters affecting ab-

sorption, namely laser wavelength and gas pressure. Simple models for LSP sizing, heat deposition in the test section, and expected thrust performance are also presented.

Then follows a summary of the results obtained from early experiments with the facility, starting with exploratory ignition experiments. The spark-ignition system considered for use in the project was more difficult to use than expected, as successful and reliable ignition was found to require a consistent arc path, which was not the case with the final spark-plug design. LSP was nevertheless ignited successfully using this method a few times, allowing some measure of its laser-absorption, found to be 79% on average at 20 bar. Ignition by thermionic emission from a tungsten wire was found to provide much more consistent ignition, although this prevented the measurement of transmitted laser energy. Power threshold experiments commonly performed in LSP literature were reproduced, showing that this LSP facility achieved lower threshold powers than several past studies, with LSP sustained at 5 bar with as low as 600 W of laser power, 40% less than would be estimated from past literature. Heat deposition into the working gas was estimated by tracking the change in static pressure inside the test section, then using the ideal gas law to relate it to the added heat. Heat-deposition efficiency appears to be consistent across pressures at approximately 15%. Finally, spectroscopic temperature measurement was attempted using the Boltzmann plot method, but the analyses have not yielded realistic temperature estimates, likely due to methodology issues.

Some flowing/thrust experiments were also attempted. Unfortunately, the retrofitted apparatus was not optimized for thruster operation and its excessive weight was a major obstacle to thrust measurement. The thrust stand designed by a collaborating team of students was not able to provide consistent thrust readings. Pressure and spectral data was acquired for LSP in bulk flow velocities ranging from 0.88 m s^{-1} to 1.8 m s^{-1} , but these experiments exhibited little to no difference from the static case. The growth and size of the LSP was observed to change under flowing conditions: as seen in the literature, the LSP front speed was slower and the tail extended further downstream, resulting in an LSP located closer to the laser focus.

Although the resulting laboratory model is not an optimized LTP thruster prototype, the facility provides a platform upon which future, more targeted, and more rigorous experiments can be performed, following up on the results presented in this report. The lessons learned in designing the facility and early tests will be invaluable in the design of the next iteration of laser-thermal thruster laboratory models at McGill University.

Chapter 1

Introduction

Despite the recent progress made by the commercial space sector in facilitating access to Earth orbit, piloted space missions have remained largely unchanged in terms of transit time and propulsion technologies. Current systems used for piloted missions (i.e., chemical propulsion) have a low fundamental limit to the specific impulse delivered in a rocket motor: the RL10B-2 hydrogen–oxygen vacuum-optimized engine is a flight-proven rocket motor with a stated specific impulse of 465.5 s [2]. Despite deriving from a design conceived in the late 1950s (Bilstein [3]), this is *still* the highest specific impulse chemical thruster ever used in practice.

The expansion of human activities beyond Earth’s sphere of influence will likely demand the development of space propulsion systems providing high thrust and propellant efficiency. Such systems would facilitate rapid transit of crew and cargo across the solar system. In addition to the usual convenience and economic benefits, faster transit times would reduce astronaut exposure to the harsh radiation environment of interplanetary space (Berger *et al.* [4]), significantly mitigating the health risk factors of crewed missions.

Laser-Thermal Propulsion (LTP) is a promising concept for such a propulsion system. Initially conceived in the 1970s by Kantrowitz [5] among many other forms of Directed-Energy Propulsion (DEP), this concept consists of beaming laser power to a spacecraft, which then uses it to heat up propellant. This method of heating could potentially raise the bulk propellant temperature¹ by an order of magnitude compared to chemical propulsion, resulting in a significant improvement in specific impulse, as shown by Nored [6]. Combined with reasonably high thrust, this places LTP on par with or better than Nuclear-Thermal Propulsion (NTP) concepts, as seen on the visual comparison² in Figure 1.1. LTP was thus the subject of significant research efforts in the 1970s and 1980s for launch vehicle and orbital tug applications, as the monolithic nature of available CO₂ lasers made it impractical to create

¹“Average” temperature—resulting temperature if the heat in the flow is distributed uniformly

²With one caveat: these systems use different propellants, which, all things equal, will result in different performance. The examples represent the state-of-the-art of these propulsion technologies.

1. INTRODUCTION

optical aperture sizes (e.g., the output lens diameter) allowing ranges beyond Low-Earth Orbit. Research into this concept has seen renewed interest in the last few years thanks to the development of low-cost, scalable, and modular fiber-laser technologies and proposals by Lubin [7] to use such lasers for interstellar propulsion. Indeed, Lubin shows that fiber-optic lasers can be phase-locked together to act as a single optical element, allowing the modular and inexpensive construction of large laser arrays. The shorter wavelength ($1.06\ \mu\text{m}$ vs. CO_2 lasers' $10.6\ \mu\text{m}$) and ability to construct meter- to kilometer-scale arrays expands the applications of directed-energy propulsion to interplanetary and interstellar missions: the focusing range d_f is proportional to D_e/λ , where D_e is the emitter diameter and λ is the laser wavelength.

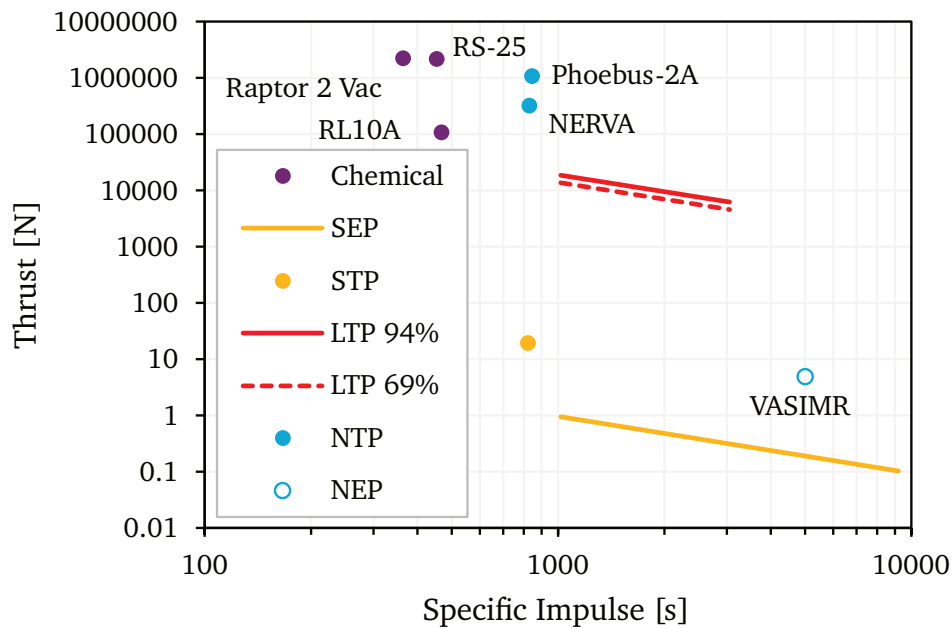
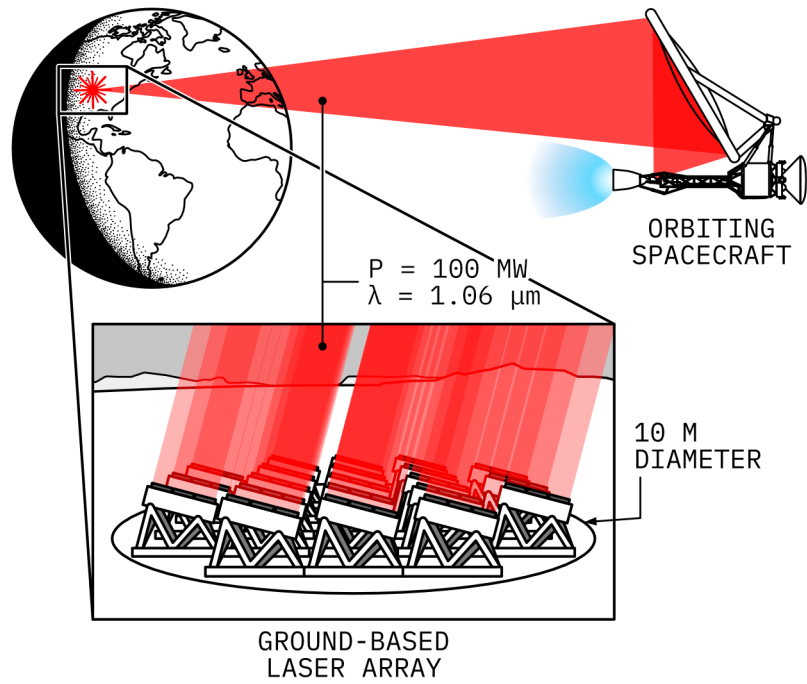


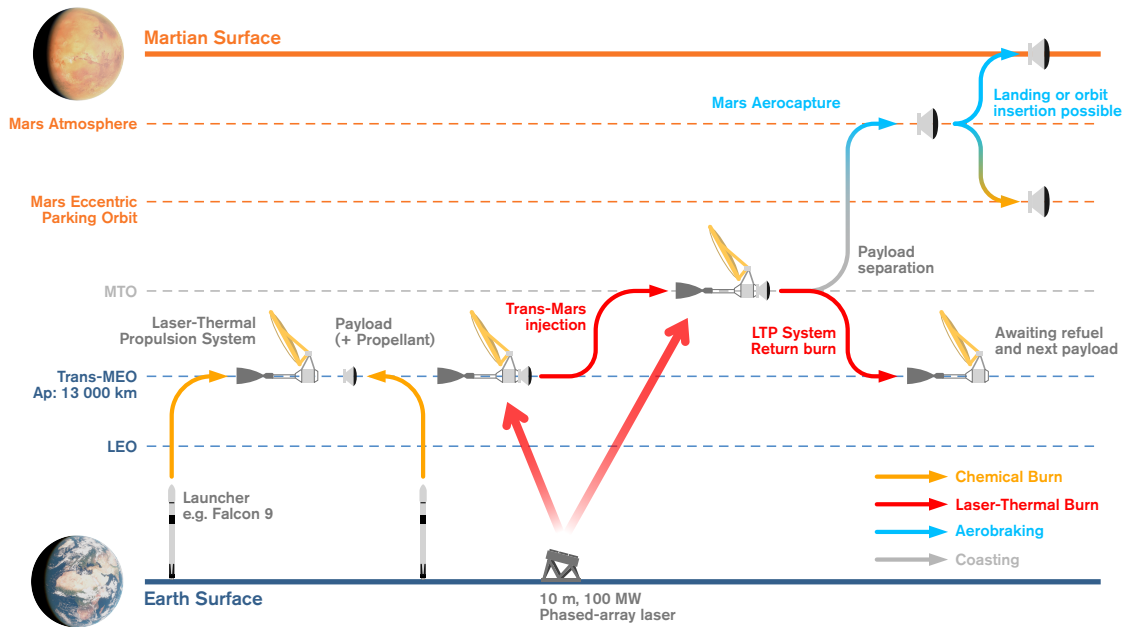
Figure 1.1: Comparison of various space propulsion systems based on their specific impulse and thrust. References: Chemical [2, 8, 9], Solar-Electric Propulsion (SEP) [10], Solar-Thermal Propulsion (STP) [11], LTP [12, 13], NTP [14], Nuclear-Electric Propulsion (NEP) [15]

The work done in this thesis is a collaboration between TU Delft and McGill University to support the research efforts performed at McGill's Interstellar Flight Experimental Research Group (IFERG) on LTP. Duplay *et al.* [12] considered the application of LTP for a 45-day transit to Mars, illustrated in Figure 1.2, showing that a ground-based 100-MW laser powering an LTP spacecraft could plausibly deliver a 1-ton payload to the planet for less than 1% of the propellant required by an equivalent mission powered by a chemical rocket engine. This study attracted significant attention, motivating the group to pursue further modelling and experimental research efforts. This Master's thesis documents the design of a Laser-Sustained Plasma (LSP) facility for propulsion applications, and reports preliminary data on LSP absorption, behavior in co-axial flow conditions, and thrust characteristics of this LTP thruster laboratory model.

1. INTRODUCTION



(a) Basic concept



(b) Concept of operations for a reusable LTP spacecraft (Duplay *et al.* [12])

Figure 1.2: DEP architecture for an LTP mission to Mars with a 45-day transit time.

Chapter 2

Background

To best understand the work done in this thesis, some background information on laser-thermal propulsion is provided in this chapter. This is an abridged version of the literature review [16] written before starting this thesis, which can be consulted for an in-depth study of past literature. The working principle of LTP will first be discussed, including a brief discussion of DEP and alternate concepts that also fall under the LTP category. A thorough discussion of LSP, the physics powering the laser-plasma LTP thruster, will then be given. Finally, an overview of the experimental work done on both LSP and LTP will be provided.

Although hydrogen is the preferred candidate for LTP propellant to maximize specific impulse (as implied by Equation 2.1), many LSP studies have also considered other gases, usually noble gases. Discussion of the literature will include such studies, specifically those on argon LSP, as it is the working fluid studied in this project. The rationale for choosing argon as propellant will be discussed at the end of this chapter, after stating research objectives derived from the findings of the literature review.

2.1 Working principle

LTP is a directed-energy propulsion concept, a class of propulsion systems where energy is beamed to a spacecraft, usually using a laser¹. This energy is then used for propulsion either directly or through an intermediate conversion process. This allows the spacecraft to forego much of its power and propulsion system mass, increasing its propellant or payload mass budget. Some applications of DEP, such as lightsails, even bypass the rocket equation altogether, making them a promising avenue for interstellar missions, as shown by Lubin [7]. Lubin proposes modular, scalable fiber-laser arrays operating at 1064 nm to beam the required MW to GW of power necessary to propel interplanetary and interstellar spacecraft. This specific laser wavelength transmits with virtually no losses through the atmosphere (Gemini Observatory [17]), and perturbations caused by atmospheric turbulence can be readily corrected using adaptive optics technology already in use in astronomy, as discussed by Eckel and Schall [18] and Hettel *et al.* [19]. The choice of fiber-pumped lasers for DEP is also driven by economics: Lubin [7] discusses that the cost and size of fiber-pumped laser

¹Theoretically, a fully-contained LTP system could be used aboard a spacecraft, but this would not leverage the main benefit of laser propulsion, i.e., high propulsion system power for a low mass penalty

amplifiers has been driven down exponentially thanks to the growing use of fiber-optics in the telecommunications industry. This affordability enables the practical, scalable, and modular construction of large and high-power laser arrays in a manner not possible for a single monolithic laser.

Laser-thermal propulsion itself encompasses several concepts where the laser is used to energize a propellant stored aboard the spacecraft. Kantrowitz [5] first proposed this idea as a way to reduce launch costs. Such concepts include pulsed concepts that ablate solid propellant or cause laser-supported detonations, as studied by Myrabo [20], or laser heat-exchanger systems, as proposed by Kare [21].

The present work focuses on continuous-wave (CW) laser-plasma propulsion, proposed by Nored [6] and studied in detail by Keefer [22]: as illustrated in Figure 2.1, a continuous laser is used to power a laser-sustained plasma (LSP)² core within a thrust chamber (Figure 2.1b). This plasma absorbs laser energy and redistributes it to the propellant gas via conduction and radiation. The heated propellant is then expelled through a high-area ratio nozzle, like any other vacuum-optimized thermal rocket engine. It should be highlighted that although the LSP can attain temperatures of 20 000 K to 30 000 K (Nored [6]), it is thought to be relatively small compared to the thrust chamber size. The heat from the LSP core is distributed to the cooler gas flowing past it, resulting in a bulk propellant temperature at the nozzle inlet of “only” 10 000 K (Duplay *et al.* [12]). As will be discussed further in Section 2.2, the LSP core’s position and size is easily controlled by the laser beam geometry (Keefer [22]), requiring no additional confinement mechanisms (such as the ones seen in fusion propulsion concepts) to separate the plasma from the chamber walls.

As alluded to in the Introduction, the key advantage of laser-thermal propulsion over chemical propulsion is its ability to deliver far greater exhaust velocities. Following from thermal rocket theory (Zandbergen [23]), the limiting exhaust velocity $v_{\text{ex, max}}$ of a thermal rocket motor depends on Equation 2.1, where γ is the specific heat ratio of the propellant gas, R_u is the universal gas constant, \mathcal{M} is the propellant molar mass, and T_c is the bulk chamber temperature.

$$I_{\text{sp, max}} g_0 = v_{\text{ex, max}} \propto \sqrt{2 \frac{\gamma}{\gamma - 1} \frac{R_u}{\mathcal{M}} T_c} \quad (2.1)$$

All other parameters being equal, a thermal rocket engine operating at a higher chamber temperature will thus have a greater limiting exhaust velocity. Chemical thrusters are fundamentally limited in their chamber temperature by the adiabatic flame temperature of their propellants’ chemical reaction. By comparison, an arbitrary amount of heat can theoretically be deposited via laser into a laser-thermal rocket engine (within thermal and structural limits). By decoupling the thermal input from the propellant choice, a laser-thermal rocket engine can readily attain bulk temperatures of up to 10 000 K at the nozzle inlet, resulting in a specific impulse³ of more than 1000 s with hydrogen propellant, as shown by Nored [6] in Figure 2.2.

Some practical issues with this concept do remain. Although it is well understood that the high propellant temperatures that could be achieved by LTP would result in 1000 s to 3000 s of specific impulse (with hydrogen), whether the heat deposited in the LSP can be

²This physical phenomenon is also referred to as *optical plasmatron*, *light spark*, *continuous optical discharge* (COD), or *laser-supported combustion* (LSC) wave in the literature.

³Unless otherwise stated, values of specific impulse reported in this thesis refer to *vacuum* specific impulse

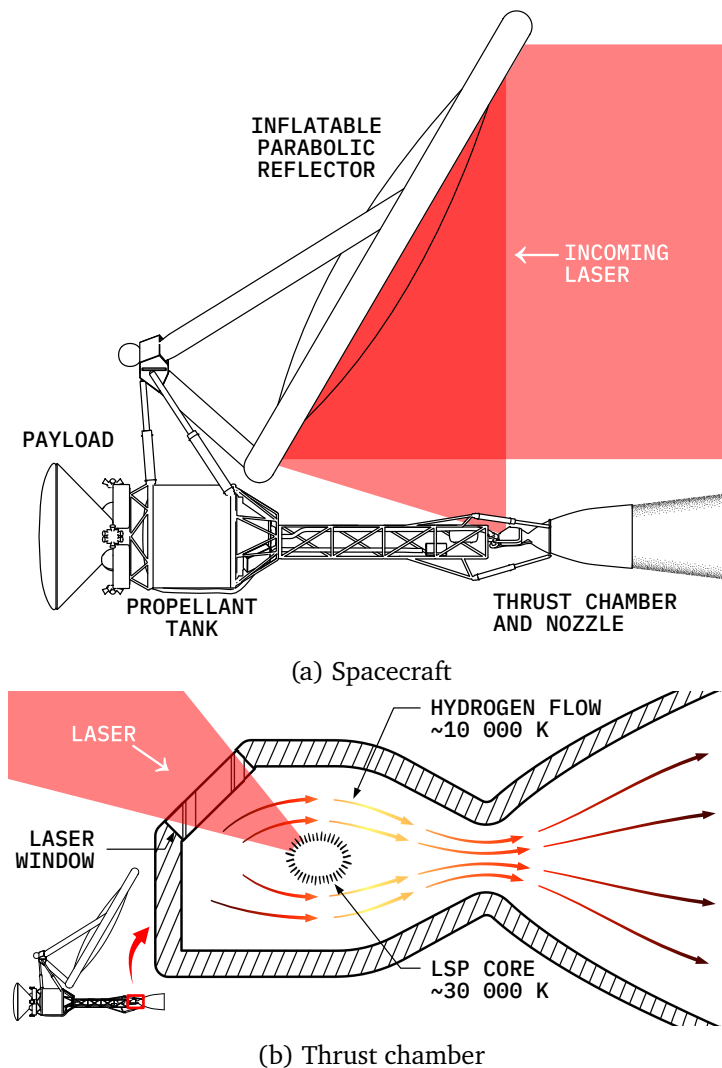


Figure 2.1: Overview of a CW laser-plasma LTP system, adapted from Duplay *et al.* [12]

transferred to all the propellant flow with minimal losses is a critical issue. This problem was studied in-depth by Shoji and Larson [13], who performed a thorough analysis of heat transfer within two LTP engines, proposing seeding the flow with carbon particles as a solution to reduce radiative heat losses to the chamber walls. Their analysis showed that such losses could be reduced to 4.5% of the input laser power for hydrogen seeded with 50% carbon (by weight). While this is promising, such a system has yet to be tested experimentally. Furthermore, as suggested by Equation 2.1, the introduction of higher molar-mass carbon particles is associated with a penalty in the resulting specific impulse: Shoji and Larson's models show a decrease in theoretical specific impulse of around 25%.

Cooling is also an issue. Even with the inclusion of carbon seeding, the magnitude of laser power considered for DEP (MW to GW) makes 4.5% of input power radiated to the thruster walls considerable. The propellant temperatures associated with high specific impulse are also far greater than the ones typically encountered by conventional thermal rocket engines, potentially necessitating new cooling strategies (Nored [6]). Thankfully, many of

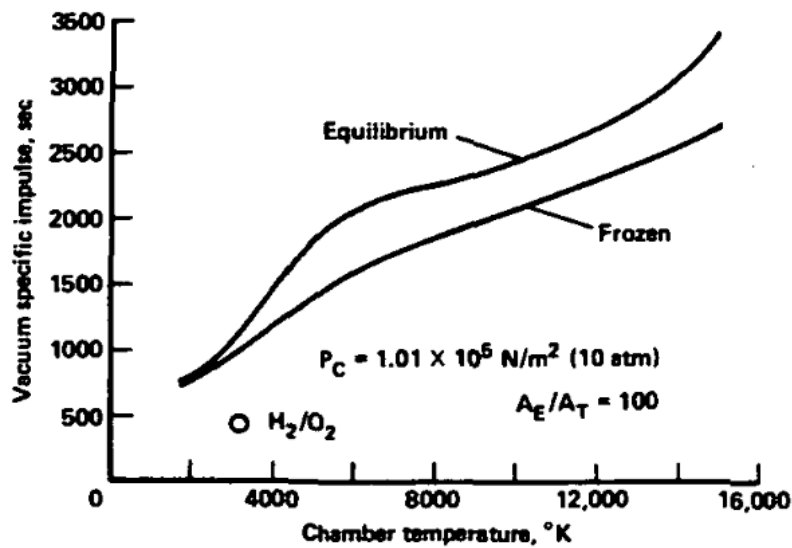


Figure 2.2: Theoretical specific impulse attained for a given hydrogen temperature at the nozzle inlet, by Nored [6]. The specific impulse is bounded by two cases: 1. The exhaust products maintain chemical equilibrium as they cool and expand through the nozzle; 2. The composition of the exhaust is frozen

these cooling issues are similar in nature and magnitude to those encountered in Gas-Core Nuclear Rockets (GCNR), a subtype of NTP. Kascak [24] discusses a hydrogen GCNR operating at temperatures and specific impulses of the same order of magnitude, suggesting that a combination of transpiration cooling and gas seeding would be sufficient.

2.2 Laser-Sustained Plasma

One might wonder why bother with plasma at all. If the laser radiation could be deposited evenly in the propellant flow, little to no mixing would be needed and peak temperatures would be lower. Unfortunately, the use of lasers to directly heat gaseous propellant has a major flaw: the gas might not absorb the specific laser wavelength at room temperatures. For instance, hydrogen only begins to absorb 10.6- μm radiation at around 10 000 K, as shown by Glumb and Krier [25]: “The paradox is that hydrogen cannot absorb any laser radiation unless it is already hot.” They were considering 10.6- μm radiation emitted by CO_2 lasers, but this statement also holds for the 1.06- μm wavelength emitted by fiber lasers. This is because these wavelengths do not match hydrogen’s resonance absorption bands, whereby radiation is absorbed in the rotational or vibrational modes of a molecule. For instance, Campargue *et al.* [26] show that there is a gap in the absorption bands of H_2 in the 917–1090 nm range. The main absorption mechanism in LSP is *inverse bremsstrahlung* (IB): free electrons absorb radiation across a continuous spectrum (as opposed to specific wavelengths) during collisions with ions in the plasma (Keefer [22]). Johnston and Dawson [27] showed that the radiation absorption coefficient α [m^{-1}] can be calculated with Equation 2.2, where Z is the ionic charge state ($=1$ for single-ionization), n_e is the electron density in cm^{-3} , ν is the radiation frequency, k_B is the Boltzmann constant, and T_e is the electron temperature in Kelvin. The product $k_B T_e$ should be expressed in eV. The Coulomb

logarithm $\ln \Lambda$ and the plasma frequency ν_p will be discussed in detail in [Chapter 4](#).

$$\alpha = \frac{7.8 \times 10^{-7} Z n_e^2 \ln \Lambda}{\nu^2 (k_B T_e)^{3/2}} \left(1 - \frac{\nu_p^2}{\nu^2} \right)^{-1/2} \quad [\text{m}^{-1}] \quad (2.2)$$

Since such free electrons are only present once gas has ionized (i.e., $n_e \gg 0 \text{ m}^{-3}$), absorption of 1.06- μm -wavelength radiation can only occur in plasma by IB for gases that do not exhibit 1.06- μm line transitions.

While this negligible absorption at room temperature poses a problem to initiate the LSP process, Raizer [28] theorized that once properly initiated, an LSP wave could be sustained in flowing gas. This was soon confirmed experimentally by Generalov *et al.* [29], who sustained a Xenon plasma using a 150-W CW CO_2 laser (i.e., 10.6- μm wavelength). In addition to showing the feasibility of LSP, Generalov *et al.* also noted that the chamber pressure affects the ease of maintaining an LSP wave: in their experiments, they failed to maintain it below 3 atm, and pressures above 4 atm were too unstable—the plasma had a tendency to die out. Generalov *et al.* gave no conclusive explanation of the phenomenon, suggesting only that combustion-instability effects could arise due to the asymmetry of the LSP observed beyond 4 atm. Since later experiments have shown that this asymmetry is not a guarantee for instability, it is unclear whether other factors such as beam geometry (Generalov *et al.* used a low f-number of 1.25) were responsible for this observed instability. Zimakov *et al.* [30] reports stable Xenon plasmas sustained beyond 20 bar with beam f-numbers ranging from 3 to 10.

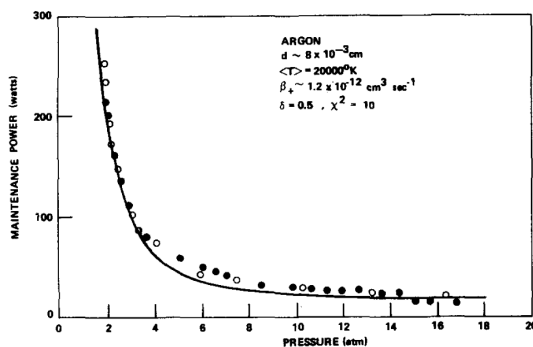
Once a plasma is initiated, its shape and position will stabilize at an equilibrium point where the local laser intensity is just sufficient to compensate for thermal losses of the plasma front (Keefer [22]). This state and its stability will be affected by beam geometry and flow conditions (Welle *et al.* [31]). Experiments by Fowler and Smith [32] show that a key aspect of beam geometry is the ratio of the converging beam's focal length to its initial diameter at the focusing lens, known as the f-number, often denoted f/N_f , where N_f is the f-number. Low f-numbers—i.e., short focal lengths with a wide initial beam diameter—produce stable plasmas which will remain close to the beam's focal point thanks to the rapid decrease in laser intensity, while the plasmas of high f-number optics will propagate away from the focus (Keefer [22]) and may be too unstable to be maintained continuously: Fowler and Smith have found that optical systems of $f/10$ and greater could not sustain a stable plasma.

Since the first model derived by Raizer, theoretical/numerical models of LSP saw progressive improvements, providing greater insight into the optimal conditions for plasma maintenance and laser absorption. Notably, Jeng and Keefer [33] developed a fully two-dimensional numerical model of hydrogen LSP in 1986 that suggests close to complete laser absorption can be achieved under certain conditions (3 atm of static pressure, 10 kW input power). This model also showed that radial velocity components of the flow were significant, meaning that the one-dimensional or quasi-two-dimensional models developed earlier, such as the one by Batteh and Keefer [34], were unsuitable for the analysis of LSP problems. Jeng and Keefer's model also allowed for the study of the effect of the laser wavelength on the resulting plasma, an analysis that was impractical to perform experimentally. Jeng and Keefer found that due to the gas absorption length's dependence on the applied electric field frequency, reducing the laser wavelength from 10.6 μm to 3.9 μm led to lower absorption rates and longer plasmas along the beam axis, due to the inversely proportional

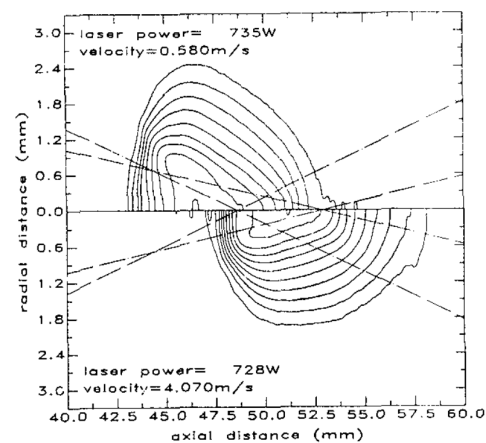
relation seen in Equation 2.2 (Keefer [22]). This is a highly relevant factor to consider for an experiment looking to study LSP using modern fiber lasers operating at 1.06 μm .

Several experiments on LSP have been performed since Generalov *et al.*'s first plasmatron in 1970. Early studies explored the parameter space for the successful maintenance of LSP, with specific attention given to the ranges of pressures and laser power (threshold power) required. Moody [35] provides a thorough exploration of this parameter space for argon plasmas sustained by a 10.6- μm laser, showing a $P \propto 1/p^2$ relation between the laser power P and the gas pressure p at < 10 atm, as shown in Figure 2.3a. In his study, the minimum pressure at which an LSP was achieved was 2 atm, for a laser power approaching 300 W. Higher pressures allow for a lower input power and can enable ambient atmosphere operation of a thruster, greatly simplifying experimental design. Similar experiments performed for other gases showed that the threshold power was typically greater for molecular gases (e.g., hydrogen) (Keefer [22]).

Another parameter affecting successful LSP maintenance is flow velocity, as shown by the studies of Welle *et al.* [31], Krier *et al.* [36], and Gerasimenko *et al.* [37]. While early experiments were typically performed in static gas, with natural convection being the only source of flow, the effect of forced convective flow was studied both for its benefits to the resulting LSP, and the application of LSP within a laser-thermal thruster. Welle *et al.* varied the flow speed from 0.4 m/s to 4.5 m/s in argon plasmas sustained by a 1 kW laser, measuring laser absorption and thermal radiation losses. They found that there are optimal pressure and flow speed conditions to maximize laser absorption, and that thermal radiation correlates with laser absorption. For pressures above 1.5 atm, increased flow speed appears to improve absorption compared to the static case. The authors suggest that the flow forced the plasma closer to the high-intensity laser focus, as seen in Figure 2.3b, improving absorption characteristics. In the case of Figure 2.3b, this translated to an improvement from 66% to 83%. Gerasimenko *et al.* found that in some cases, forced convection enables the maintenance of LSP under pressure and laser power conditions that would otherwise not allow it.



(a) Pressure dependence on required laser input power to maintain LSP in argon, reproduced from Moody [35]



(b) Temperature profile of argon plasmas at two flow velocities, reproduced from Welle *et al.* [31]. Intervals of 500 K with outer contour at 10 500 K.

Figure 2.3: Dependence of LSP on pressure and flow velocity

2.3 Past facilities

LSP and LTP experiments have been performed since the 1970s, with the very first LSP achieved by Generalov *et al.* [29], who used a CO₂ laser operating at 10.6 μm to sustain a Xenon LSP. The use of CO₂ lasers is common in the literature that followed, although the optical setups, diagnostics, working gases, and configurations of LSP and LTP experiments vary greatly. Facilities from three research groups will be discussed in particular, for their significant published research output and relevance to propulsion applications: the facility at the University of Illinois (late 1980s), at the University of Tennessee (late 1980s), and in Japan, where LSP experiments were performed as recently as 2019.

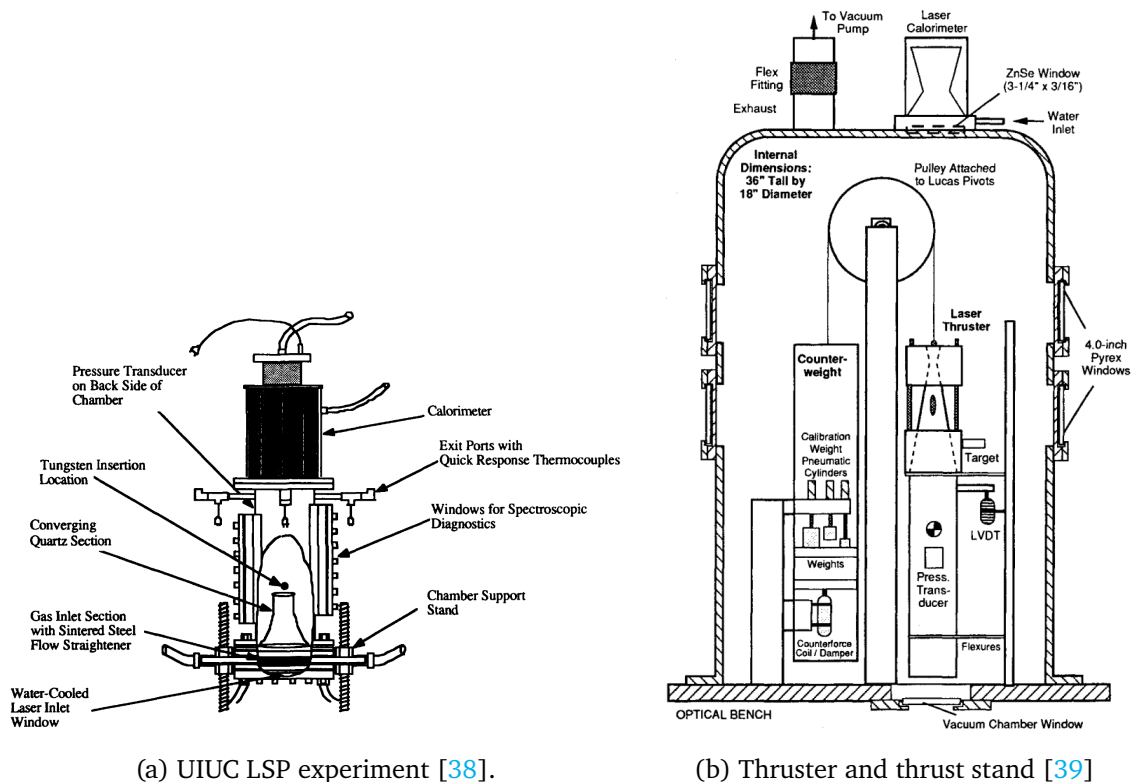


Figure 2.4: UIUC experimental configurations

2.3.1 University of Illinois Urbana-Champaign (UIUC)

This facility (depicted in Figure 2.4a) was operated principally by Krier and Mazumder and was designed to characterize the energy conversion ability of LSPs, using argon as a working fluid in most cases. According to Schwartz *et al.* [40], the LSP was sustained using a CO₂ laser with a maximum power of 10 kW. The beam was focused into the absorption chamber with an elaborate set of reflective optics that allowed the maintenance of dual-plasma geometry, which was thought to reduce radiative losses and improve heat retention. Initiation of the plasma was achieved using a tungsten rod as a solid target, which was removed directly after plasma initiation using a solenoid actuator. The working fluid was argon for most experiments, at 1.0 atm to 2.7 atm of gauge pressure. The absorption chamber design features devices to straighten and accelerate gas flow upstream of the LSP, facilitating the maintenance of a plasma at high flow rates, as turbulent flow were prone to

blow out the plasma. These design features include a flow straightener as the gas inlet section, and a converging quartz nozzle, which enabled the acceleration of the chamber flow without the need to manufacture a narrower thrust chamber, as the facility was initially designed for low flow speeds (< 2 m/s) (Krier *et al.* [38]). Most of their experiments revolved around laser absorption and thermal radiation, with little interest in thrust characteristics, so the heated gas exhaust was simply fed through exit ports. Nevertheless, experiments at this facility eventually led to the design and operation of a 10-kW-class thruster by Black *et al.* [39], with a 15:1 expansion ratio nozzle, achieving a specific impulse of up to 350 s, efficiencies near 40%, and thrust exceeding 3 N using hydrogen propellant. In their study, efficiency η is the thrust efficiency, calculated using Equation 2.3, based on a mass flow rate \dot{m} , thrust force F_T , and laser power entering the thruster P_{in} .

$$\eta = \frac{F_T^2}{2\dot{m}P_{in}} \quad (2.3)$$

Their thrust stand, like their LSP experiments, used a vertical configuration with a pulley and counterweight. The entire stand was encapsulated in a vacuum chamber. Thrust measurements were performed using a combination of a linear variable differential transformer, which senses the displacement of the thruster, and a counterforce coil, which uses the detected displacement and attempts to counteract it. The current supplied to the coil can be correlated to the thrust force F_T . This force could then be used with a mass flow rate \dot{m} measured with mass flow meters to compute specific impulse I_{sp} with Equation 2.4, which follows from thermal rocket theory.

$$I_{sp} = \frac{F_T}{\dot{m}g_0} \quad (2.4)$$

2.3.2 University of Tennessee Space Institute (UTSI)

The UTSI experiments were run using a 1.5-kW-class CO₂ laser. This facility is contemporary of the one at UIUC and shares similar design features, such as the vertical configuration and the converging gas inlet. Both facilities' absorption chambers are made in large parts out of quartz walls to allow for spectroscopic measurements to determine a spatial temperature distribution. In experiments performed by Keefer *et al.* [41], argon was used as the working fluid, at pressures ranging from 1.3 atm to 2.3 atm, and laser powers as low as 360 W. A significant feature of their facility is the presence of a specialized laser beam dump integrated within the converging exit nozzle.

2.3.3 Japanese experiments

The most recent LSP experiments have been performed at the University of Tokyo and Shizuoka University, studying not only the characteristics of LSP (Inoue *et al.* [42]), but also investigating its propulsion performance and its applications for replicating atmospheric re-entry conditions in wind tunnels (Matsui *et al.* [43]). The Japanese facility (illustrated in Figure 2.6a) took a different approach to that of UIUC and UTSI, opting for a horizontally configured thrust stand. Instead of running the entire thruster within a vacuum chamber, the nozzle was connected to a separate vacuum tank by means of an expansion joint, labelled Bellows in Figure 2.6a. This joint allowed the thruster to exhaust to vacuum conditions with reduced complexity and without preventing the thruster from applying a force to

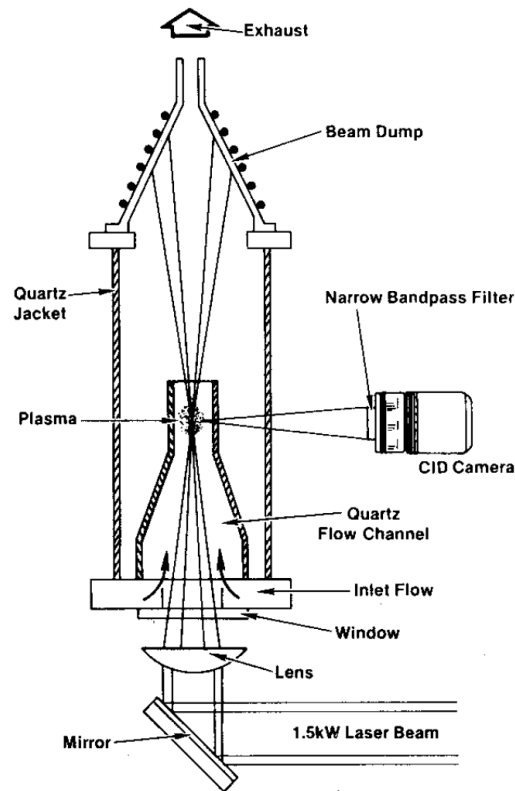


Figure 2.5: UTSI LSP apparatus [41]

the load cell, as would be the case with a rigid connection to the vacuum tank. The Tokyo research group performed experiments using a variety of working gases, laser powers, and plasma initiation methods. Matsui *et al.* [44] even performed experiments with disk, fiber, and diode lasers, a major change from the traditional use of CO₂ lasers. In addition to emitting wavelengths of 1030, 1070, and 940 nm, respectively, these lasers also offer improved energy efficiency, more compact form-factors, and easier maintenance compared to CO₂ lasers (Matsui *et al.* [44])—all relevant factors for the development of DEP and LTP. These advantages do come at the cost of reduced IB absorption coefficients at comparable pressures, as discussed by Matsui *et al.*

The Japanese LSP chambers generally follow a similar design as those of UIUC and UTSI, i.e., a cylindrical section followed by a converging-diverging nozzle. However, they do not feature some of the additional flow control devices seen in the other facilities, such as the converging gas inlet channel. Instead, it appears many of their LSPs are maintained just downstream of the cylindrical section, which then allows the flow to naturally develop before it reaches the plasma. The gas inlet is also placed close to the nozzle, forcing the gas to flow between the internal and external walls of the thruster before entering the main chamber near the laser window, acting as a regenerative cooling system. The LSP's axial position could be controlled by moving the laser focusing lens using a one-axis stage. The thruster also features a two-stage converging nozzle, with a sub-chamber in which the LSP is moved to after initiation, resulting in improved thrust levels (Toyoda *et al.* [45]). This is likely due to the improved absorption ability of LSP at higher flow speeds observed by Welle *et al.* [31].

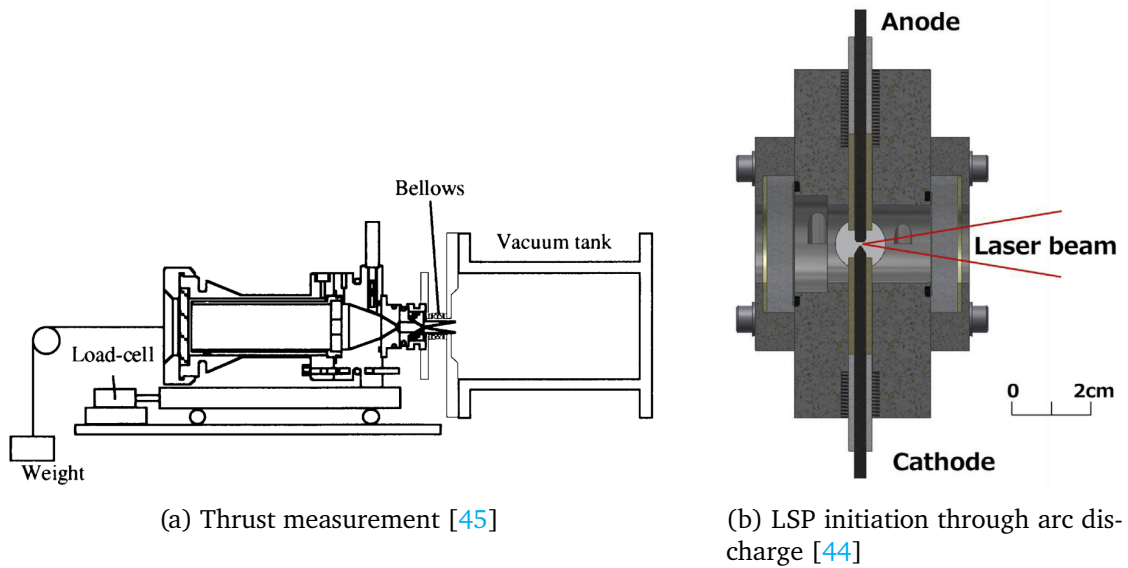


Figure 2.6: University of Tokyo LSP apparatus

The thrust measurement method used by Toyoda *et al.* [45] is also considerably simpler than the implementation used by Black *et al.* [39]. The thruster is mounted on low-friction linear rails and placed in contact with a load-cell. Weights on a pulley are used to balance the initial loads on the thruster. When operating the thruster to vacuum exhaust, the spring constant of the expansion joint was taken into account and compensated for. Furthermore, the motor was first run as a cold-gas thruster, using this initial thrust level as a reference to quantify the effect of the LSP. Efficiency was measured differently than in UIUC experiments, using Equation 2.5 [45]⁴, to separate the effect of the LSP from the baseline cold thrust $F_{T, \text{cold}}$. This provides a more meaningful measurement of the energy-conversion efficiency of LSP for propulsion applications.

$$\eta = \frac{F_{T, \text{hot}}^2 - F_{T, \text{cold}}^2}{2\dot{m}P_{\text{in}}} \quad (2.5)$$

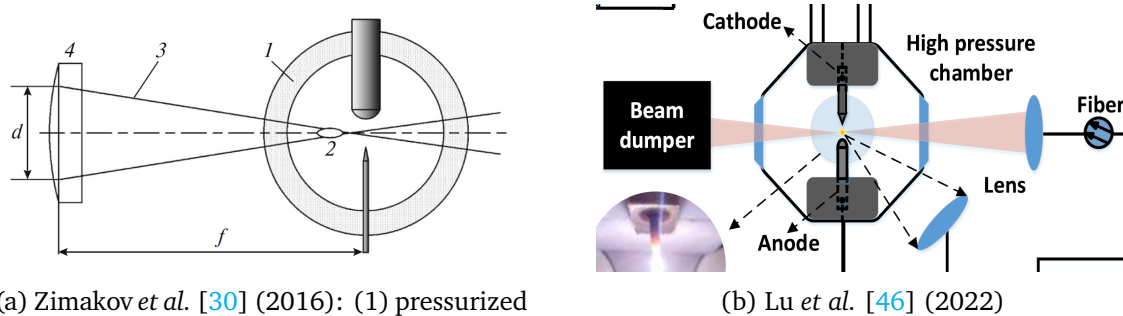
Two methods of plasma initiation were used throughout their experiments. Early thruster studies used a tungsten rod in the same manner as Schwartz *et al.* [40] at UIUC. A later study by Matsui *et al.* [44] used an arc discharge at the laser focus point, seen in Figure 2.6b. This solid-state method of plasma initiation is attractive for its mechanical simplicity and its ability to quickly react to control inputs compared to solenoid-actuated ignition rods.

2.3.4 Other LSP facilities

In addition to the LTP experiment described above, two recent experimental studies are considered for comparison with this project: those of Zimakov *et al.* [30] and Lu *et al.* [46], pictured in Figure 2.7. While they do not study LSP for thrust applications, they are of interest as they are some of only a few experiments using 1.06- μm fiber lasers to sustain plasma in argon, like in this project. In addition, both experiments appear to successfully

⁴The cited reference appears to have a typographical error, as the units are inconsistent. This equation can be derived from the conventional thrust efficiency equation, assuming a constant mass flow rate.

use an arc discharge for LSP ignition, which differs from much of the older experimental literature.



(a) Zimakov *et al.* [30] (2016): (1) pressurized bulb, (2) LSP, (3) laser beam boundaries, (4) lens with focal length f

(b) Lu *et al.* [46] (2022)

Figure 2.7: Recent argon LSP generator designs

Zimakov *et al.* [30]'s investigation focuses on determining the power necessary to sustain a steady argon and Xenon LSP, providing a simple model to plot this power threshold in terms of gas pressure, using experimentally determined parameters. Comparing their power threshold data with that of Moody [35] shows a drastic increase in required laser power for similar pressures, going from around 50 W to 1000 W at 6 bar, due to the change of laser wavelength from $10.6 \mu\text{m}$ to $1.07 \mu\text{m}$. This can be expected due to the reduced IB absorption coefficient, as seen in Equation 2.2 and Figure 2.8. They also attempt to determine plasma temperature by comparing the continuum emission spectrum of the LSP with the predicted spectrum of a plane slab plasma of comparable dimensions, approximating the LSP temperature to be 15 000 K for laser powers ranging from 65 to 230 W at 22 bar.

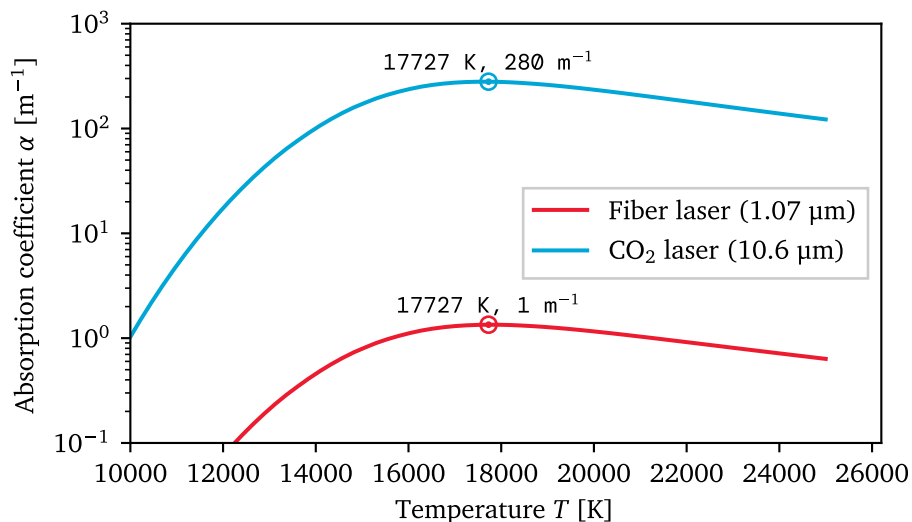


Figure 2.8: IB absorption coefficient at 1 bar for CO₂- and fiber-laser radiation

Lu *et al.* [46] performed in-depth spectroscopic analysis to determine plasma parameters, namely temperature and electron density. By using a line-to-continuum spectral analysis method, they estimated the LSP temperature to be 13 000 K (13 bar, 200 W).

2.4 Takeaways and research objectives

Research on LTP and LSP, beginning in the 1970s, suggest that LTP has a great potential as a high-efficiency, high-thrust propulsion concept with performance rivaling that of NTP systems. The use of ground-based laser arrays to transmit power virtually eliminates the power-generation subsystem mass from a spacecraft, enabling it to perform high-delta- v maneuvers in a shorter timespan than equivalent systems using on-board power. Although concerns regarding laser tracking, thrust chamber cooling, and engine efficiency present engineering challenges, no fundamental issues have been identified. Extensive literature on LSP sustained by CO₂ lasers exists and have shown promising results in terms of laser absorption by the LSP, one of the major potential loss factors for an LTP system: very high absorption was experimentally achieved under a variety of conditions. On the other hand, heat deposition from the LSP into the surrounding cold propellant is far less efficient, but potential solutions have been proposed, such as seeding the propellant flow with carbon or tungsten particles to improve radiative absorption.

LTP thruster laboratory models have been operated, but not since the early 2000s, never with fiber lasers, and some of the radiative absorption strategies mentioned earlier have yet to be tested to improve thrust efficiency. Recent research has nevertheless begun experimenting with argon LSP powered by fiber-lasers, which offer the modularity required to construct DEP laser arrays, but not for propulsion applications. They have demonstrated the feasibility of LSP using such lasers, with peak temperatures on the same order of magnitude as those sustained by CO₂ lasers, although the necessary power required was approximately an order of magnitude greater, due to the lower absorption coefficient predicted by IB theory. There is still lacking experimental work on the resulting heat deposition into the working gas from the LSP, a critical metric for thruster design, as this heat should ideally be retained in the exhausted propellant to maximize jet power and thrust efficiency.

Considering the current context of directed-energy propulsion favoring fiber lasers operating at 1.06 μm rather than the CO₂ lasers historically considered for LTP, there is a rationale to pursue and update research on LTP and LSP at a fiber laser wavelength. This is *despite* the less favorable IB absorption characteristics at this wavelength. With the long-term objective of developing fully-fledged LTP experimental capabilities at McGill University, the following near-term research objectives were set for this project:

1. Build an argon LSP generator/thruster model to replicate the results of recent, comparable experiments ([30, 44, 46])

Rationale: This establishes a baseline that can be validated against the literature.

2. Determine heat deposition from the LSP into the working gas

Rationale: Understanding the resulting heat deposition can be used to predict thruster performance and/or optimize an LTP thruster using conventional thermal rocket theory.

For this project, argon was selected as a working fluid rather than hydrogen. This is in most part due to its safer handling characteristics compared to hydrogen. It also has a lower ionization energy [47] than neon (a lighter inert gas), is affordable, and its monatomic nature simplifies thermodynamic calculations since no dissociation can occur. Future studies following this project are expected to use hydrogen, especially for thruster prototypes, as hydrogen's lower molecular weight is beneficial to maximize exhaust velocity.

Chapter 3

Facility design

Since there was no existing LSP facility at McGill University, a considerable portion of this project revolved around the design and fabrication of an LSP generator. This is summarized in the following need statement:

NEED STATEMENT

Experimental testing will be critical in the development of a laser-thermal propulsion (LTP) system. Thus, there is a need for a laboratory facility to study laser-sustained plasma and LTP thrust characteristics in conditions comparable to those expected in a working thruster.

This chapter will discuss the major design requirements of such a system, the selection of appropriate solutions, and the assembly, integration, and testing process. Several practical issues were encountered in developing the LSP generator, which are rarely mentioned in the experimental LSP literature. They will be documented in detail in this report in the hopes that this can facilitate future work in this field.

3.1 Existing hardware and OTS components

As seen in [Section 2.3](#) and shown in [Figure 3.1](#), an experimental LTP test facility consists of at least 5 subsystems:

1. A laser source and any beam-shaping optics
2. A pressurized test section or thruster with a suitable ignition mechanism
3. A feed system for the thruster/test section
4. A thrust bench
5. An instrumentation suite to measure pressure, flow rates, temperatures, thrust, etc.

Most of the design activities revolved around subsystem number two: the test section. The laser, feed system, and instruments either were already available in the laboratory or purchased off-the-shelf (OTS). The thrust stand design was delegated to a team of students collaborating on this project.

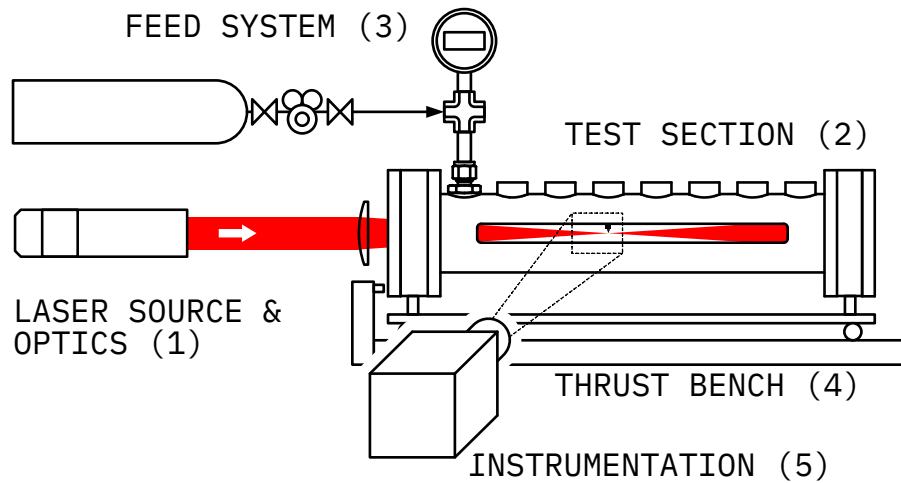


Figure 3.1: LTP Experiment subsystems. The field of view of the high-speed camera is shown in dotted lines. Any snapshots from the camera shown in this report will be from this region.

3.1.1 Laser system

The laser made available for this project was the most important driver of many design decisions. Whether they are for interstellar-class lightsails as envisioned by Lubin [7], or interplanetary missions powered by electric propulsion as proposed by Sheerin *et al.* [48], fiber lasers operating at the 1064-nm-wavelength are currently favored, for both physical and economic reasons discussed in Section 2.1, for many DEP applications. Since LTP is proposed as an additional DEP concept within this ecosystem, this experimental work aimed to match this laser wavelength.

An IPG Photonics YLR-300/3000-QCW-MM-AC Ytterbium fiber laser (seen in Figure 3.2a) was generously loaned to the IFERG by the Royal Military College of Canada. This is an infrared laser primarily designed for welding, drilling, and cutting. It is capable of operating in both pulsed and continuous modes at a wavelength of 1070 nm. Its key specifications are summarized in Table 3.1. A complete calibration report for the laser can be found in Appendix A. An IPG Photonics P30-001736 collimator head (seen in Figure 3.2b) was also acquired for the laser, forming a 1-in-diameter beam at its output. The collimator's calibration report can be found in Appendix B.

Table 3.1: Summary of nominal laser specifications

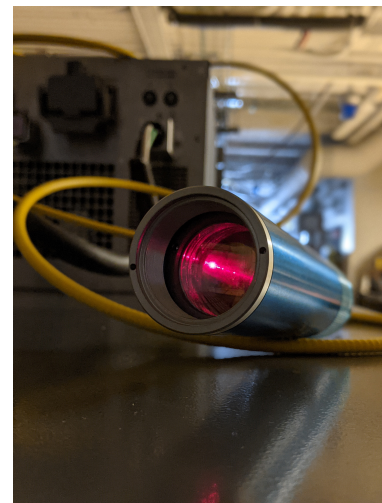
Parameter	Quantity	Unit
Wavelength	1070	nm
Maximum CW Power	300	W
Maximum Pulse Power	3000	W
Maximum Pulse Duration (3 kW)	10	ms
Maximum Pulse Energy	30	J

Although a practical LTP system would likely operate in continuous mode, the YLR laser's pulsed mode was of particular interest in this project. As discussed in [Section 2.2](#), laser power is a critical factor in the ability to achieve a steady LSP. The YLR laser is not only capable of pulsing at an order of magnitude above its CW power rating, but it is able to do so for several milliseconds, a relatively long-pulse in the world of laser physics. This pulse is in fact so long that it is considered to be in the CW regime as far as laser damage is concerned (Thorlabs [49]), hence the *Quasi-Continuous-Wave* (QCW) designation of this laser. This capability enables running very high-power experiments without investing in far more expensive (and dangerous) CW kW-class lasers, although the 10 ms timescale imposes a major constraint on the facility design and experimental methodology.

Laser safety Considerations for safety were paramount in operating the high-power laser. All personnel involved in the project followed mandatory laser safety training prior to participating to experiments. A detailed laser operation procedure was posted at the laser control station and was included in the experiment procedure document (available in [Appendix G](#)). Laser safety screens and safety curtains were used to minimize the risk of laser exposure. Laboratory personnel was instructed to wear appropriate laser-safety goggles. The experiment was designed to be operable without entering the laser curtain enclosure. Appropriate signage and light signals were placed outside the laboratory entrance to inform passersby of the presence and operation of a class-4 laser, as mandated by McGill-wide laser safety guidelines. A laser-safety officer was invited to visit the laboratory to vet the safety measures and provide recommendations that were promptly followed.



(a) IPG Photonics YLR-300/3000-QCW-MM-AC Laser



(b) Laser collimator head

Figure 3.2: Laser system used for this project

3.1.2 Instrumentation

The 10 ms experimental timescale meant that most instruments used on this experiment were selected based on their ability to make measurements within 10 ms or a sampling rate of at least 1 kHz, where applicable.

Laser power meter

A laser power and energy meter was required to determine what fraction of laser power was absorbed by the LSP. A UP55N-300F-H12 power and energy meter from Gentec-EO was procured for this project. This thermopile power meter is rated for a maximum average power of 300 W and a maximum average power density of 45 kW cm^{-2} . These specifications¹, along with its ability to function as both a continuous power meter and a pulse energy meter, made it an excellent match for the IPG laser system. A selection of its nominal specifications can be found in [Table 3.2](#) and its calibration report can be found in [Appendix E](#) page 122. Although the 3-rise time appears to disqualify this power meter for pulsed experiments, using the power meter's pulse energy measurement mode bypasses this limitation.

Table 3.2: Summary of nominal laser power meter specifications

Parameter	Quantity	Unit
Calibrated Spectral Range	248–2100	nm
Maximum Average Power	300	W
Maximum Average Power Density	45	kW cm^{-2}
Rise Time (0–95%)	3	s
Aperture Diameter	55	mm
Calibration Uncertainty	2.5	%

High-speed camera

High-speed footage of the experiment was deemed necessary to study the behavior of LSP and determine some of its basic properties, such as dimensions, growth rate, and brightness. This was also the primary method to confirm successful LSP ignition. The camera used was a Photron FASTCAM SA5, capable of recording at up to 7000 fps at its full 1024×1024 pixel resolution, and up to 775 000 fps when cropping the sensor. Most footage was recorded at 10 000 fps, providing sufficient temporal resolution while maintaining a relatively large field of view, which was necessary to capture the entirety of the plasma.

The use of a high-power laser and the ignition of a plasma (bright source of UV) in the vicinity of this camera was concerning regarding potential damage to the camera sensor. Such damage would result in a lengthy, expensive repair procedure (or complete replacement), and interrupt or hinder not only this experiment, but several other concurrent projects in the lab, as this camera was shared across experiments. Several risk mitigation measures were put in place to minimize the likelihood of serious sensor damage:

- The strategic use of aluminum safety screens to block the path of laser reflection
- The use of a variable neutral-density filter capable of reducing incoming light intensity by a factor of 2000
- The use of a UV-IR cut filter, reducing the intensity of radiation below 390 nm and above 700 nm by a factor of 100

¹Its average power rating may be lower than the laser's peak power, but the pulsed mode allows for enough time for the power meter to cool down between pulses

Both filters were 58-mm-diameter commercial-grade photography filters fitted on a SIGMA 70-300 mm F4-5.6 DG MACRO zoom lens.

Pressure transducer

While simple pressure gauges were sufficient for experiment set-up, pressure data with high temporal resolution was also of interest to study the effect of LSP ignition on the gas pressure, potentially using it as a proxy for temperature change and heat deposition within the test section. PCB Piezotronics 113B28 pressure transducers were sourced within the laboratory. Such transducers are used to detect changes from an initial pressure. With a rise time of less than 1 μs , a usable frequency range of more than 100 kHz, and a nominal sensitivity of 14.5 mV kPa^{-1} , these sensors are well suited to detect rapid and minute changes in pressure that would be expected in this experiment. The transducer's calibration report can be found in [Appendix E](#) page 124.

A possible concern regarding pressure from a safety, design, and measurement standpoint is whether the pressure rise resulting from heat deposition would exceed the measurement range of the transducer and/or the design pressures of the test section. The maximum possible pressure rise can be calculated assuming complete deposition of a laser pulse energy (30.8 J) into the working gas as heat. With the test section parameters seen in [subsection 3.2.1](#) and [Appendix C](#), the maximum expected pressure rise is 37.5 kPa, less than 2% of the maximum design pressure, and equivalent to a 0.56-V rise from the pressure transducer, well within its design range of 5 V (344.7 kPa).

Spectrometer

Spectrometry was identified as one of the primary methods to determine the LSP temperature. Indeed, the high expected plasma temperature (above 10 000 K) and the timescale of the event ($\sim 10 \text{ ms}$) meant that most intrusive methods (and some non-intrusive methods such as infrared thermometers) were inadequate.

Spectrometry is commonly used in neighboring McGill laboratories studying combustion and metal fuels, so a portable USB spectrometer was easily sourced for this experiment. The Ocean Optics (now Ocean Insight) USB4000 [50] is a compact spectrometer with a measurement range of 200 nm to 1100 nm and a minimum integration time (analogous to exposure time for a camera) of 3.8 ms. Although this may not satisfy the sampling rate requirement stated at the start of this section, this was deemed sufficient as determining the temporal change in LSP temperature was not within the scope of the experiment. Varying diameters of fiber optics were tested to determine the optimal fiber size: as this spectrometer was used without an aperture slit, the fiber core diameter affected the spectral resolution. Smaller apertures cast a wider beam on the diffraction grating, illuminating a greater number of grooves and thus providing finer wavelength separation [51].

The use of smaller entrance apertures comes at the cost of reducing the signal strength (i.e., brightness), but the LSP brightness was found to be sufficient to provide a clear spectrum even with the narrowest available 10- μm fiber. The spectrometer was calibrated using an Ocean Optics HG-1 Mercury Argon Light Source for wavelength calibration (ensuring the sensor's pixels match to the correct wavelength), and an Ocean Insight HL-2000 Halogen Light Source for relative intensity calibration (correcting for uneven sensitivity across the captured spectrum).

3.2 Design process

The design of custom hardware was necessary for this experiment. This included a pressurized test section and an ignition system. As mentioned in [Section 3.1](#), a thrust stand was also needed, but its design was delegated to a team of students assisting in the project. These design activities, along with the thrust stand requirements given to the students, will be documented here.

3.2.1 Test section

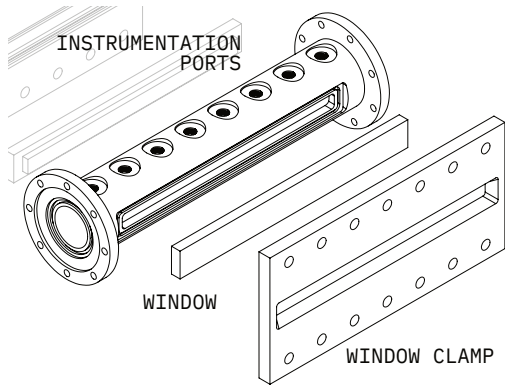
The requirements for the Laser-Thermal Thruster Laboratory Model (LTTLM) are listed in [Table 3.3](#). In summary, the thruster model should be a pressurized vessel featuring one or more windows to allow laser input and optical viewing of the LSP. Furthermore, this vessel should allow the integration of various instrumentation systems. The design and manufacture of such a vessel would have required a significant amount of time, so the alternative of re-purposing hardware from a different project was considered first. This hardware's specifications could be compared to the requirements, and modifications could be made if necessary.

Table 3.3: Top-level design requirements for the LTP laboratory model (the “thruster”)

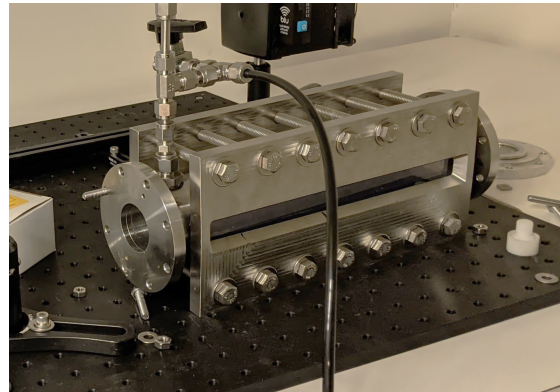
Identifier	Requirement	Rationale
LTTLM-1	The thruster shall operate at a maximum laser power of 3 kW at a wavelength of 1070 nm	This is the laser system made available for this experiment
LTTLM-2	The thruster shall operate using gaseous argon at room temperature as a propellant	The past experiments used for comparison also used argon
LTTLM-3	The thruster shall operate at a maximum design pressure of 2 MPa	This should allow the generation of LSP even in continuous-wave laser modes
LTTLM-4	The thruster shall allow visible observation of the LSP in the thrust chamber	This enables high-speed imaging of the plasma and the remote measurement of its temperature
LTTLM-5	The thruster shall provide interfaces to allow for measuring chamber pressure and gas temperature	This permits the estimation of stagnation conditions for the heated propellant
LTTLM-6	The thruster shall provide interfaces to allow for measuring absorbed laser power	This is one of the major energy losses to be determined
LTTLM-7	The thruster shall have a structural safety factor of 10	This provides an adequate safety margin for operating the thruster

Coincidentally, Kokkalis [52] at the neighboring McGill Fluid Dynamics Lab (FDL) was undertaking research into cavitation effects within piston-cylinder assemblies. His apparatus

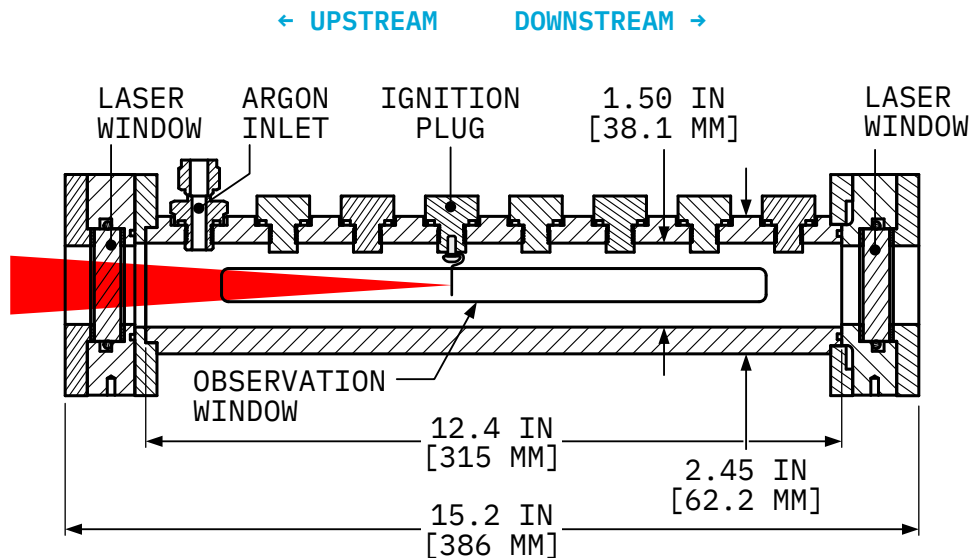
included cylindrical sections designed to withstand high dynamic pressures encountered in their experiments, and featured windows or transparent walls to track the onset of cavitation with high-speed cameras. The design was modular, allowing the installation of various endcaps with different functions. This theoretically fulfilled requirements LT-TLM-2 to LT-TLM-4. One particular test section (pictured in [Figure 3.3](#), detailed drawings can be found in [Appendix C](#)) had been fabricated with a set of instrumentation ports and polycarbonate windows spanning the length of the cylinder. This test section had been tested in a few experiments examining dynamic cavitation in water but was found to be inadequate, as gaps around the ports and windows were sources of parasitic cavitation.



(a) Assembly schematic



(b) Photograph of the test section fitted with a gas feed line



(c) Basic dimensions. Detailed drawings available in [Appendix C](#) and [Appendix D](#)

Figure 3.3: Laser ionization test section

As seen in [Table 3.4](#), this apparatus was verified against the requirements set in [Table 3.3](#) to determine what retrofitting activities would be needed to use it as an LTP thruster model. It was found that very little retrofitting work was required in order to use it as an LSP generator: special instrument plugs could be created, and special laser window endcaps were

needed to seal the apparatus while allowing the laser to enter the test section. To operate the system as a thruster, an existing blank endcap could be modified to accept small nozzles. The apparatus was designed to withstand much greater pressures than the 20-bar design pressure, was tested to withstand this pressure, and a thick-walled pressure vessel calculation showed it had a hoop-stress safety factor of 50 for this application. Finally, as spectrometry was planned to be used for plasma temperature determination, the polycarbonate side windows would have to be exchanged for UV-grade quartz windows, which would allow a broader spectrum of radiation to pass through.

Table 3.4: Verification of LTTLM requirements for the cavitation apparatus

Identifier	Requirement	Status
LTTLM-1	The thruster shall operate at a maximum laser power of 3 kW at a wavelength of 1070 nm	Requires laser windows
LTTLM-2	The thruster shall operate using gaseous argon at room temperature as a propellant	Fulfilled
LTTLM-3	The thruster shall operate at a maximum design pressure of 2 MPa	Fulfilled
LTTLM-4	The thruster shall allow visible observation of the LSP in the thrust chamber	Fulfilled
LTTLM-5	The thruster shall provide interfaces to allow for measuring chamber pressure and gas temperature	Requires special instrument plugs
LTTLM-6	The thruster shall provide interfaces to allow for measuring absorbed laser power	Requires laser windows
LTTLM-7	The thruster shall have a structural safety factor of 10	Fulfilled

However, using this test section would not come without a set of drawbacks. Its original intent made it unoptimized to work as a laser-thermal thruster model for the following reasons:

1. Although its thick stainless-steel construction made it very safe for the operating pressures of the project, it also made it heavy. The superfluous mass would make frictional loads on a thrust bench far more significant than for a custom-designed, lightweight thruster model.
2. Its length forces the use of long focal-length lenses to focus the laser into the test section. Such long lenses would create a high f -number beam, which could affect how easily a stable LSP could be achieved, as discussed in [Section 2.2](#). While shorter lenses would still be able to focus the laser into the chamber, the beam past the focal point would diverge quickly and hit the test section walls, affecting laser absorption measurements at best, or damaging experimental apparatus at worst.
3. Instrumentation ports are available only on one side of the cylinder. The lack of opposing ports constrains the design of certain ignition methods, such as spark igniters.

The alternative was to work on a clean-sheet design that would perfectly satisfy the re-

quirements set in [Table 3.3](#), without the drawbacks of the existing apparatus listed above. While this may have avoided many difficulties encountered later in this project, opting for a custom design would have introduced significant risks in terms of timeline, compounded by the many uncertainties surrounding the operation of an LSP generator/LTP thruster. In order to quickly move forward with the project, it was decided to retrofit the existing cavitation apparatus into an LSP generator. It was reasoned that the lessons learned in attempting experiments with an unoptimized system would still be valuable to document and would be very effective in informing the design of a custom thruster laboratory model.

3.2.2 Laser window mount

The first and most important retrofitting task was the implementation of windows allowing the laser to enter the test section, then exit it, with minimal power losses. In terms of methodology, significant power losses would be acceptable as long as they are measurable and consistent, such that they can be accounted for. However, minimizing them is beneficial to allow the complete use of the laser's power range. As anti-reflection coated optics could readily be found with less than 1% power losses, this was deemed as an acceptable threshold.

Three major requirements thus drove the laser window design:

1. The window shall transmit at least 99% of the incident laser power. *Rationale:* this maximizes the available laser power within the test section.
2. The window shall seal the test section at 20 bar and remain structurally sound. *Rationale:* this directly derives from requirement LTTLM-3.
3. The window shall have a structural safety factor of 10. *Rationale:* this directly derives from requirement LTTLM-7.

Pressure vessel windows are often needed in the IFERG—the group has thus acquired useful experience on their design, adopting design guidelines from the Brookhaven National Laboratory [53]. In summary, these guidelines provide design formulas, empirically derived properties, and tried-and-tested designs for various applications. The window mount follows the “free edges” design (Figure 14 in [53]), deemed most appropriate for this application, and having been successfully implemented² in past experiments. In this design, a peripheral o-ring provides a reliable seal, while two rubber or Teflon gaskets support the window and prevent its edges from touching the metal walls. This is the critical design criterion for pressure windows: although glass and crystals often exhibit excellent tensile strength, their brittleness makes them susceptible to localized stress concentrations which ultimately are the source of failure. This occurs at glass-metal contact points, so pressure window designs focus on preventing these contacts by minimizing strain and introducing soft interfaces such as Teflon or rubber gaskets.

The calculation procedure described in [53] for elliptical windows was used to size an appropriate window based on different materials and suppliers. Sapphire, borosilicate glass (N-BK7), and quartz were considered as potential materials. Strict application of the guide's mandated safety factor of 10 and the use of the full test section internal diameter (38.1 mm or 1.5 in) as the aperture size led to window dimensions that could not be sourced from

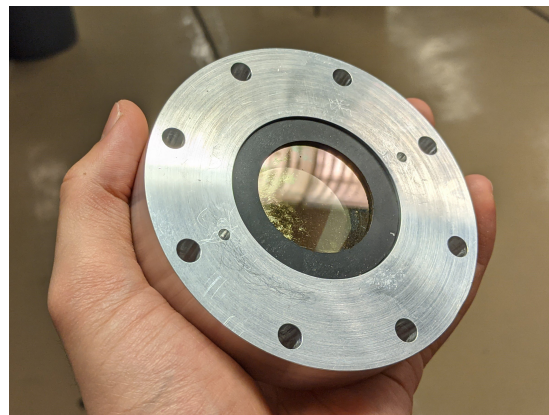
²A former laboratory member consulted on this design problem stated: “Every time I did not follow this guide to the letter, it failed.”

off-the-shelf suppliers. To reduce costs and facilitate supply, a compromise was reached by reducing the effective aperture to 1.4 in (35.6 mm) to provide more support to the window while accepting a reduced safety factor of about 9.1. The resulting window is 12-mm-thick and 50.8 mm in diameter for N-BK7 glass, which is supplied by Thorlabs as WG12012-C [54]. Other suppliers either could not supply a window matching these specifications or did so for a much higher price. Likewise, other material choices resulted in window dimensions that could not be sourced off-the-shelf.

Window mounts (pictured in Figure 3.4) were then designed to interface with the existing apparatus, following the “free edges” design. As the existing apparatus had no mounting arrangements, the window mounts also featured a tapped hole allowing the mounting of optical posts (as seen in Figure 3.4a) to the assembled test section. This permitted its integration with an optical table system, greatly facilitating experimental setup. Complete drawings for the window mounts can be found in Appendix D.



(a) O-ring installed and mounted on optical post



(b) Window installed in mount with gasket

Figure 3.4: Laser window mounts

3.2.3 UV-grade side windows

The windows installed on the existing cavitation apparatus were bonded acrylic and polycarbonate. While this was sufficient for observation in the visible spectrum, these materials are less suitable to perform spectroscopy, which would be an integral part of the instrumentation used for the project. Data gathered by Zimakov *et al.* [30] and Lu *et al.* [46] suggest significant radiation emission both in the near ultraviolet and near infrared. Polycarbonate and acrylic both feature a sharp drop in transmission between 400 and 450 nm, along with irregular (although admittedly high) transmission in the near-IR [55]. To ensure a complete picture of the plasma’s radiation emission was captured, the decision was made to replace these plastic windows with UV-grade fused silica (JGS1). As seen in Figure 3.5, this material features a relatively uniform transmission profile from 210 nm to 1000 nm. An added benefit of the new windows was greater optical clarity in the visible spectrum as well. Windows matching the geometry of the polycarbonate windows were ordered from Dalian Unique Optics Co., Ltd. in China. A set of gaskets cut out of Buna-N rubber were used to seal and protect the window, as it is subject to the same failure modes discussed in subsection 3.2.2.

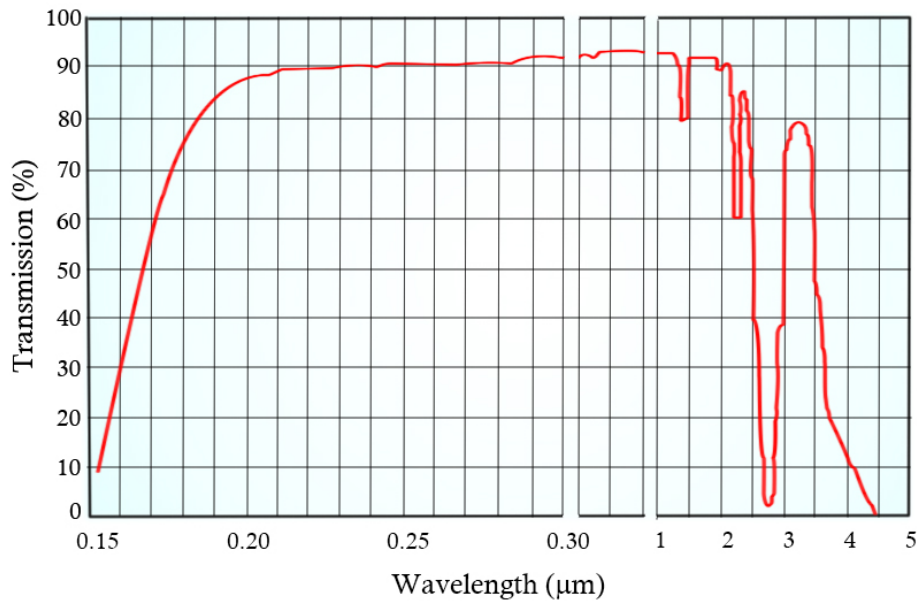


Figure 3.5: Transmission profile of JGS1 fused silica [56]

3.2.4 Spark-ignition system

As seen in [Section 2.3](#), several methods were devised to ignite LSP, i.e. create a seed plasma that could initiate the inverse bremsstrahlung laser absorption mechanism. These include:

- Inducing a plasma using a separate high-power laser pulse
- Focusing the laser onto a solid tungsten or titanium target, releasing an electron cloud by thermionic emission (Schwartz *et al.* [40]) that could initiate LSP
- Focusing the laser onto an electrical arc discharge across two electrodes

An ignition mechanism was selected based on available resources and experimental requirements, namely:

1. The ignition system shall not impede the measurement of absorbed laser power by the plasma. *Rationale:* derives directly from requirement LTLM-6.
2. The ignition system shall operate on a millisecond timescale. *Rationale:* the laser pulse will be as short as 10 ns, so an ignition system should function within a couple of milliseconds or be capable of triggering with millisecond precision.

The use of a separate high-power laser pulse to induce a seed plasma would likely fulfill both requirements, as this is a non-intrusive ignition method, and such lasers often operate with nanosecond pulses or shorter. However, this would require the purchase of a second laser system at a high cost and a long lead time, so this option was discarded. Solid metal targets offer an easy to implement, reliable, and affordable ignition solution, but was thought to be unable to fulfill the requirements listed above: Placing a solid target in the beam path would prevent the measurement of laser power exiting the plasma. While actuators could be used to remove the target, these would add complexity and likely be unable to operate within the desired timescale.

This left spark ignition as the preferred solution: spark igniters are easily triggered with precision thanks to their fully electrical, solid-state operation, the lack of moving parts also facilitate sealing, and the electrode spacing can be controlled to avoid intersecting the laser beam path. Furthermore, such systems have been in use in various other projects in the laboratory, so this would build on past experience.

Past work within the laboratory and the Thermodynamics and Combustion Group of Concordia University converged on a design based on the use of “smart” high-performance automotive ignition coils. Such coils are charged with a DC power supply and triggered based on a Transistor-to-Transistor Logic (TTL) signal, which can be generated by a wide variety of electronics, including precision digital delay generators commonly used in the laboratory. Reliable spark-igniter operation had previously been achieved with the AEM 30-2853 High Output Smart Coil. This coil can output a 40-kV voltage and a spark energy of up to 103 mJ. Detailed specifications can be found in its instruction manual [57].

The spark-igniter circuit design (illustrated in Figure 3.6) was adapted and greatly simplified from previous implementations for other projects, as this experiment only required a single arc discharge at a time. Previous igniter designs featured control electronics to trigger a series of sparks—these electronics were discarded as they introduced complexity and unreliability for the benefit of flexibility that was not needed in this project. In this simplified design, the coil awaits a 3- to 9-ms-long 5-V gate signal to charge. This gate signal is generated directly by a delay generator that can be triggered manually or from an external signal. Once the gate signal ends, the coil releases its energy through the high voltage terminal at 40 kV. This energy discharges across the spark plug’s electrodes, creating a spark. The negative electrode is connected to the coil’s spark ground (on pin 3), the test section body, and a real ground wire, to ensure that no residual voltage remains in the system.

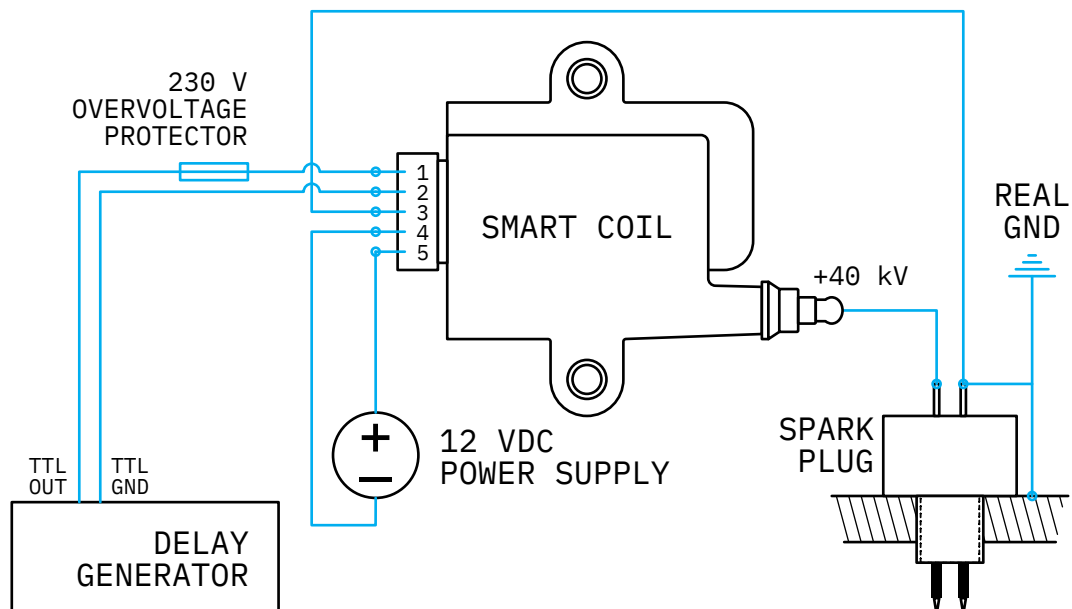


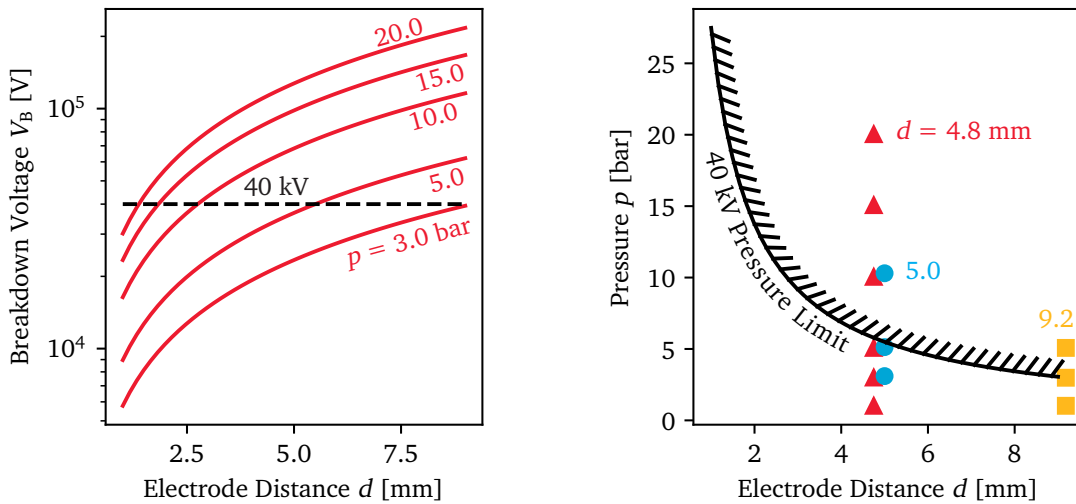
Figure 3.6: Spark-ignition circuit diagram. Not pictured are various switches used to safely operate the system.

Figure 3.6 also depicts the custom spark plugs fabricated for this experiment: two holes were drilled in blank Delrin plugs, through which industrial steel sewing needles were driven. After bonding them to the plug body with epoxy and applying insulation, these plugs were fitted with wire terminals to connect to the smart coil. A notable difference in this design from past literature is the use of side-by-side electrodes instead of electrodes inserted at opposite ends and meeting in the middle. This was due to the absence of opposing ports on the test section. The drawback of this design is a greater likelihood of a spark forming somewhere other than between both needle tips, but the use of insulation mitigated this issue.

Electrode spacing is a key design parameter for the custom spark plug. The discharge arc length d is a function of the gas properties, pressure p , and applied voltage V_B , as seen in Equation 3.1:

$$V_B = \frac{Bpd}{\ln(Apd) - \ln\left(\ln\left(1 + \frac{1}{\gamma_{se}}\right)\right)} \quad (3.1)$$

This is known as Paschen's law. The parameters A and B depend on the gas and are determined experimentally. The secondary-electron-emission coefficient γ_{se} is also different for each gas [58]. This equation can be solved (numerically) for the electrode distance required to arc at a certain voltage and pressure. This is shown in Figure 3.7a, where the required voltage is plotted for the range of operating pressures planned for the experiment. A line is drawn at 40 kV to represent the smart coil's output—in theory, as long as this line intersects all pressure curves, there exists an electrode distance at which the spark plug will successfully arc. The values used for this model are as follows, taken from Lieberman and Lichtenberg [58] and Theis *et al.* [59] for argon: $A = 11.5 \text{ cm}^{-1} \text{ Torr}^{-1}$, $B = 176 \text{ V cm}^{-1} \text{ Torr}^{-1}$, and $\gamma_{se} = 0.07$.



(a) Required voltage to arc across electrodes

(b) Spark tests with varying electrode spacing

Figure 3.7: Exploration of spark-gap size in argon with Paschen's law

This initial model was sufficient to proceed with prototyping spark plugs. Several prototypes were fabricated with varying electrode spacing to determine the maximum electrode gap that could spark across the range of operating pressures. The plugs were then tested to

compare their performance to the limit predicted by Paschen's law. The results are shown in [Figure 3.7b](#). One can distinctly see that the spark plugs appear to successfully spark beyond the pressure limit predicted by Paschen. This is thought to be due to the electrode geometry. Indeed, the A and B parameters used above were determined for parallel flat plate electrodes, whereas the pointed electrodes are more favorable for arcs by concentrating the electric field near the tips. Furthermore, more sophisticated Particle-In-Cell simulations for spark formation implemented by Theis *et al.* [59] suggest that Paschen's Law overestimates the necessary breakdown voltage for pd values above 10 Torr cm.

As far as the experiment was concerned, the test showed that a single spark plug with electrodes spaced by 4.8 mm was sufficient to spark throughout the range of operating pressures considered for the experiment. The 4.8 mm gap sparked reliably while still leaving ample space for the laser beam. Initial LSP ignition tests would later show that this design approach is not optimal, as will be discussed in [Section 5.1](#).

3.2.5 Thrust stand

In order to perform preliminary thrust experiments, the LTTLM would have to be mounted on a custom thrust stand. The design and assembly of this thrust stand was delegated to a team of students collaborating on the project. A preliminary set of requirements were given to them, inspired in part by thrust stand designs by Takken [60] and Jansen [61], which would be verified upon delivery of the thrust stand. As is discussed in detail in [Section 4.4](#), the expected thrust at the given laser power levels for an LTP thruster are much lower than stated in requirement TS-2. This requirement was set in part to accommodate for the use of larger nozzles than needed, which would allow for test-section flow velocities on the order of 1 m s^{-1} . As discussed in [subsection 3.3.3](#), issues in developing the thrust stand lead to focusing on static LSP tests rather than attempting to take thrust measurements of the LSP-powered thruster.

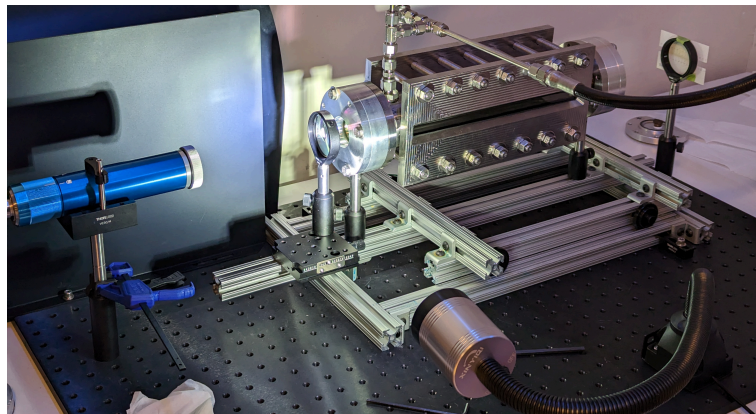


Figure 3.8: Test section mounted on the delivered thrust stand. Load cell, DAQ, and preload/calibration system not pictured. Details on the feed system are provided in [subsection 3.3.4](#).

The delivered design (pictured in [Figure 3.8](#)) consisted of a wheeled cart placed on aluminum extrusion rails, featuring the means to attach several weights to preload the stand. The structural design of the stand satisfied requirements TS-1 and TS-4 through TS-7. Thrust measurement was performed using a Honeywell FSG020WNPB force sensor, whose

Table 3.5: Top-level design requirements for the thrust stand (the “system”)

Identifier	Requirement	Rationale
TS-1	The system shall hold up the thruster such that its thrust axis is horizontal	This ensures the horizontal laser beam can be lined up with the thrust axis
TS-2	The system shall have a maximum measurable thrust rating of at least 10 N, and no greater than 20 N	The expected operating pressures and nozzles would yield a maximum thrust within that range
TS-3	The system shall provide thrust measurements with a sample rate of at least 1000 S/s	This provides at least 10 thrust readings during a laser pulse
TS-4	The system shall not impede laser focusing into the thruster	The laser must be able to focus into the chamber to sustain LSP
TS-5	The system shall allow known loads to be applied for calibration and preloading	Applying these loads allows correction for friction and backlash in the system
TS-6	The system shall mount to existing optical benchtop	This facilitates integration with the optical hardware
TS-7	The system shall not impede existing measurement equipment	Impeding other instrumentation would limit the type of experiments that can be performed

signal was processed by a DATAQ Instruments DI-2108 data acquisition system. The force sensor’s maximum load rating of 20 N and the DAQ’s 50-kHz maximum rate frequency meant that requirements TS-2 and TS-3 were also satisfied. Optical hardware could be mounted onto the cart itself, which facilitated laser alignment with the test section.

3.3 Integration and test

As part of the design process and the progressive integration of all the experimental apparatus, a series of tests were performed on various components of the experiment. This was done to verify each component performed as expected and to a degree deemed sufficient for the experiment.

3.3.1 Pressure testing

One of the first concerns regarding the test section acquired from the FDL was whether it could sustain 20 bar of internal pressure and whether it could maintain this pressure with minimal leakage. Before taking possession of the test section, the FDL demonstrated that it could sustain the necessary 20 bar of pressure without failing. They also showed the test section had an average leak rate of 0.04 bar/min when pressurized with 11 bar of nitrogen, or a 1.8% pressure drop over 5 minutes. To determine whether these promising results would be applicable to argon, the leak rates L of two different gases in the same system

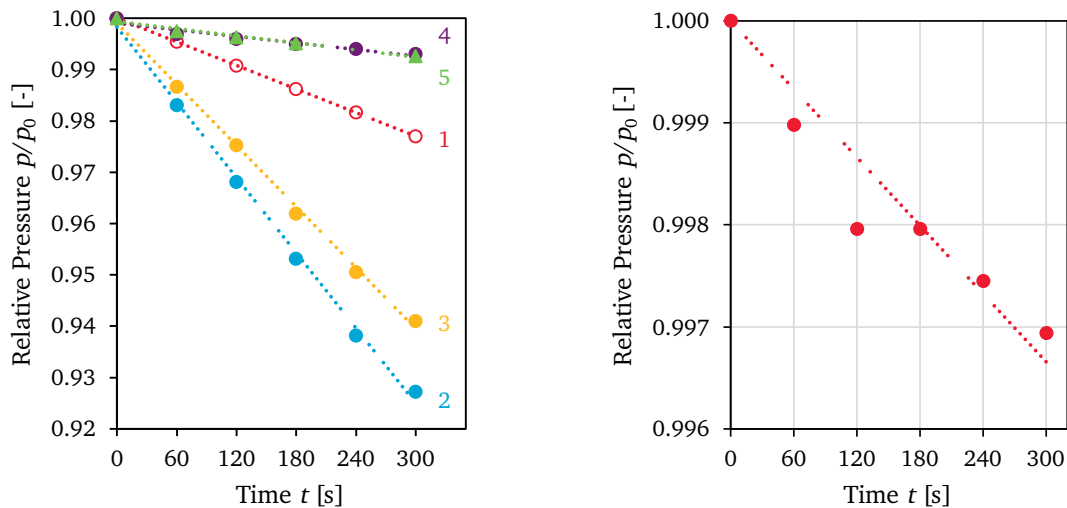
and conditions can be related by Equation 3.2 (Greenhouse *et al.* [62]):

$$\frac{L_{\text{Ar}}}{L_{\text{N}_2}} = \sqrt{\frac{\mathcal{M}_{\text{N}_2}}{\mathcal{M}_{\text{Ar}}}} \quad (3.2)$$

Where the leak rate L is expressed as the product of a volume and pressure loss rate, e.g. Pa m³/s. Evaluating Equation 3.2 with the properties of argon and nitrogen shows that the test section is expected to leak 16.3% slower when filled with argon. This provided the confidence needed to move forward with repurposing the FDL's cavitation test section into an LSP generator.

An acceptable leak rate was determined based on the expected time needed to complete an experimental trial after pressurizing the test section. This time is needed to perform laser safety procedures (closing laser curtains, turning on a laser warning light, etc.), power on the laser, check that instrumentation is ready, and more. This was estimated to take 5 minutes, and a 1% loss in test section pressure was deemed acceptable within that time frame.

Figure 3.9a shows the results of pressure testing the test section as received from the FDL, i.e., fitted with polycarbonate/acrylic side windows, and with the ends sealed with blank endcaps. This was necessary to confirm that similar leak rates could be achieved with argon compared to the nitrogen test, and to serve as a comparison basis once new windows would be integrated in the test section. As seen in Table 3.6 a series of tests were performed at varying argon pressures, with attempts made to minimize leaks. Pressure measurements were read off a digital pressure gauge at 1 minute intervals. Only minor adjustments to the test section fittings were needed to bring the leak rate below the acceptable threshold of 1% over 5 minutes.



(a) As received from the FDL, see Table 3.6 for details

(b) With new laser windows and side windows

Figure 3.9: Pressure leak tests on the test section

Once the laser windows and UVFS windows were installed, another pressure test was performed to qualify the facility for experimentation. Figure 3.9b shows the result of this

Table 3.6: Pressure leak tests on test section received from the FDL. The initial pressure is p_0 , $\overline{dp/dt}$ is the average leak rate, and $\Delta p/p_0$ is the relative pressure loss after a specified time.

Test #	p_0 [bar]	$\overline{dp/dt}$ [bar/min]	$\Delta p/p_0$ (5 min)	Comments
1	3.01	0.0138	2.3%	
2	6.92	0.1007	7.3%	
3	7.25	0.0855	5.9%	Tightened plug #2
4	6.95	0.0097	0.7%	Replaced vent valve
5	11.24	0.0165	0.7%	

test, done at an initial pressure of 19.6 bar. The test section leaked at an average rate of 0.012 bar/min, resulting in a relative pressure loss of 0.3% after 5 minutes, well within the acceptable rate. The improved leak rate is thought to be due partially to the use of UVFS windows: their smoother surface finish may have provided a better seal, and their susceptibility to fracture meant that careful tightening of the window clamp was required. This was performed with a torque wrench, tightening each bolt of the clamp to 5 N m, following a sequence used for bolting automotive engine cylinder heads. In addition to preventing window fracture, this evenly distributed the clamping load, minimizing the chances of a leak path forming between the window and the gasket.

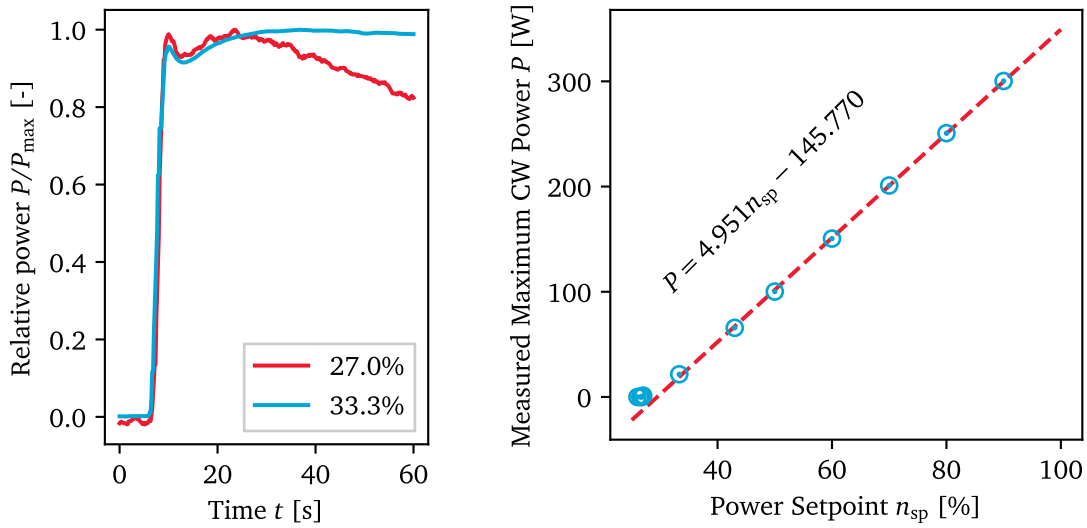
3.3.2 Laser power tests

Laser power and optical power loss tests were necessary to understand the limitations of the laser system and determine the losses induced by the optics in the experiment.

The YLR-300/3000 laser provides control over the laser power as a setpoint percentage. Early laser tests showed that there was a minimum threshold setpoint under which the laser would not function. Such a phenomenon is implied by the calibration report but is not explicitly documented. As the primary method to control power is through this setpoint percentage system, calibration was required to determine the true useful CW and pulsed power range. To do so, the laser was set up to point directly at the Gentec power meter and turned on over a range of power setpoints. The incident power on the power meter was then recorded.

The result of this first test run are shown in [Figure 3.10](#). The power setpoint threshold was found to be at approximately 27%. This was the point at which a significant signal was detected on the Gentec power meter. The power stability at that threshold is poor when compared to a higher setpoint, as seen in [Figure 3.10a](#), and the output power at that setpoint deviates from the otherwise closely linear relationship between setpoint percentage and output power, seen in [Figure 3.10b](#). In addition, the maximum CW power appears to significantly exceed the nominal average power rating of the laser, at 350 W instead of 300 W. Considering these results, the effective operating range (where the power is stable and in the linear range) of the laser in CW mode was deemed to be between 30 and 100%. A linear fit of the data (for $n_{sp} \geq 30\%$) was made to accurately convert a given setpoint n_{sp} to an output power P , with the resulting affine function printed on [Figure 3.10b](#).

In the pulsed power regime, similar tests were performed, but found a practically linear relationship. Furthermore, pulsed mode could be controlled with IPG's PulseShaper soft-



(a) Power stability: the decrease in power seen after the initial peak is due to the power meter's rise time compensation ("anticipation") feature. This did not affect the calibration results as the steady state measurement was used.

(b) Setpoint percentage to power relation. Blue markers represent experimental tests, the dashed line is a linear fit for the data, excluding points below 30% of setpoint power.

Figure 3.10: CW laser output power test results

ware, which used calibration settings saved on the laser itself to accurately determine the pulse power/energy. The maximum pulse energy (100% for 10 ms) was 30.8 J.

Optical power losses

As mentioned in subsection 3.2.2, power losses through the focusing optics were expected and tolerated as long as they could be measured and accounted for. The power losses in the system can be characterized by Equation 3.3:

$$P_m = P(1 - \ell_1)(1 - \ell_w)(1 - \alpha_{LSP})(1 - \ell_{\text{other}})(1 - \ell_w) \quad (3.3)$$

Where P is the laser power exiting the collimator, ℓ_1 is the loss due to the lens, ℓ_w is the loss due to a laser window, ℓ_{other} are losses due to parts of the test section interior blocking the beam, and P_m is the measured power at the power meter. The power absorbed by the LSP is also included as α_{LSP} , and must be determined during experiment. These losses are illustrated in Figure 3.11. If $(1 - \ell_1)(1 - \ell_w)$ and $(1 - \ell_{\text{other}})(1 - \ell_w)$ can be determined separately (although with no need to determine the individual losses due to each component), then they can be accounted for to calculate an accurate value for α_{LSP} .

To determine these losses, the laser was programmed to output 100 W of CW power. Incident power was measured by the Gentec power meter with no optics. Then, the focusing lens and one laser window were placed in the beam path between the laser collimator and the Gentec power meter. The incident power in both cases was measured for 30 s once the power meter's signal reached steady-state (after 60 s). This allows the measurement of $(1 - \ell_1)(1 - \ell_w)$. A similar procedure was followed to determine

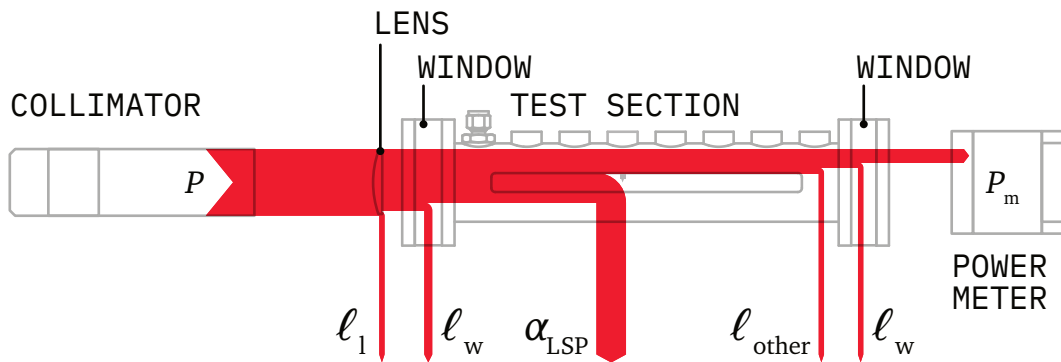


Figure 3.11: Qualitative diagram of laser power losses throughout the test section.

$(1 - \ell_1)(1 - \ell_w)(1 - \ell_{\text{other}})(1 - \ell_w)$, by placing the focus lens and the entire test section in the laser beam path. The results of both tests are summarized in [Table 3.7](#).

Table 3.7: Optical power loss test summary

Test	P [W]	P_m [W]	$P - P_m$ [W]	$1 - P_m/P$ [-]
Front optics	100.19	99.60	0.587	0.586%
Full test section	100.92	95.32	5.602	5.551%

These results can be used to compute the loss terms as follows:

$$(1 - \ell_1)(1 - \ell_w) = \frac{P_m}{P} = \frac{99.60}{100.19} = 0.9941$$

$$(1 - \ell_{\text{other}})(1 - \ell_w) = \frac{P_m}{P} \frac{1}{(1 - \ell_1)(1 - \ell_w)} = \frac{95.32}{100.92} \frac{1}{0.9941} = 0.9501$$

The much greater losses at the exit of the test sections are likely due to the laser beam being reflected or otherwise blocked by parts of the test section itself. This is an issue at the exit rather than at the laser inlet, as the diverging beam makes it more difficult to entirely avoid reflections. However, as these losses are quantified, they can be compensated for during experiments.

3.3.3 Thrust stand testing

Although the delivered thrust stand appeared to match the desired requirements, a series of tests were still necessary to develop a calibration procedure and ensure it provided an accurate thrust measurement. It soon became apparent that the friction caused by the test section's weight would pose a challenge.

The static friction in the system provided much of the reaction force against the thrust, meaning reading the system's thrust directly off of the load cell was not possible. Instead, a calibration procedure was performed using known masses pulling on the apparatus. Masses

were added to progressively increase the applied load, then removed in the same manner, to provide a calibrated voltage-to-thrust conversion factor in both directions.

Significant hysteresis was also observed in the system: the measured thrust would not return to 0 at the end of a test, remaining instead close to the final “real” thrust reading despite the lack of flow. There was therefore low confidence in the accuracy of any thrust profile that was not monotonically increasing. To mitigate this issue, a system of ropes and cables, illustrated in [Figure 3.12](#), was set up to relieve some of the weight of the test section on the thrust stand. Although this appeared to resolve hysteresis, this introduced other issues. The load cell’s signal was found to be much noisier, and the readings from the system did not seem consistent with the applied loads, whether from known masses or the thruster itself. It is thought that relieving the test section’s weight from the thrust stand made it more susceptible to loads and moments imparted by the feed system tubing and misaligned thrust axis and load cell.

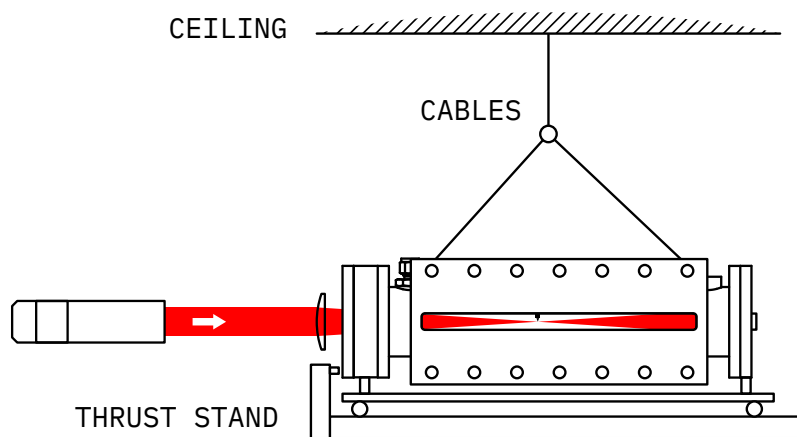


Figure 3.12: Diagram of cable system used to relieve thruster weight from the thrust stand

In addition to these issues, the problems encountered in other areas of the project including ignition and diagnostics for static LSP, the realization that the deposited heat would likely result in a change in thrust too small to be measured, and the planned design of a dedicated thruster testing model in the future meant that work on the thrust stand was suspended in order to focus efforts on other parts of the project.

3.3.4 System integration

Once the necessary parts were manufactured, installed, and tested, the experimental apparatus could be integrated together. As the laser pulse duration was short, precise timing and triggering was needed to ensure the necessary conditions for LSP formation, and integration work focused on connecting instrumentation, ignition systems, and the laser such that an entire experimental trial would automatically run with a single trigger. Laser tests and spark tests showed that the laser pulse would begin 2 ms after receiving an EMISSION START signal, while the spark would occur at the end of a gate signal which could be controlled to be between 3 ms to 9 ms. The experiment was then planned to occur as summarized in [Table 3.8](#). This information can also be found in a graphical form in [Figure 3.13](#), with indications on which triggering signals are active and what they trigger. For

flowing tests, a solenoid valve was used to control gas flow—argon was allowed to flow for at least 5 s to ensure the test-section pressure stabilized before actually initiating the LSP experiment.

Table 3.8: Timeline of one experimental run

Time [ms]	Event
0.0	Experiment is triggered manually. High-speed camera begins recording. Spark-igniter gate signal is opened to charge it.
6.0	EMISSION START signal is sent to laser. Oscilloscope begins recording pressure transducer signal.
8.0	Laser pulse begins.
9.0	Spark-igniter gate signal closes, spark begins. LSP should begin forming.
10.0	Spark should have ended. LSP continues growing.
11.0	Spectrometer begins capturing radiation.
15.0	Spectrometer stops capturing radiation.
18.0	Laser pulse ends, LSP dissipates.

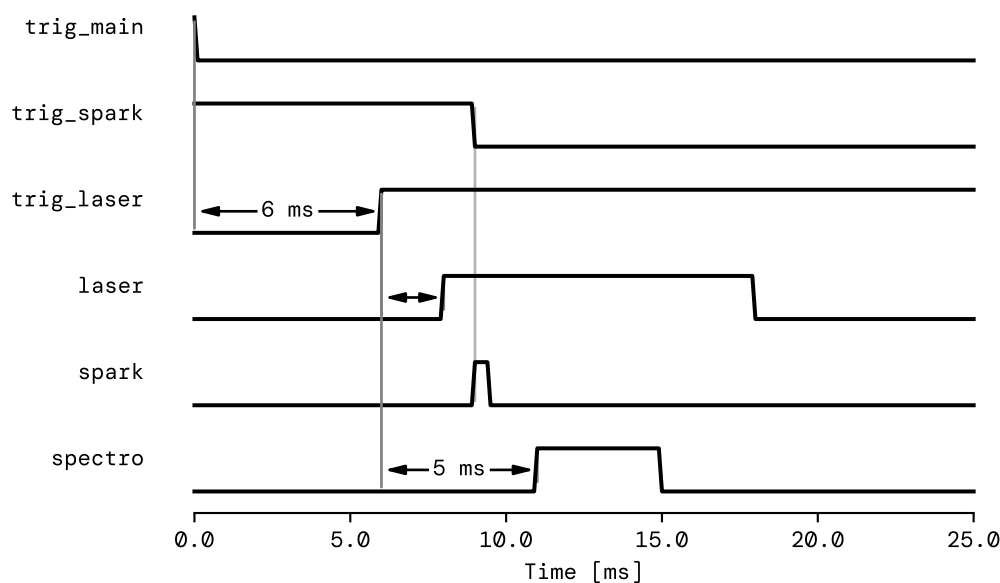


Figure 3.13: Signal timing diagram of an experimental run. Triggering signals are prefixed with `trig_`, all lines indicate whether a component is active (high) or inactive (low). Consult [Table 3.8](#) for additional details.

Experiment control A series of digital delay generators, seen in [Figure 3.14](#), was used to achieve the timings listed shown in [Table 3.8](#). These devices use coaxial cables terminated with BNC connectors as inputs/outputs and provide easy adjustment of timings down to sub- μ s precision, making them ideal to tweak the triggering sequence as the experiment was modified.

The laser, triggering systems, computer for data acquisition and camera control, and an

oscilloscope were mounted on a 19-inch rack, allowing a single operator to run an experiment from the same location. This capability was critical, as the experiment area was contained by laser curtains to protect lab personnel. The oscilloscope was a useful tool to troubleshoot communication between delay generators and other devices, and to monitor the state of the laser at all times.

Optics Control over the laser focus was critical to reliably ignite LSP, avoid losing laser power before it reached the power meter, and avoid specular reflections that could damage instrumentation. Several focusing lenses were purchased of varying focal lengths, although all experiments were performed with a 200-mm N-BK7 lens. The longer focal length, although not ideal for LSP stability as discussed in [Section 2.3](#), made it easier to ensure the entire beam would be allowed through the exit window into the power meter, since the beam divergence was smaller. A diagram showing relevant dimensions for optical alignment can be seen in [Appendix D](#), page 120. The lens was mounted on a set of leadscrew-operated optical stages, allowing precision adjustments to the lens position with 3 degrees of freedom.

Feed system Argon gas was provided from a gas cylinder, fitted with a high-pressure regulator, a manual metering valve, and a solenoid valve. Argon was delivered to the test section through 1/4-in tubing. A second manual metering valve was fitted on the tubing to allow venting of the test section. An Omega digital pressure gauge provided an absolute static pressure reading of the test section and was used as the definite measure of test-section pressure when operating the regulator. Mass-flow rates were to be controlled by the choked orifices, as mass-flow meters able to precisely determine flow rates at a high sample rate were not available. This would leave a significant uncertainty on calculated flow rates, but was deemed sufficient at the current stage of the project.

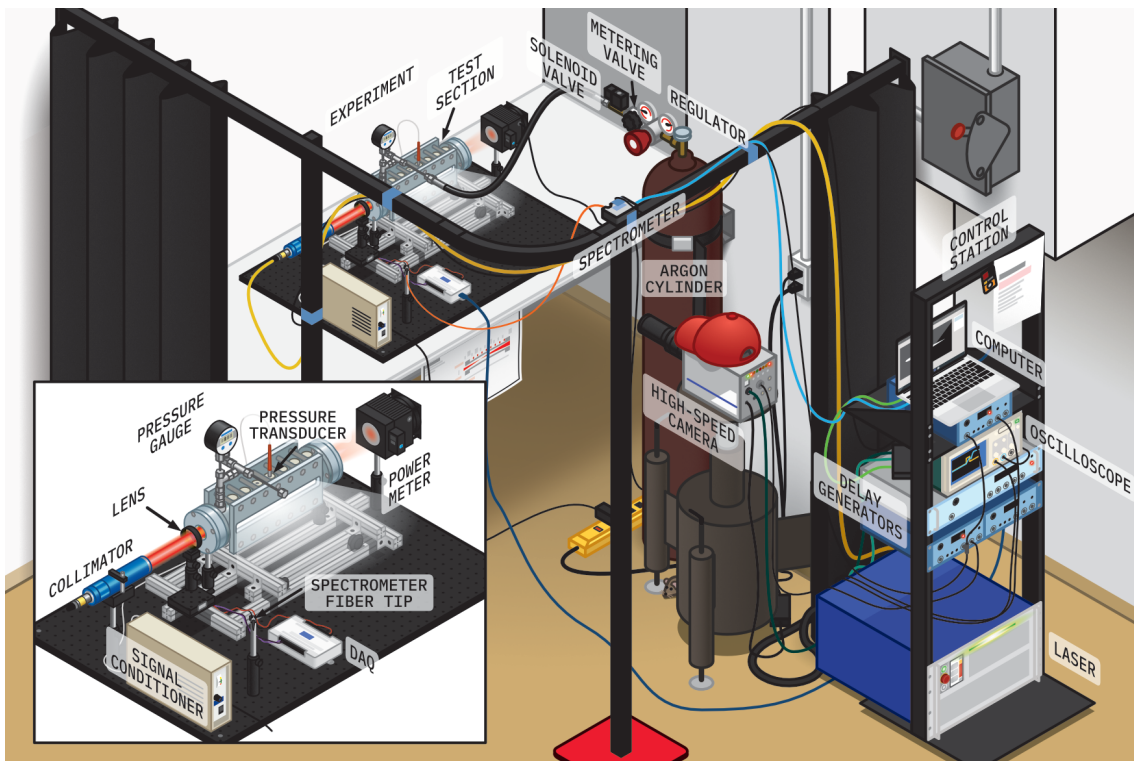


Figure 3.14: Overview of the experimental setup. Spark igniter is not pictured.

Chapter 4

Modelling

Although the work of this project was primarily experimental, some modelling work was performed in order to better understand the physics of LSP and aid in the experimental design. One major area of interest is in determining the absorption properties of LSP. High laser absorption is desirable to maximize power conversion efficiency. Furthermore, the IB absorption coefficient typically reaches a maximum at a specific temperature. According to Keefer [22], this peak absorption temperature was found to closely correlate with LSP peak temperature. The measurement of absorption coefficient can thus be used to support LSP temperature estimates.

4.1 Absorption

A critical property of LSP is its ability to absorb laser radiation. As stated in Section 2.2, the primary mechanism for radiation absorption in LSP is inverse bremsstrahlung. Calculation of the absorption coefficient of this process is critical for modelling LSP behavior and estimating its laser absorption efficiency. The calculation method presented here aims to adapt the work of Akarapu *et al.* [63] and Nassar [64], who have developed CFD models for the use of argon LSP in surface-treatment applications. Although their work considered CO₂ lasers, adapting the method to the fiber laser of this study is a matter of using the appropriate laser frequency in Equation 2.2. Their work was thus used to validate each calculation step, and their results will be plotted alongside this study's computations when relevant. A step-by-step example calculation is provided in Section F.1.

The absorption coefficient can be calculated using Equation 2.2 and is heavily dependent on electron density n_e and radiation frequency ν . The first step of absorption modelling is thus to determine electron density, which is variable with temperature T according to the Saha ionization equation, developed by Saha and Fowler [65]. It is reproduced here for the single ionization case as Equation 4.1.

$$\frac{n_e^2}{n_0 - n_e} = \frac{n_e^2}{n_{Ar}} = \frac{2}{\Lambda_{th}^3} \frac{\mathcal{Z}_{Ar^+}}{\mathcal{Z}_{Ar}} \exp\left(-\frac{E_{ion, Ar}}{k_B T}\right) \quad (4.1)$$

Where n_0 is the initial number density of neutral atoms, n_{Ar} is the number density of unionized atoms at a given temperature, $E_{ion, Ar}$ is the first ionization energy of argon (15.76 eV [66]), and k_B is the Boltzmann constant. In this case, the product $k_B T$ can be

expressed in J or eV depending on the unit of $E_{\text{ion, Ar}}$. The thermal DeBroglie wavelength Λ_{th} is a function of temperature as follows, where \hbar is the reduced Planck constant and m_e is the mass of an electron:

$$\Lambda_{\text{th}} = \sqrt{\frac{2\pi\hbar^2}{m_e k_B T}}$$

The ratio $\mathcal{Z}_{\text{Ar}^+}/\mathcal{Z}_{\text{Ar}}$ is the ratio of the partition function values for Ar^+ and Ar (also designated Ar II and Ar I, respectively). These values are also dependent on temperature and can be queried in the NIST Atomic Spectra Database (ASD) (Kramida *et al.* [47]) for a given spectrum (e.g., Ar I) and electron temperature T_e . This ratio is plotted in Figure 4.1a. Nassar fitted a seventh-order polynomial (shown in Equation 4.2) to approximate this ratio across temperature:

$$\begin{aligned} \frac{\mathcal{Z}_{\text{Ar}^+}}{\mathcal{Z}_{\text{Ar}}} = & -2.3077 \times 10^{-29} T^7 + 2.3474 \times 10^{-24} T^6 \\ & - 8.8453 \times 10^{-20} T^5 + 1.4851 \times 10^{-15} T^4 - 9.843 \times 10^{-12} T^3 \\ & - 1.2477 \times 10^{-8} T^2 + 0.00047534 T + 3.7971 \quad (4.2) \end{aligned}$$

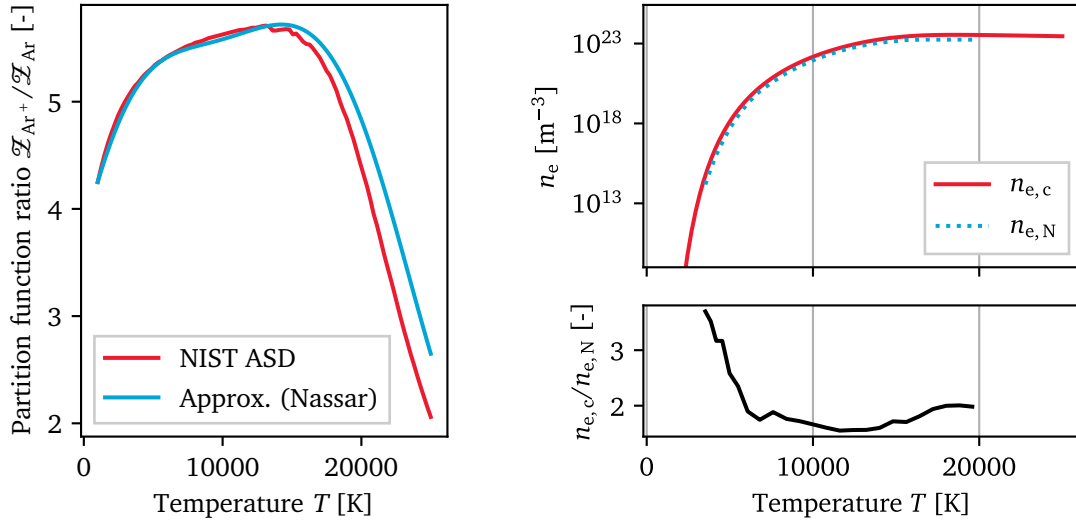
This approximation is plotted alongside the data directly retrieved from the NIST ASD in Figure 4.1a for comparison.

It is important to note that n_0 in Equation 4.1 is not constant across temperatures. In the case of LSP, the ionization process occurs at constant pressure, even if the experiment occurs in a closed container, as only a small fraction of the test section volume undergoes ionization. The hotter argon is free to expand into the cooler surroundings, locally reducing the number density and maintaining a constant pressure. Therefore, n_0 must be calculated based on a given pressure p and the varying temperature. This can be done with the ideal gas equation, where V is volume, N is the number of atoms in moles, R_u is the universal gas constant, and N_A is Avogadro's number:

$$\begin{aligned} pV &= NR_u T \\ p &= \frac{N}{V} R_u T \\ \frac{N_A p}{R_u T} &= n_0 \end{aligned}$$

The electron density n_e is plotted against temperature in Figure 4.1b, for a pressure of 1 bar. The calculation by Nassar is plotted alongside it, and their relative value is compared. While the electron density plots appear to agree, there remains a difference in density of a factor of two. This appears to be due to the use of lower precision physical constants in Akarapu *et al.* and Nassar's work.

Although electron density appears to plateau past 20 000 K, the caveat of this calculation is that it only considers single-ionization, i.e., removing a single electron from the atom. While this is valid below 20 000 K, second-degree ionization (removing a second electron away) begins past this temperature, increasing the number of electrons in the plasma. The plot is extended up to 25 000 K to provide some estimate of plasma properties, although they will not be as accurate as below 20 000 K.



(a) Ratio of Ar II to Ar I partition function values (b) n_e at 1 bar, and comparison between computed density $n_{e,c}$ and density $n_{e,N}$ reported by Nassar [64]

Figure 4.1: Computation of electron density n_e of argon

The absorption coefficient α can now be calculated with the known electron density. For convenience, the equation for α , Equation 2.2, is reproduced here:

$$\alpha = \frac{7.8 \times 10^{-7} Z n_e^2 \ln \Lambda}{\nu^2 (k_B T_e)^{3/2}} \left(1 - \frac{\nu_p^2}{\nu^2} \right)^{-1/2} \quad [\text{m}^{-1}] \quad (2.2 \text{ revisited})$$

Most parameters have been defined in Section 2.2, so the Coulomb logarithm $\ln \Lambda$ and the plasma frequency ν_p will be of interest here. The Coulomb logarithm is evaluated by Nassar [64] using a common approximation seen in plasma physics (Richardson [67]), with n_e in cm^{-3} and $T_{E,e}$ being the electron temperature in eV, i.e., $T_{E,e} = k_B T_e$.

$$\ln \Lambda \approx 23 - \ln (n_e^{1/2} Z T_{E,e}^{-3/2}) \quad (4.3)$$

However, alternate evaluations of the logarithm exist, such as the one given by Johnston and Dawson [27] in the specific context of IB absorption coefficient calculation (Equation 4.4).

$$\Lambda(\nu) = \begin{cases} \frac{\nu_T}{\nu \rho_{\min}} & \nu \gg \nu_p \\ \frac{\nu_T}{\nu_p \rho_{\min}} & \text{otherwise} \end{cases} \quad (4.4)$$

Where ν_T is the electron thermal velocity, ν is the laser frequency, ν_p is the plasma frequency, and ρ_{\min} is the impact parameter. These can be evaluated with the following equations:

$$\nu_T = \sqrt{\frac{k_B T}{m_e}} \quad (4.5)$$

$$\nu_p = \frac{1}{2\pi} \sqrt{\frac{e^2 n_e}{\epsilon_0 m_e}} \approx (8.978 85 \text{ m}^{3/2} \text{ s}^{-1}) \sqrt{n_e} \quad (4.6)$$

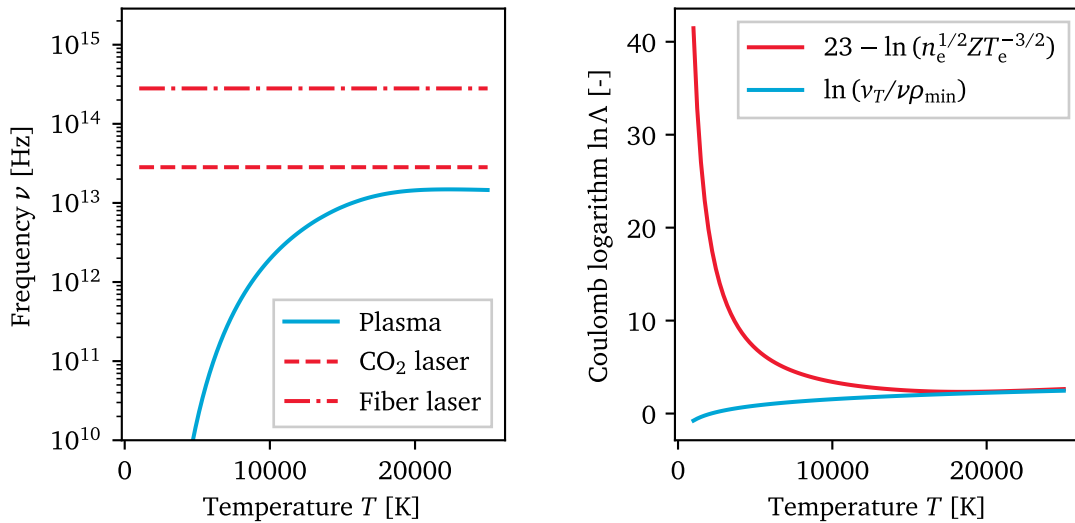
$$\rho_{\min} \approx \max \left(\frac{Z e^2}{k_B T}, \frac{\hbar}{(m_e k_B T)^{1/2}} \right) \quad (4.7)$$

It is not clear how the $Ze^2/k_B T$ quantity evaluates to a length, unlike $\hbar/\sqrt{m_e k_B T}$. Nevertheless, using a consistent system of units yields a value for the latter term several orders of magnitude greater than the former, resulting in a value of $\ln \Lambda$ that is relatively close to that obtained from Equation 4.3.

Johnston and Dawson [27] state:

...at frequencies well above the plasma frequency ν_p , $\ln \Lambda(\nu)$ should contain the wave frequency ν rather than the plasma frequency ν_p .

The respective frequencies of the plasma, CO₂ laser, and fiber laser are plotted in Figure 4.2a for comparison. It can be seen that for a fiber-laser-powered LSP, the $\nu \gg \nu_p$ case of Equation 4.4 is valid across the range of temperatures of interest, so Johnston and Dawson's statement is highly relevant in this case, and perhaps of lesser importance in Nassar's study. Furthermore, the fiber laser frequency is so much greater than the plasma frequency that $(1 - \nu_p^2/\nu^2)^{-1/2} \approx 1$ in Equation 2.2. As it was not clear whether the approximation of $\ln \Lambda$ in Equation 4.3 was applicable in this case, both evaluations of the Coulomb logarithm were compared in Figure 4.2b, showing that while there is a large divergence at lower temperatures, this is negligible as the argon is not in a plasma state. For temperatures of interest, namely above 10 000 K, both evaluations of the Coulomb logarithm appear to converge. Johnston and Dawson's form of the logarithm was retained for further calculations as it considers the relative values of the plasma and laser frequencies.



(a) Comparison of plasma and laser frequencies

(b) Comparison of computation methods

Figure 4.2: Calculation of the Coulomb logarithm, 10 bar

With values for the Coulomb logarithm and the plasma frequency, Equation 2.2 can be evaluated. Figure 4.3 plots the IB absorption coefficient for a range of temperatures and pressures. The point of peak absorption appears around the 20 000-K mark, with a sharp rise in peak absorption coefficient with increasing pressure. This is expected as α is proportional to n_e^2 on the first order, which increases with pressure. The occurrence of peak absorption appears to shift to greater temperatures as pressure increases.

The temperature of peak absorption is of interest, as it correlates to the peak temperature

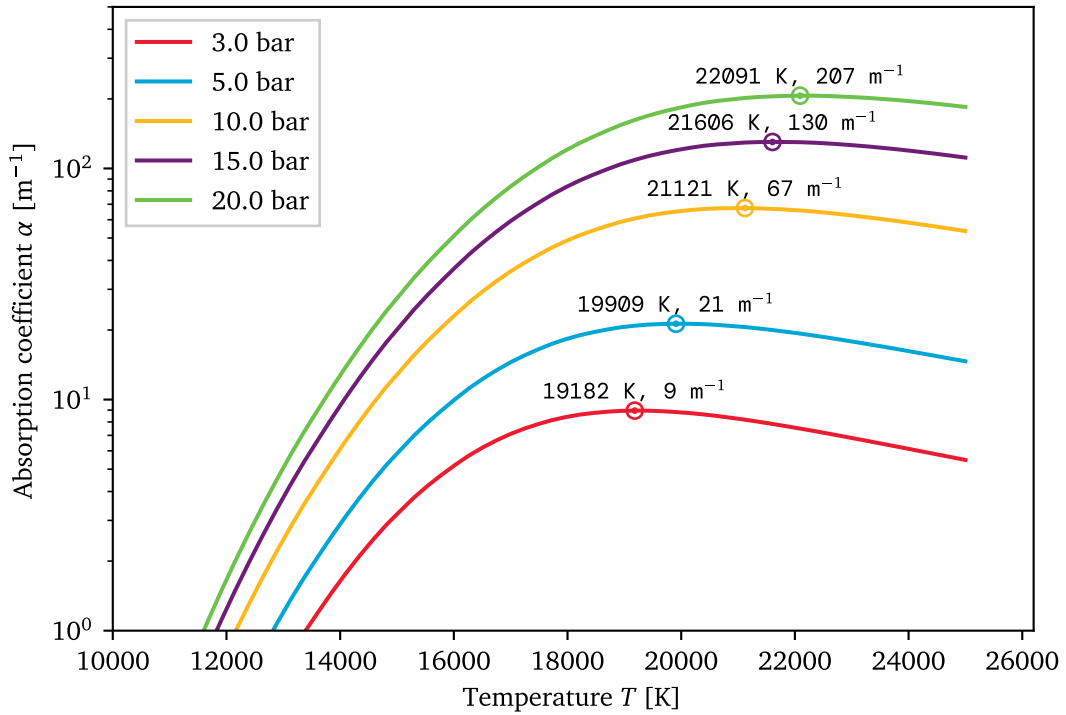


Figure 4.3: Inverse bremsstrahlung absorption coefficient of argon, 1070-nm radiation

of the LSP (Keefer [22]). This absorption model thus suggests that a peak temperature of around 20 000 K should be expected. Furthermore, the calculated absorption coefficient provides a scale length over which laser radiation will be absorbed by the LSP, by taking the reciprocal of α . For instance, at 10 bar of pressure and assuming complete absorption, the LSP length can be estimated to be close to the absorption length, i.e., $1/(67 \text{ m}^{-1}) = 15 \text{ mm}$. Experimental measurements of the fraction of laser power absorbed by the LSP can be used with the measured LSP length to compute an effective absorption coefficient, which can be compared to the predicted values in Figure 4.3, using the Beer-Lambert law.

4.2 LSP size estimate

Another avenue for LSP temperature estimate is to relate the average temperature and plasma volume, assuming the laser pulse energy is converted into enthalpy in the plasma volume. This calculation can then provide a range of LSP volumes and their associated average temperature. Figure 4.4 illustrates the simplified model of the LSP. The plasma volume is considered to be perfectly bounded by the laser beam and is approximated as a cone whose tip coincides with the laser focus. Knowing the beam geometry, i.e., the f-number $N_f = 7.9$, means that the cone's volume is only a function of the LSP length d .

$$\frac{d}{2r} = N_f \implies V = \pi \frac{d^3}{12N_f^2} \quad (4.8)$$

Starting with an initial temperature T_1 of 290 K, a final temperature T_2 will correspond to a change in enthalpy Δh . Given a set pulse energy E_{in} absorbed with efficiency η_α , the mass

m of gas required to increase in temperature from T_1 to T_2 can be found with Equation 4.9:

$$m = \frac{\eta_\alpha E_{\text{in}}}{\Delta h(T_1, T_2)} \quad (4.9)$$

This mass can then be converted to a volume V based on the density $\rho(T_2)$ of the gas at temperature T_2 .

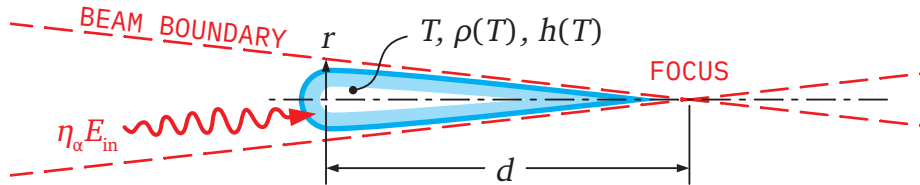


Figure 4.4: LSP sizing model

Unlike the heat deposition calculations discussed in the following section, the varying specific heat of argon must be considered, as it changes by an order of magnitude between 5000 and 20 000 K. At these temperatures, the ionization of argon consumes additional heat, so more of it is needed to increase its temperature. The thermodynamic properties of argon were obtained through NASA's CEA software [68] for a range of pressures and temperatures, and interpolated using cubic splines. The resulting specific heat at constant pressure and enthalpy are both plotted in Figure 4.5 for 10 bar of ambient pressure.

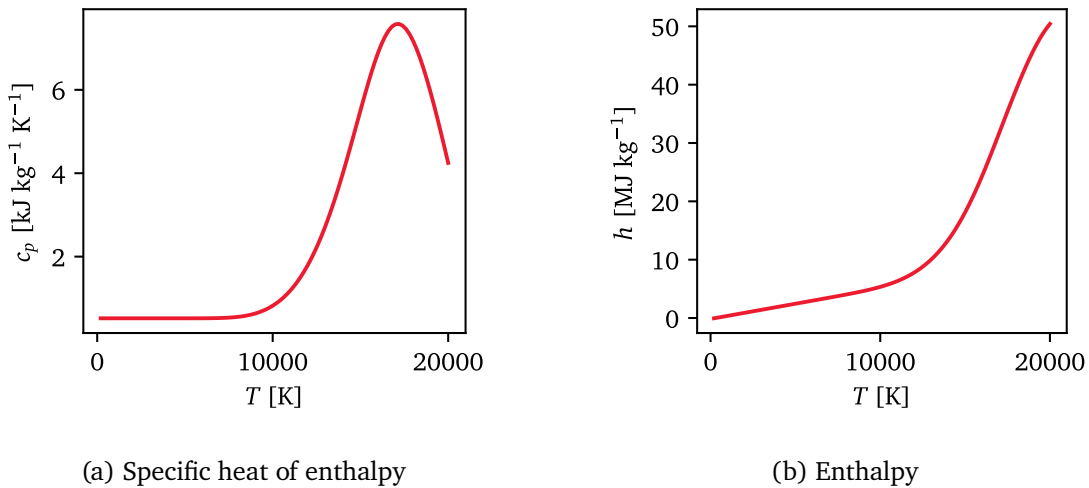


Figure 4.5: Thermodynamic properties of argon at 10 bar

The varying density $\rho(T)$ was also taken from CEA's output. Figure 4.6 shows the resulting LSP dimensions based on a range of possible final temperatures. The calculation was performed for two pressures and assuming both complete and 50% laser absorption by the plasma. The results suggest that in the range where ionization is expected and IB absorption is possible, i.e., above 10 000 K, the volume of plasma that would contain the energy of a full-power pulse is on the order of 1000 mm³, corresponding to LSP lengths ranging from

70–140 mm. Although not a perfect match, this loosely corresponds to the scale absorption lengths suggested by the IB absorption calculation in [Section 4.1](#), especially at higher temperatures.

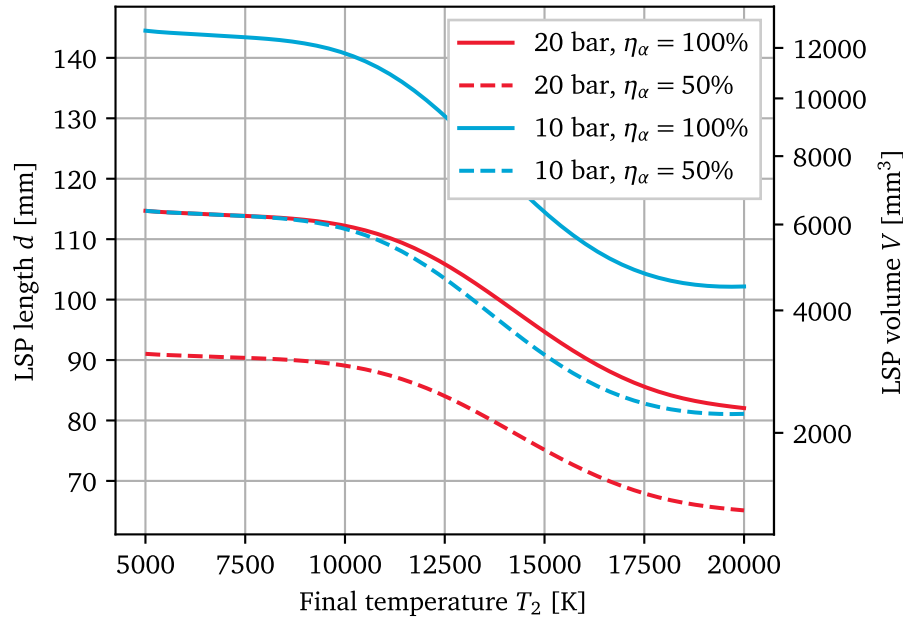


Figure 4.6: LSP dimension estimate for 30 J pulse, assuming conical volume

This model of LSP sizing does have a few caveats. First, it assumes that the plasma envelope is adiabatic—none of the heat deposited into the plasma is transferred out within the duration of a laser pulse. In reality, heat will likely be lost through radiation and conduction as the plasma grows. Second, the plasma temperature will not be uniform, as seen in the data from Welle *et al.* [31] ([Figure 2.3b](#)), and a portion of the plasma will lie outside the laser-beam boundaries. These effects will likely result in a smaller than estimated plasma volume/length, as less heat will be contained in the plasma envelope at any given time and a portion of this heat will be contained in lower-temperature regions.

4.3 Test-section heating

Some calculations were performed in the interest of safety and selecting appropriate instrumentation to predict the rise in temperature and pressure of the test section during an experiment. As discussed in [Table 3.1.2](#), precise pressure measurements will be taken during the experiment to estimate the heat deposition resulting from successful LSP ignition. The following scenarios are considered:

1. Failed ignition
2. Successful ignition
 - (a) ...in the static case (constant volume)
 - (b) ...in the flowing case (constant pressure)

The apparatus used in this project is mostly made of stainless steel and 6061 aluminum, and argon is the working fluid. Some relevant thermodynamic and structural properties are given in [Appendix I](#).

4.3.1 Failed ignition

In the case of failed ignition, most of the laser radiation will be directly incident on the backplate of the test section. This is the worst case scenario—alternatively, a window module could be present, allowing the laser beam to be safely dumped into the power meter, resulting in virtually no heating of the test section itself. The opaque backplate used in this experiment is made of 6061 aluminum. It can be approximated as a disk 3.94 in in diameter and 0.39-in thick, giving it a mass of approximately 0.2 kg and a heat capacity of 180 J K^{-1} . The worst-case temperature rise can be estimated assuming all the laser energy is absorbed by the plate as heat.

It is immediately apparent that distributing the energy of a full-power laser pulse (30.8 J) will lead to a negligible temperature rise—less than 0.2 K. The portion of the plate directly exposed to the laser beam will likely experience a higher temperature, but the beam diameter is approximately 2 cm by the time it reaches the backplate, so local laser intensity will not be sufficient to cause any damage or to raise the surface temperature by more than a few K. In the CW scenario, with up to 350 W deposited into the plate, the plate temperature is unlikely to rise by more than 10–20 K in the time it would take to determine that no ignition had occurred and to shut down the laser, i.e., around 10 s.

In reality, the resulting temperature rise is likely to be much lower, as aluminum will reflect most of the laser radiation: Pozzobon *et al.* [69] reported 96–98% reflectivity in the near-infrared spectrum. The diffuse reflection (up to 75%) will distribute the laser radiation across several parts of the apparatus, minimizing local temperature rises. Laser damage to the facility in the event of a failed ignition is thus of minimal concern.

4.3.2 Successful ignition

In the case of successful ignition, several scenarios are possible depending on whether the laser is operated in pulsed or CW mode and whether the working fluid is static or flowing through the test section. Two scenarios will be considered: the effect of a laser-pulse-sustained plasma in static argon, as it is the most relevant to the experiments performed in this project, and the effect of continuous LSP in flowing argon, as this is the scenario most relevant to operating a thruster prototype.

Laser-pulse LSP in static argon

Assuming an even distribution of heat added into a closed system, the resulting pressure change Δp can be expressed using the ideal gas equation and the change in temperature ΔT caused by a constant volume heat addition Q_{in} . In this case, Q_{in} refers to the heat deposition in the working fluid, not the laser-pulse energy entering the test section, which will be defined as E_{in} .

$$pV = mR_g T \quad (4.10)$$

$$Q_{\text{in}} = mc_v \Delta T \quad (4.11)$$

The change in pressure and temperature of this system can be determined between two states (1 and 2) as follows:

$$\begin{aligned}
 \frac{p_1}{T_1} &= \frac{mR_g}{V} = \frac{p_2}{T_2} \\
 \implies \frac{T_2}{T_1} &= \frac{p_2}{p_1} \\
 \implies \frac{T_1 + \Delta T}{T_1} &= \frac{p_1 + \Delta p}{p_1} \\
 \implies \frac{\Delta T}{T_1} &= \frac{\Delta p}{p_1} \\
 \implies \frac{p_1}{T_1} \Delta T &= \Delta p
 \end{aligned}$$

Substituting p_1/T_1 with [Equation 4.10](#) and ΔT with [Equation 4.11](#), the static pressure change in the test section can be related to the heat added in the system and vice-versa:

$$\Delta p = \frac{R_g Q_{\text{in}}}{V c_V} \quad (4.12)$$

The specific heat at constant volume c_V is taken to be that of room-temperature-and-pressure argon: $312 \text{ J kg}^{-1} \text{ K}^{-1}$ [70]. Although the specific heats of argon vary significantly as it heats to a plasma state, this analysis considers the final state of the system, whose temperature is not expected to increase to a point where variable specific heats should be considered. The resulting change in pressure is independent of the gas mass, and therefore, independent of the initial pressure for a set volume. This initial-pressure independence however only holds as long as the heat deposited in the gas Q_{in} is also independent on the initial pressure.

The heat-deposition efficiency can then be defined as $\eta = Q_{\text{in}}/E_{\text{in}}$. Approximating the volume V of the test-section as a cylinder matching the internal dimensions annotated in [Figure 3.3c](#) (315×38 -mm cylinder) allows the prediction of the measured pressure change resulting from an LSP test. These results are shown for a range of laser-pulse energies in [Figure 4.7a](#). Although the pressure rise is independent of the initial pressure, the temperature rise is not. Indeed, lower initial pressures result in a lesser gas mass to absorb the deposited heat, resulting in a greater final temperature. As seen in [Figure 4.7b](#), the same pulse providing a ~ 1 -K temperature rise at 20 bar would raise the temperature by almost 10 K at 3 bar.

Two assumptions made in this model may not be accurate. First, this model assumes that the heat deposited by the LSP in the working gas is distributed evenly in the test section before it has time to be transferred to the test section walls. This may not be the case, so numerical simulations may be necessary to ascertain the validity of this assumption. Second, this model assumes that the heat-deposition efficiency does not change with pressure/density, when a denser gas could contribute to improved heat deposition through more effective heat conduction and/or greater absorption of radiated heat.

The predicted state changes for this experiment are still low when considering thrust applications. As will be discussed in [Section 4.4](#), both thrust and specific impulse depend on $T^{1/2}$. In case of low heat-deposition efficiency, a temperature change of a few K will

likely only modify thrust and specific impulse by a few percent or less from the cold-flow case. It is thus already apparent that the current test-section design is unoptimized for thruster experiments, and these calculations indicate that thrust chamber volume should be decreased to amplify the changes in pressure and temperature during LSP operation.

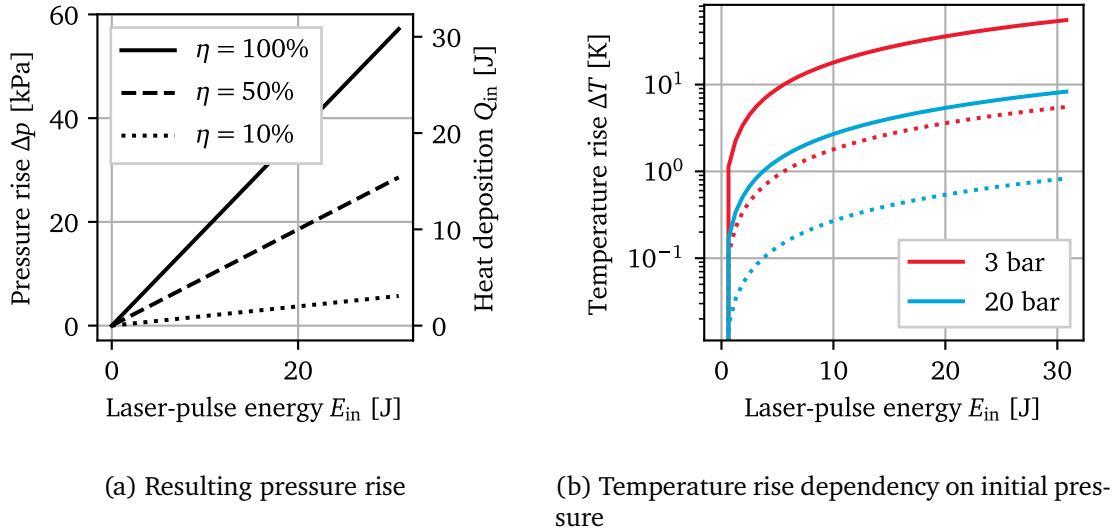


Figure 4.7: Effect of pulse LSP on test-section conditions

CW LSP in flowing argon

The CW flowing case is most akin to a real thruster operation. In this scenario, the resulting steady-flow temperature rise can be calculated for a range of mass-flow rates and a constant laser power input of 350 W. This is a constant-pressure process, unlike the static LSP case. For steady flow, the temperature change from T_1 (room temperature) to T_2 due to a heat addition rate \dot{Q}_{in} can be determined from its change of enthalpy as follows:

$$\eta P_{in} = \dot{Q}_{in} = \dot{m}(h(T_2) - h(T_1)) \quad (4.13)$$

Where P_{in} is the laser power and η is the heat-deposition efficiency. This equation can be solved for T_2 , the resulting bulk temperature at the inlet of the thruster nozzle. Again, variable specific heat data from NASA CEA [68] will be considered to determine what mass flow rates are necessary to attain temperatures expected in an actual LTP system, i.e., 10^3 – 10^4 K.

Figure 4.8 shows the result of this calculation for mass-flow rates ranging from 0.03 to 30 g s^{-1} and a chamber pressure of 10 bar. At this low laser-power level, low mass-flow rates of 1 g s^{-1} or less appear necessary to raise the propellant temperature to those expected in an LTP thruster. In the best case conditions, the theoretical 10 000-K chamber temperature reported by Duplay *et al.* [12] for a full-scale thruster can only be replicated in the lab with a 0.06-g s^{-1} flow rate. Temperature increases appear negligible for flow rates beyond 20 g s^{-1} .

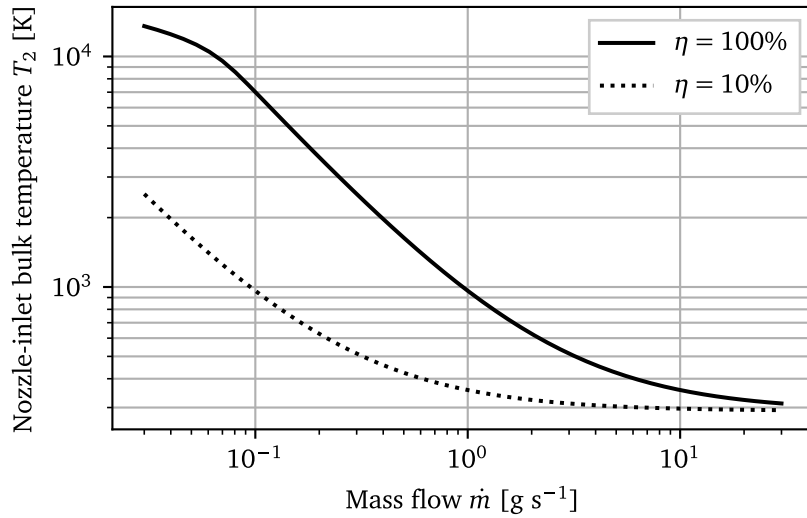


Figure 4.8: Expected flow temperature at nozzle inlet, 10 bar, 350 W of input laser power.

4.4 Thrust modelling

Sizing thruster and thrust-stand components requires the calculation of theoretical performance parameters such as the expected thrust and exhaust velocity. These parameters should be calculated for a range of operating conditions, which include the chamber pressure, the laser power, and the mass flow rate. Given the number of factors affecting thrust, a complete study of the operating range and theoretical performance of a prototype thruster could be the subject of its own thesis. Therefore, three specific scenarios (tabulated in Table 4.1) will be studied in detail:

- **CW20:** CW laser input at maximum power (350 W). At this power level, the minimum pressure allowing a stable LSP is 20 bar according to Zimakov *et al.* [30]. This is thus the only operating scenario in which the LTTLM could be operated continuously.
- **P20:** Full-power (3080 W) laser pulse generating LSP at 20 bar.
- **P3:** At 3 bar, the LSP power threshold is approximately 3 kW. This is the lowest pressure at which the LTTLM could theoretically be operated with the available laser.

Table 4.1: Operating scenarios for the LTTLM, $p_{c,1}$ is the initial chamber pressure and \dot{Q}_{in} is the input power.

Scenario	$p_{c,1}$ [bar]	\dot{Q}_{in} [W]	Laser mode
CW20	20	350	CW
P20	20	3080	Pulsed
P3	3	3080	Pulsed

The thrust F_T of a thermal rocket engine can be determined with Equation 4.14, where T_c is the chamber temperature, p_{ex} is the exhaust pressure, p_c is the chamber pressure, A_{ex} is

the nozzle exit area, and p_a is the ambient pressure.

$$F_T = \dot{m} \sqrt{\frac{2\gamma}{\gamma-1} R_g T_c \left(1 - \left(\frac{p_{ex}}{p_c} \right)^{\frac{\gamma-1}{\gamma}} \right)} + A_{ex} (p_{ex} - p_a) \quad (4.14)$$

In this case, the thruster will exhaust to atmosphere, so p_a will be set to 1 bar. The following simplifying assumptions will also be made:

1. The mass-flow rate \dot{m} into the thruster will be held constant. This is achievable in practice by setting up the system in a *double-choked* configuration, where the inlet port is a choked orifice whose mass-flow rate is only dependent on upstream stagnation conditions. The flow can then choke again at the thruster's nozzle throat, provided a normal shock occurs between the inlet port and the thrust chamber. For the sake of brevity, a complete flow analysis will not be given, but this configuration is theoretically possible and is considered for the next iteration of the LTTLM, which is in development at the time of writing this report.
2. The thruster nozzle will be assumed to be a simple orifice with no diverging section, meaning that the exit pressure p_{ex} is equal to the flow's sonic pressure p^* , i.e., the pressure of the flow as it reaches sonic conditions. The sonic pressure is a function of stagnation pressure p_c and the specific heat ratio γ of the gas:

$$p^* = p_c \left(\frac{2}{\gamma+1} \right)^{\frac{\gamma}{\gamma-1}} \approx 0.5 p_c \text{ (Argon)} \quad (4.15)$$

The choked orifice is the simplest, albeit unoptimized, nozzle configuration. Adding a diverging section would not fundamentally change the flow conditions in the thruster; it would merely improve thrust and specific impulse.

3. Finally, argon will be treated as a perfect gas, i.e., c_p and γ are constant. This is a valid assumption for argon until ~ 5000 K [68]. As the intent of the LTTLM is not yet to attain such high temperatures, this is a suitable simplification.

4.4.1 Cold-flow conditions

Starting the thruster will involve a cold-thrust stage (denoted with the subscript 1) before the laser is turned on. Flow conditions should stabilize such that the desired chamber pressure is attained. In this case, the chamber temperature remains close to room temperature T_a (290 K). For a desired mass-flow rate and chamber pressure, the nozzle exit area (i.e., the orifice size) is fully constrained by the [Equation 4.16](#)¹ for the choked mass-flow rate.

$$\begin{aligned} \dot{m} &= \sqrt{\frac{\gamma}{R_g} \left(\frac{2}{\gamma+1} \right)^{\frac{\gamma+1}{\gamma-1}} \frac{A_{ex} p_c}{\sqrt{T_c}}} = K_{\dot{m}} \frac{A_{ex} p_c}{\sqrt{T_c}} \\ \implies A_{ex} &= \frac{\dot{m}}{K_{\dot{m}}} \frac{\sqrt{T_a}}{p_{c,1}} \end{aligned} \quad (4.16)$$

¹Equivalent to Equation 6-6 in Zandbergen's *AE4-S01 Thermal Rocket Propulsion* course notes [23]

For the temperatures of interest in the overall flow (excluding the LSP), K_m for argon is $0.0504 \text{ s K}^{1/2} \text{ m}^{-1}$. For those familiar with the Vandekerckhove function Γ , the mass flow parameter K_m is equivalent to $\Gamma/R_g^{1/2}$.

The orifice area A_{ex} is then assumed to remain constant throughout both cold-flow and hot-fire conditions—no variable geometry nozzles are currently planned for the thruster prototype. The thrust equation Equation 4.14 can now be evaluated for cold flow conditions. Figure 4.9 shows the variation in thrust and the nozzle dimension for a mass-flow rate ranging from 1–10 g s^{-1} . The cold thrust appears to remain on the order of 1 N regardless of chamber pressure, although the difference between 3 bar and 20 bar appears to grow at greater mass-flow rates. The nozzle diameter exhibits a more significant difference between both chamber pressures. It should be noted that the CW20 and P20 scenarios are perfectly superposed—this is normal since the only difference between both cases is the laser power, which is not active at this stage.

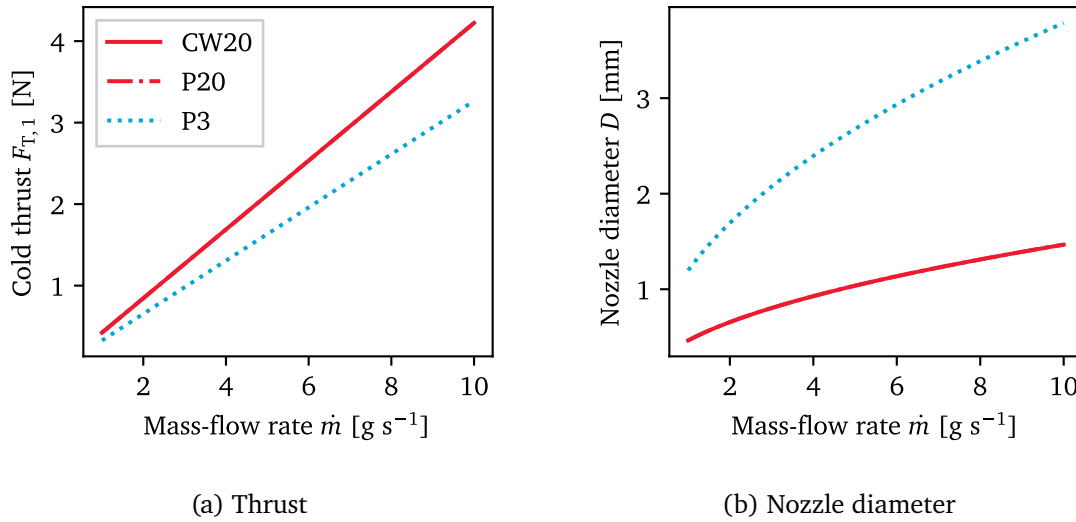


Figure 4.9: Cold gas thruster parameters. Legend is shared between both plots.

Although the thrust increases with \dot{m} , the exhaust velocity v_{ex} is unaffected by the mass-flow rate—its value for each scenario is tabulated in Table 4.2. The equivalent exhaust velocity v_{eq} is also given. This term combines the true exhaust velocity with the pressure thrust $A_{\text{ex}}\Delta p_{\text{ex}-a}$ normalized by mass-flow rate. The equivalent exhaust velocity is commonly used to simplify calculations for rocket trajectories and mission planning, as no special attention must be given to pressure-thrust effects. The specific impulse I_{sp} is also commonly used to report rocket engine exhaust velocities. These various forms of expressing the exhaust velocity are related by the following equations:

$$\begin{aligned}
 F_T &= \dot{m}v_{\text{ex}} + A_{\text{ex}}(p_{\text{ex}} - p_a) \\
 v_{\text{eq}} &= v_{\text{ex}} + \frac{A_{\text{ex}}(p_{\text{ex}} - p_a)}{\dot{m}} \\
 I_{\text{sp}} &= \frac{v_{\text{eq}}}{g_0} \\
 \implies F_T &= \dot{m}v_{\text{eq}} = \dot{m}I_{\text{sp}}g_0
 \end{aligned}$$

Where g_0 is the standard gravitational acceleration. For the rest of this analysis, the *equivalent* exhaust velocity v_{eq} will be reported, as the true exhaust velocity is of lesser interest.

Table 4.2: Cold-flow (stage 1) exhaust velocities: v_{ex} is the real exit flow velocity, v_{eq} is the equivalent exhaust velocity, and I_{sp} is the specific impulse based on v_{eq} .

Scenario	$v_{\text{ex},1}$ [m s^{-1}]	$v_{\text{eq},1}$ [m s^{-1}]	$I_{\text{sp},1}$ [s]
CW20	275	422	43
P20	275	422	43
P3	275	327	33

Again, there is no difference in the resulting exhaust velocity between the CW20 and P20 scenarios. This is not surprising considering the chamber pressure is identical, and the use of an orifice nozzle means that the p_{ex}/p_c ratio reduces to a function of γ , which is identical in both cases. P3 yields a lesser equivalent exhaust velocity than the other two scenarios as the pressure thrust is decreased.

4.4.2 Hot-fire conditions

Once cold-flow conditions have been established, the laser is turned on and LSP is assumed to be ignited successfully. The flow is expected to adjust to the heat addition, resulting in new, hot-fire flow conditions (stage 2). The heat deposition is assumed to be 100% efficient and results in a change in chamber temperature as modelled in [Equation 5.5](#). The perfect gas assumption does simplify the model as follows:

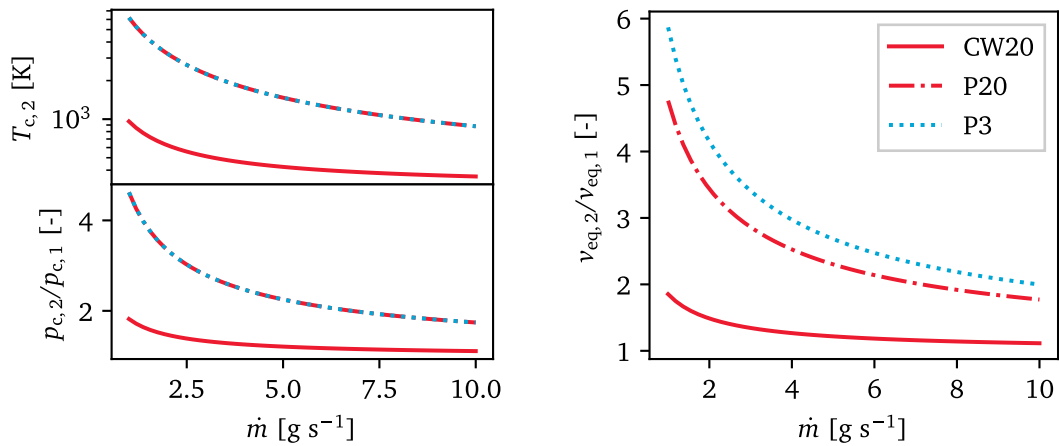
$$T_{c,2} = T_{c,1} + \frac{\dot{Q}_{\text{in}}}{\dot{m}c_p} \quad (4.17)$$

Where $T_{c,1}$ is the chamber temperature in state 1, i.e., T_a .

Under the assumed constant mass-flow rate conditions, this increase in temperature must lead to an increase in chamber pressure p_c . Indeed, by examining conservation of mass:

$$\begin{aligned} \dot{m}_1 &= \dot{m}_2 \\ \implies K_{\dot{m}} \frac{A_{\text{ex}} p_{c,1}}{\sqrt{T_{c,1}}} &= K_{\dot{m}} \frac{A_{\text{ex}} p_{c,2}}{\sqrt{T_{c,2}}} \\ \implies \frac{p_{c,1}}{\sqrt{T_{c,1}}} &= \frac{p_{c,2}}{\sqrt{T_{c,2}}} \end{aligned}$$

Since the nozzle area cannot be changed, the only way to maintain the same mass flow is to increase the chamber pressure. [Figure 4.10a](#) shows the new chamber temperature and the change in chamber pressure resulting from the heat addition. The chamber temperature is in good agreement with [Figure 4.8](#), where variable specific heat was considered. Here, both P20 and P3 are perfectly superposed, as they share the same rate of heat addition. Since the increase in temperature is dependent on the mass-flow rate, the order-of-magnitude difference in input power between the CW and pulsed laser results in a similar difference in chamber temperature.



(a) Chamber temperature and change in pressure

(b) Ratio of equivalent exhaust velocity

Figure 4.10: Change in operating parameters between cold (1) and hot (2) flow. Legend is shared.

The change in pressure is also significant. A two-fold increase in chamber pressure is observed for a 3-kW input power (P20 and P3) at a 10-g s⁻¹-mass-flow rate, and this pressure ratio increases to above 4 at 1 g s⁻¹. The CW20 case approaches a two-fold increase in pressure at 1 g s⁻¹. This has major implications in the thrust-chamber design: in the P20 and CW20 case, this would mean an operating pressure of around 80 bar and 40 bar, respectively—significantly greater than the current test section’s design pressure. Furthermore, in order to maintain a constant mass-flow rate at the inlet port, the chamber pressure *must* remain below the reservoir’s sonic pressure, i.e., around half of the reservoir’s stagnation pressure (Equation 4.15). This suggests that unless the feed system can be designed to respond to this pressure change, the reservoir’s pressure should be an order of magnitude greater than the cold-flow operating pressure $p_{c,1}$. The increase in chamber pressure does have a benefit: this moves the thruster operating point further beyond the LSP power threshold, which should facilitate the maintenance of the plasma.

The change in exhaust velocity is shown in Figure 4.10b. Although P20 and P3 exhibit the same relative pressure change and have the same $T_{c,2}$, a greater relative change in exhaust velocity is observed in the P3 scenario. This is due to a difference in pressure thrust: since P3 uses a larger nozzle for a given mass-flow rate (as seen in Figure 4.9b), the contribution of the pressure thrust to the equivalent exhaust velocity is proportionally greater. The CW20 scenario exhibits a change in exhaust velocity that mirrors its change in chamber pressure. The use of equivalent exhaust velocity over the real exhaust velocity is convenient here: since the thrust is directly proportional to v_{eq} , the relative change in equivalent exhaust velocity is the same as the relative change in thrust $F_{T,2}/F_{T,1}$.

Figure 4.11 shows the final thrust performance figures of an LTP thruster model powered by the laser used in this project. Ultimately, the thruster-operation mode described here makes a change in pressure from 3 bar to 20 bar unimportant compared to a difference in power input: both the P20 and P3 scenarios have similar thrust levels across the given mass-flow-rate range (although, again, the difference grows at greater \dot{m}). Although noticeably lower,

the thrust level of the CW20 scenario is still somewhat comparable: all three scenarios result in thrust on the order of 1 N. Detecting a noticeable change in exhaust velocity and/or thrust between cold and hot flow will however require mass-flow rates closer to 1 g s^{-1} . The expected exhaust velocities range from 500 m s^{-1} for the CW20 case to up to 2 km s^{-1} for the pulse-laser cases. Here again, the pressure difference between P3 and P20 result in only a minor change in exhaust velocity.

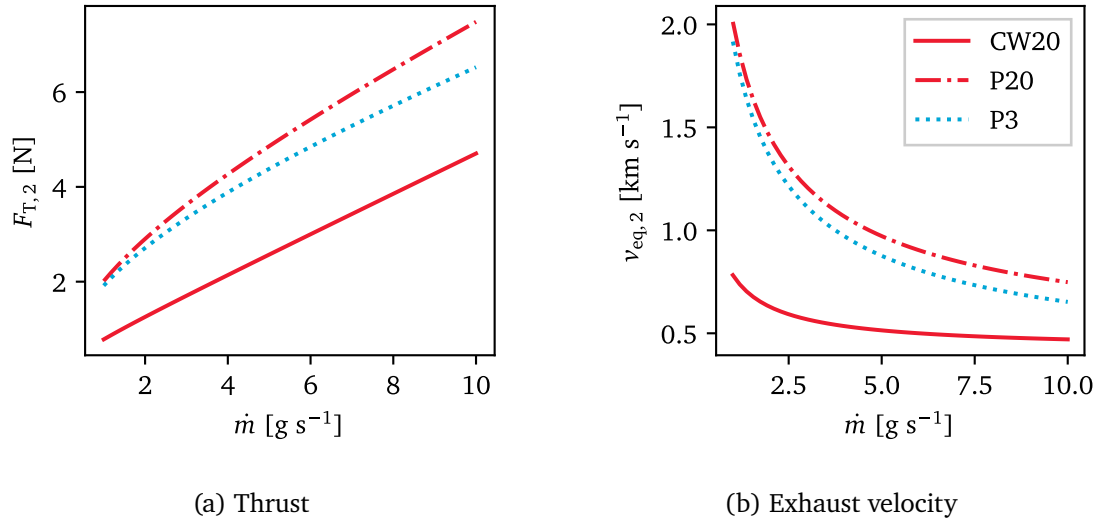


Figure 4.11: Thrust and exhaust velocity, hot-fire conditions

4.4.3 Limitations

Although this analysis provides some valuable insight into the possible operation of a lab-scale LTP thruster and yields concrete performance estimates, the validity of its assumptions must be discussed to determine to what degree these performance predictions will apply to real tests. The most questionable assumption is likely the 100% heat-deposition efficiency from the laser to the working fluid. The thruster tests of Toyoda *et al.* [45] suggest that a far lesser heat-deposition efficiency is to be expected in real-world conditions, likely due to significant radiative heat losses to the thruster walls. The use of regenerative cooling could potentially alleviate this issue, but the use of more aggressive heat retention methods, such as gas seeding proposed by Shoji and Larson [13], may be required to approach this idealized heat-deposition efficiency. If the difference in operating parameters between the P20 and CW20 scenarios is indicative, an order-of-magnitude reduction in exhaust velocity could be expected, along with a $\sim 50\%$ reduction in thrust. This analysis also does not consider boundary-layer effects, which may be significant based on the expected nozzle sizes—one of their potential effects is an effective reduction in the nozzle area, leading to a greater pressure than expected to achieve the same mass-flow rate.

The P20 and P3 cases are also idealized in the sense that these calculations assume that a steady flow and heat transfer is established within the span of a 10-ms laser pulse, which is unlikely. Studying these cases does provide some understanding of the effect of increased laser power compared to the CW case, which should be analogous to a difference in heat-deposition efficiency. The CW20 case remains the most representative scenario for thrust testing.

The takeaway from this analysis is that a well-sized load-cell should likely have a minimum resolution on the order of 0.01 N and a maximum load rating of around 1 N, much lower than the 10–20 N stated in the TS-2 thrust-stand requirement (Table 3.5). This was a preliminary requirement set to allow for the use of relatively large nozzles, larger than necessary for dedicated thrust testing. As discussed in Section 5.6, these larger nozzles allowed for bulk flow velocities in the test-section high enough to affect the LSP. In addition, as the project progressed, it quickly became apparent that the selected test-section was unoptimized for thrust testing, as its mass made it difficult to design a thrust stand that could appropriately measure its thrust. The requirements were thus not revised following in-depth thrust modelling. The analysis presented here will however inform the design of a dedicated LTP thruster model and thrust stand, in development at the time of writing.

Chapter 5

Experiments

The results of the first experiments performed on the LSP facility are presented here. These include an exploration of ignition methods and their reliability, the attempted replication of power-threshold experiments seen in LSP literature, and the analysis of LSP's absorption, heat deposition, and spectral characteristics. Preliminary flowing data is also presented and contrasted with the static case.

Figure 5.1 provides an overview of the instrumentation used in static experiments and their relative positions. All experiments were performed with a 200-mm-focal length lens, focusing the 1-in-wide laser beam to a focus approximately 0.5 mm in diameter. These parameters result in an effective f-number of 7.9 for the laser beam. The working fluid is argon, chosen for its safer handling characteristics over hydrogen or nitrogen, as discussed in Chapter 2.

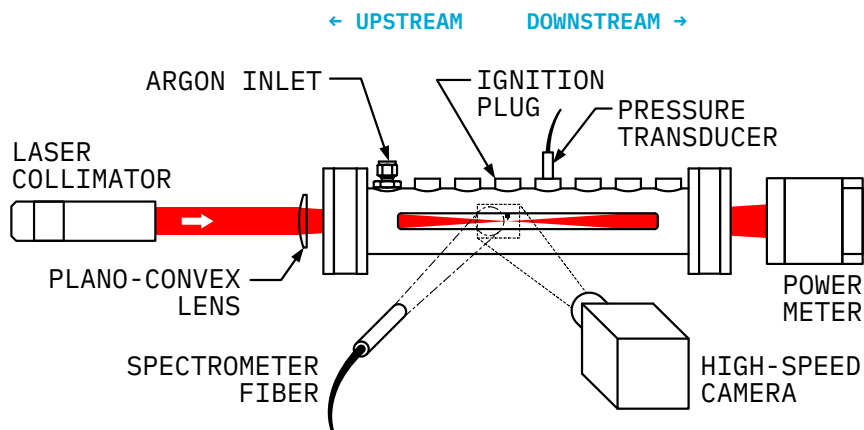


Figure 5.1: Static configuration of the test section

A summary of the experiments/tests performed, along with their goal and success criteria, is presented in Table 5.1. The experiments performed in this chapter involve one subsystem test (ignition), and the collection of data relevant in studying the laser absorption and heat deposition effectiveness of LSP.

Table 5.1: Overview of experiments/tests, goals, and success criteria

Experiment/Test	Goals	Success criteria
Ignition test	Test and fine-tune ignition methods	90% reliability
Power threshold	Identify minimum power needed to sustain plasma for 3–20 bar	-
Laser absorption	Determine absorption coefficient in agreement with literature/models	-
Heat deposition	Estimate heat deposition using static pressure measurements	-
Spectroscopy	Estimate peak plasma temperature using emission spectrum	-
Flowing experiment	Compare measured data to static case	-

5.1 Preliminary ignition tests

Once the necessary components of the experiment were integrated, a preliminary testing campaign began to attempt to ignite LSP. Two ignition methods were tested—both are designed to generate a seed cloud of free electrons able to initiate the IB absorption process, which can only sustain itself in ionized argon ($T > 1000$ K). The hope was to resolve any unforeseen practical issues, then quickly move on to replicating the power threshold experiments of past LSP literature [30, 44, 46]. The test campaign aimed to answer two questions:

- Can LSP be achieved with this experimental setup?
- How reliable is LSP ignition with this system?

To answer these questions, experimental trials would be run in conditions most favorable to steady LSP formation, i.e. at maximum laser power and maximum test section pressure: 3 kW and 20 bar. Successful ignition would be determined based on two independent measures:

1. The high-speed camera should be able to image the LSP growing and propagating towards the laser source over the course of the laser pulse, as consistently documented in LSP literature.
2. A measurable drop in laser energy reaching the Gentec power meter should be observed.

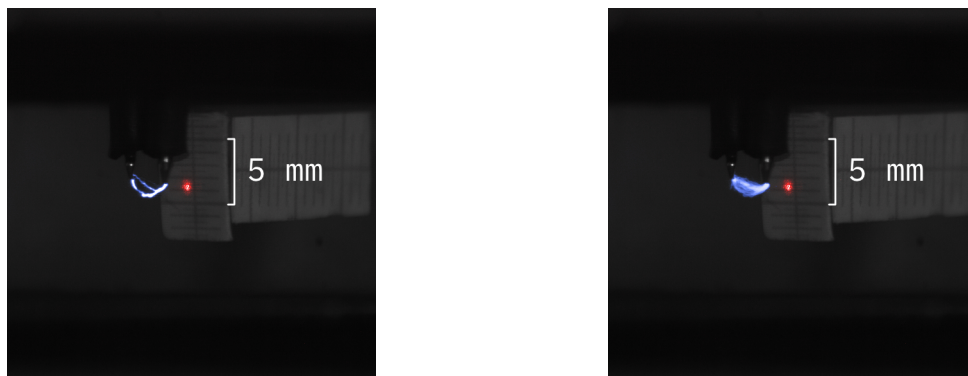
LSP would only be deemed to have successfully ignited if the expected behavior was observed with both instruments.

5.1.1 Spark ignition

Laser alignment was immediately found to be a non-trivial problem. In order to successfully ignite the LSP, the laser must be focused onto the arc generated by the spark igniter. To maximize the chance of ignition, the laser flux at the arc must be as great as possible, so

the focused laser dot must be as small as possible. This makes alignment tolerances much stricter, as the laser is less likely to be incident on the thin arc at all.

Compounding this issue was the fact that the path taken by the arc between both electrode tips was not consistent. As seen in [Figure 5.2](#), the location of the arc was highly variable: although an average arc path could be determined, the arc could form up to 1 mm away. This made it impossible to ensure consistent alignment between the arc and the laser focus. This issue could be alleviated by repeatedly triggering the spark, but the smart coil had a nominal delay of 3 ms between sparks, only allowing up to three ignition attempts within a single laser pulse, making this approach of little viability for high-power pulse laser tests. Repeated sparks could be used with CW laser operation at 300 W, but the lower laser power also reduces the likelihood of successful LSP ignition.



(a) Single arc generated by the spark igniter

(b) Several arcs stacked together to create a “heatmap” of arc formation. Note the large variance in the path taken by the arc.

Figure 5.2: Composite photos made during a typical spark–laser alignment procedure. The gray-scale background, blue arcs, and red guide laser photos were taken separately then stacked together to be able to compare the relative position of the arcs and laser.

In addition, the laser could not be aligned without placing reflecting or scattering material in the beam path. As seen in [Figure 5.2](#), a target must be placed near the ignition point to perform the alignment (and also serves as a scale indicator). However, this alignment target had to be removed to pressurize the test section, which was required both to determine the spark location, and to perform the LSP ignition test. Pressurization cycles and the placing/removal of this target made the alignment process slow and cumbersome. Alignment with the arcs could not be confirmed visually since the target could not be present when pressurizing the test section.

Despite these difficulties, several attempts were made to ignite LSP with this method, and a few were successful. The first successful test was performed at 10.0 bar with a full power pulse (30.8 J). A paper target had been placed next to the electrodes to facilitate alignment, so no measurements were made of the pulse energy transmitted through the plasma for the first few successful tests. However, high-speed footage showed strong evidence of plasma formation: a bright flash saturating the camera sensor, igniting at the time of spark formation, as seen in [Figure 5.3](#). Such a flash had never been observed in past (failed) ignition tests. Although this suggested that some plasma had been formed, there was a possibility that the alignment target was affecting the experiment and may even have contributed to the ignition. The footage showed evidence of particles being ejected from the

area around the ignition point, possibly due to the interaction between the laser, plasma, and the paper target.

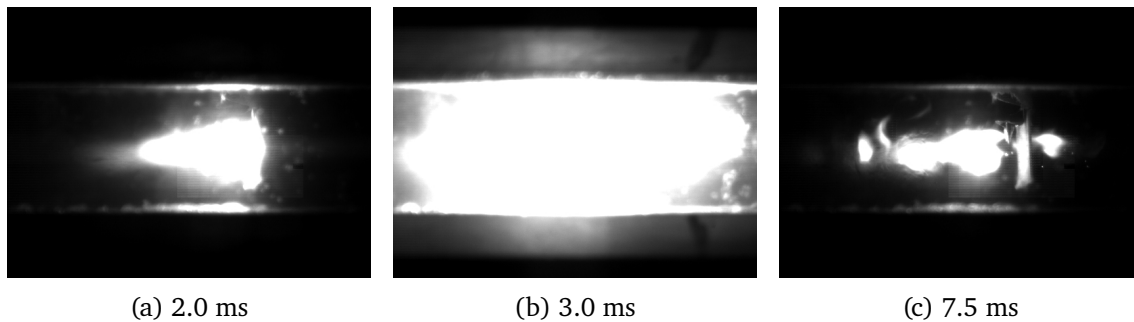


Figure 5.3: High-speed footage frames of first successful LSP ignition. The horizontal reflections above and below the event are the edges of the observation window.

The experiment was repeated with the target several times, ensuring that the flash was not the result of merely burning a hole through the paper target. In addition, the exposure settings were adjusted (increasing the ND filter to ND2048 and setting the aperture to $f/22$) to provide a clearer view of the brightest part of the frame, the LSP core. A snapshot of the resulting footage is shown in Figure 5.4, revealing a slender plasma core, approximately contained within the focused laser beam (note the thinner right tip of the LSP compared to the left tip). The plasma was observed to grow towards the source of the laser, as reported in the experimental LSP literature. This appearance and growth behavior provided additional evidence that these tests were truly achieving laser-sustained plasma, as opposed to some other phenomenon.

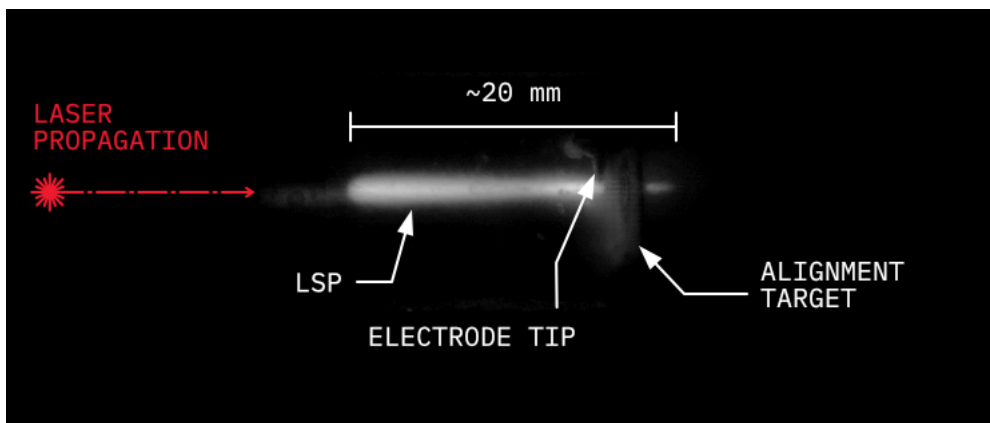


Figure 5.4: Third successful LSP test ignited by arc discharge. Snapshot from just before the end of the laser pulse. Dimension is approximate.

To provide complete confidence that this indeed was LSP, more experiments were performed without the paper target. This allowed the measurement of the laser energy that was not absorbed by the plasma and would confirm that the LSP is ignited purely by the spark, as opposed to ablated material from the paper target. With a fully uninterrupted beam path, the power meter reported a 70 to 80% drop in laser pulse energy during a test, suggesting that significant laser absorption was occurring in the plasma. This thus satisfied the second criterion for determining successful LSP ignition.

5.1.2 Wire ignition

As power-threshold experiments were underway, as discussed in [Section 5.2](#), it became apparent that the reliability of spark ignition was unsatisfactory. The inability to consistently arc through the laser beam meant that most ignition attempts would fail, especially below full laser power. Reliability of the spark-ignition system was estimated between 10% and 50% depending on conditions.

Private communications with Todd and Nassar (involved in [\[63, 64\]](#)) highlighted the difficulty of spark ignition, and motivated the change to a solid-target system, with the use of thin metallic wire as an ignition target. As briefly mentioned in [subsection 3.2.4](#), this ignition mechanism creates the necessary electron cloud by thermionic emission from the metal target. Metal is heated to a point where thermal energy in the surface overcomes the surface's work function, releasing electrons. Tungsten had been used successfully in past LSP experiments, such as those of Toyoda *et al.* [\[45\]](#), so 0.01-in-diameter tungsten wire was acquired and placed in the beam path as a target. Approximately 1 in of wire was protruding from the ignition plug, of which only a ~ 0.5 -mm section was exposed to the laser based on the apparent focal point diameter. Estimates suggested that the local wire temperature would increase to 1500–3000 K within 0.1 ms, assuming all laser energy is absorbed (≈ 0.3 J) in the region exposed to the laser. This estimate suggests a full-power laser pulse is sufficient to trigger thermionic emission, which occurs at temperatures beyond 2000 K in tungsten, according to Awan *et al.* [\[71\]](#).

Wire ignition proved to be easier to work with, as laser alignment was simpler. However, it did not guarantee ignition either—wire ignition's greater reliability revealed other important factors in consistently achieving LSP:

- Axial positioning of the laser focus such that it coincides with the target is crucial to generate the “seed” cloud of electrons necessary for LSP ignition.
- Ensuring high argon purity in the chamber was also found to be important. Venting of residual air in the system done by performing several pressurization-vent cycles with argon—at least 3 cycles up to 5 bar—before final pressurization to the test pressure. While this was sufficient for tests at 10 bar and above, additional cycles were found to improve ignition reliability at low pressures (3 bar to 10 bar).

Factors that were hypothesized to impact reliability but ultimately were found to have little to no impact include:

- Focusing the laser on the same spot on a wire across several tests
- Touching/dirtying the wire before installing it in the test section
- Sanding/cleaning the wire before installing it in the test section

Once these reliability factors were identified and controlled, wire ignition proved to be highly reliable, attaining practically 100% reliability. At the time of writing, 124 LSPs were successfully ignited, 80% by wire ignition.

5.1.3 Early LSP observations

These early ignition tests already allowed the observation of LSP. [Figure 5.5](#) depicts the initial growth of LSP ignited off a tungsten wire, showing rapid growth over a fraction of a

millisecond. Under the right ignition conditions, plasma would form practically as soon as the laser was turned on, before the tungsten wire had time to heat up and melt off. This quick ignition would prove to be a useful property when combined with stepped-pulse profiles in later power threshold experiments. In some cases, the wire exhibited signs of localized melting. This observation suggests parts of the wire experienced temperatures beyond tungsten's 3700-K melting point [72], greater than the temperature estimates of 1500–3000 K. This discrepancy is likely due to the laser beam's non-uniform irradiance profile, exposing small portions of wire to greater laser fluxes than the average flux, up to twice as strong at the center of the beam in the case of an idealized gaussian beam.

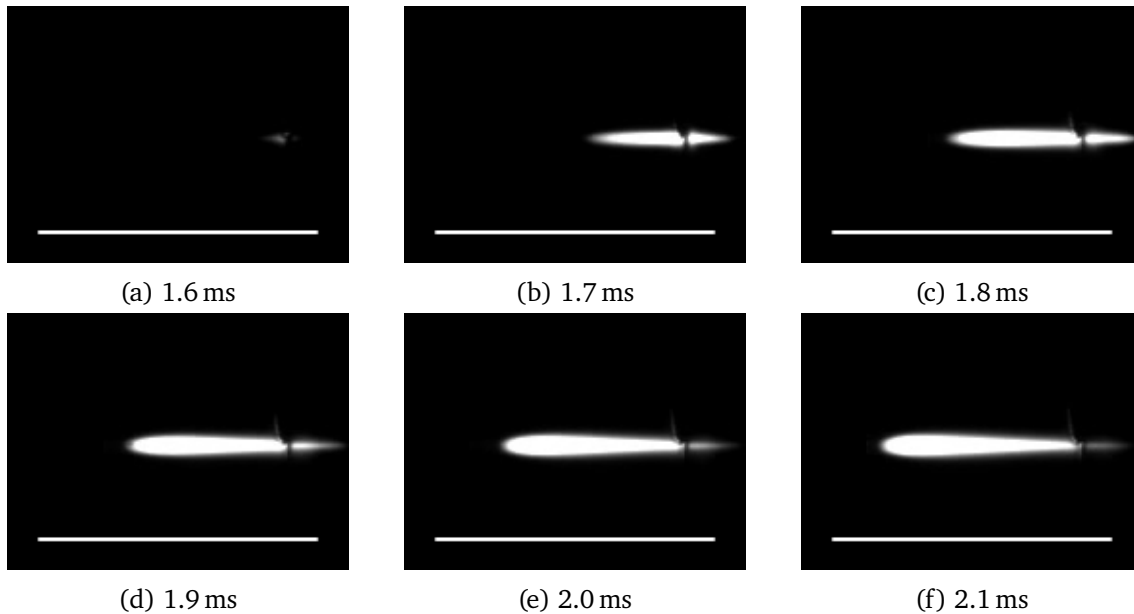


Figure 5.5: LSP ignition via tungsten wire: 3080 W, 20.29 bar. The white line at the bottom of each frame is 10 mm long. LSP1_PS1: 0.1 ms, $f/22$, ND2048

Selected frames of an entire LSP lifetime are shown in Figure 5.6. The initially rapid LSP growth ($\sim 9 \text{ m s}^{-1}$) slows down as it approaches steady conditions, with the front speed decreasing to less than 1 m s^{-1} by the end of the laser pulse. The LSP responded practically instantaneously to the end of the laser pulse, as it dissipated from the high speed footage in the span of 1–2 frames (0.1–0.2 ms).

The fact that the plasma was still growing, albeit slowly, at the end of the laser pulse suggests that true steady-state conditions for the plasma are not yet attained within full-power 10-ms pulses. Unfortunately, the available equipment provided few metrics to quantify the (un)steadiness of flow and plasma conditions within the short time of a laser pulse. Spectroscopy measurements, which could potentially provide a time-dependent measure of plasma temperatures, required a minimum integration time of 3.8 ms, allowing for *at most* three measurements (only one was taken per pulse for this project). Time-dependent laser absorption and pressure measurements would require CW operation. This only left changes in the appearance of the LSP seen in high-speed footage as means to determine steady conditions.

Nevertheless, the rates of change in the size and brightness of the LSP by the end of the pulse are significantly slower than those at plasma ignition. Furthermore, tests using

stepped-pulse profiles discussed in [Section 5.2](#) show a stable plasma appearance after readjusting to a sudden drop in laser power. Although possible, it seems unlikely the plasma conditions would drastically change over a timescale orders of magnitude greater than that of its readjustment, which appears to take place in a few ms.

Attempts were made at operating the experiment in a periodic or quasi-steady state by sending repeated laser pulses after a successful ignition. If a sufficient number of free electrons were still present after the extinction of the LSP, these residual electrons could perhaps allow for a subsequent LSP ignition without the use of an igniter. Tests were performed by sending full-power 10-ms pulses at the laser's maximum duty cycle of 10%, but no re-ignition was observed. The laser's duty cycle created 90 ms gaps in laser irradiation, enough time for the argon to dissipate its heat.

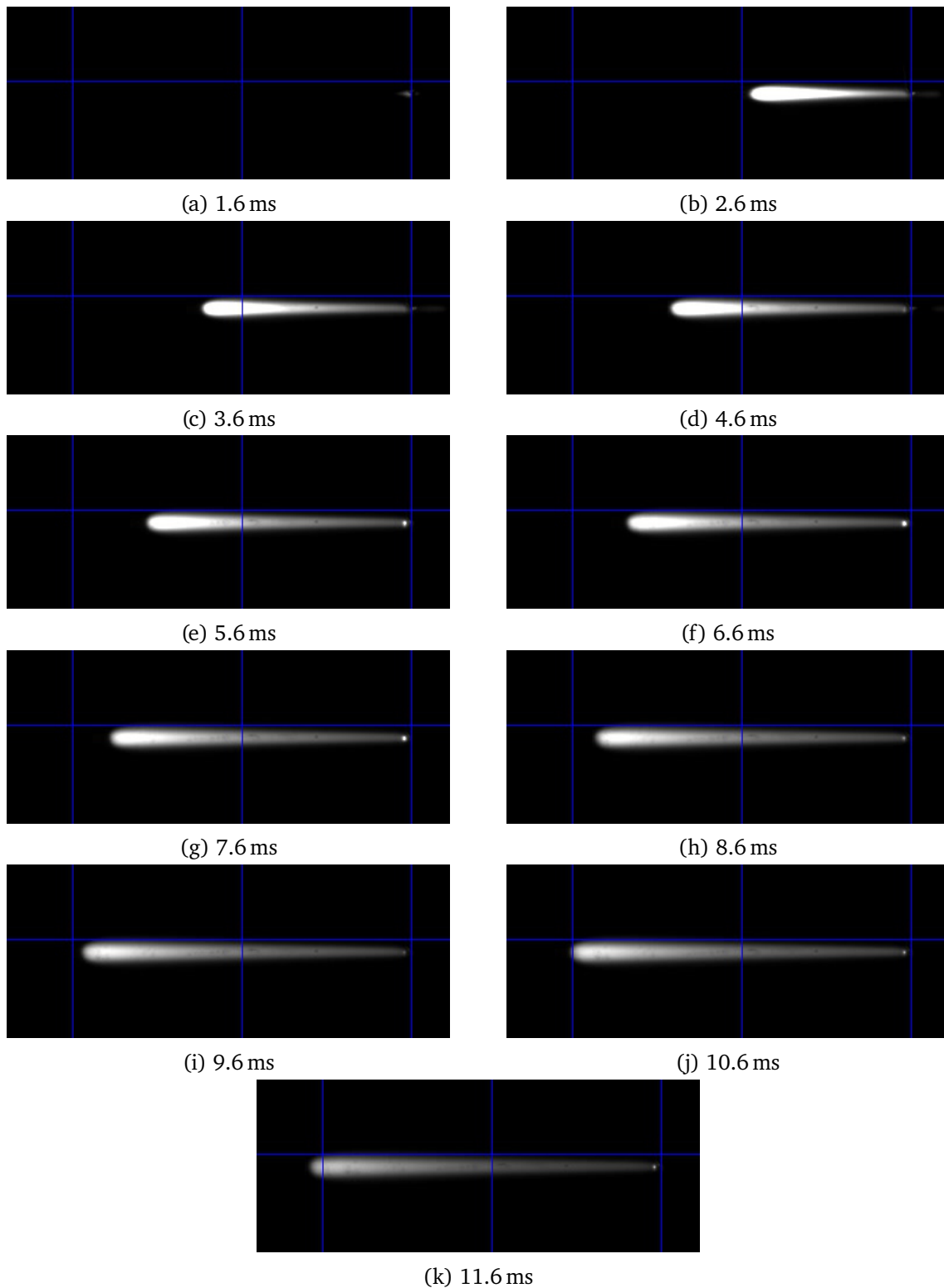


Figure 5.6: LSP growth throughout 10-ms-laser pulse: 3080 W, 20.29 bar. The blue grid is spaced by 10 mm. LSP1_PS1: 0.1 ms, $f/22$, ND2048

5.2 Power threshold

Once LSP ignition had been confirmed, work began on reproducing power threshold experiments, a frequent topic in LSP research. The aim of this experiment is to determine the minimum laser power required to sustain a steady plasma, at a given pressure. Knowing this power threshold is useful to establish the operation bounds of an LSP facility, whether it is a laboratory experiment or a laser-thermal thruster. Several of such experiments have been performed for argon with fiber-lasers: the work of Zimakov *et al.* [30], Matsui *et al.* [44], and Lu *et al.* [46] will thus be used for comparison.

5.2.1 Methodology

The test section would be pressurized with argon to a desired pressure between 3 and 20 bar. Then, determining the power threshold was done through a process akin to a binary search or bisection root-finding algorithm in computer science: LSP would be ignited first at the maximum setpoint power to confirm that the laser and igniter were aligned such that LSP was achievable. Power would then be reduced to a point far below the threshold (10% power) to confirm that LSP was not achieved. This brackets the threshold point. Subsequent tests would be performed at a power setpoint in the middle of this iteratively shrinking bracket, until the threshold was determined to be within approximately 50 W below the last successful LSP test.

This series of tests were performed with both spark and wire ignition. One issue encountered with wire ignition was that while lower laser powers could theoretically sustain LSP, they would not necessarily be sufficient to ignite it. Low laser powers may not raise the temperature of the wire at the ignition point fast enough to trigger thermionic emission, as discussed in subsection 5.1.2, as heat would be conducted away from the laser focal point. No successful ignition was observed below 1 kW of laser power.

To circumvent this issue, stepped laser pulse profiles were used instead of constant laser power. An example of such a pulse is shown in Figure 5.7: the pulse begins at 100% setpoint power for 0.5 ms to initiate the LSP off of the tungsten wire. The power would then be stepped down to the desired power level, which would be maintained for as long as possible to ensure that the LSP could re-adjust to steady conditions.

Whether LSP could be considered steady for a given test was determined by observing its behavior in the high-speed footage. It needed to fulfill two conditions:

1. The LSP is still visible at the end of the laser pulse
2. The LSP is not visibly changing by the time the laser pulse ended, i.e., it is not shrinking or dimming significantly.

As plasma brightness changed with laser power, the variable ND filter would be adjusted to determine whether a vanishing plasma was unstable or simply too dim to be picked up through the lens filters.

5.2.2 Results

The resulting power threshold plot can be seen in Figure 5.8. Both spark and wire ignition experiments are shown, along with data reported by Zimakov *et al.* [30], Matsui *et al.* [44], and Lu *et al.* [46]. The use of wire ignition shows a significant improvement in the

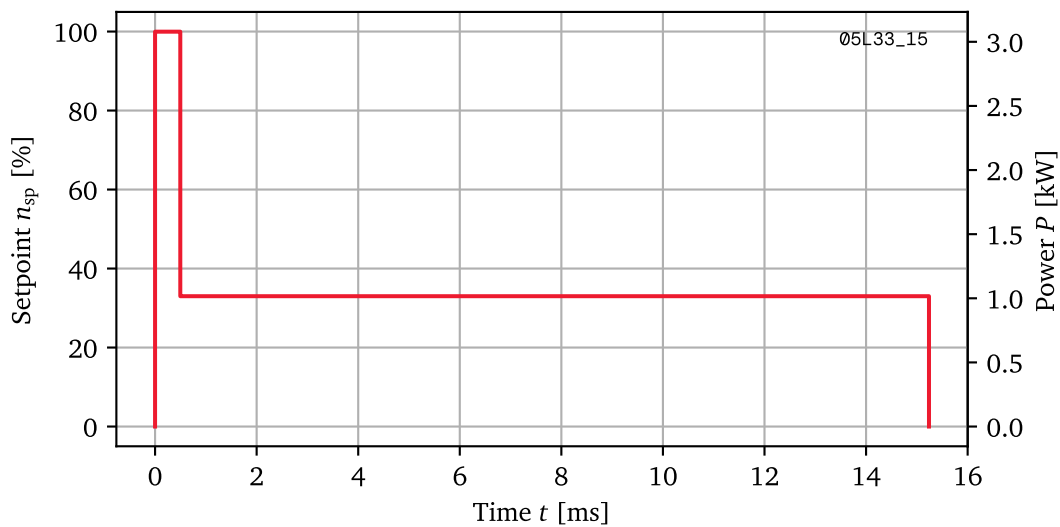


Figure 5.7: Typical stepped-pulse profile: 05L33_15. A complete list of stepped-pulse specifications can be found in [Appendix H](#).

minimum power required to sustain LSP over the spark-ignition method. The improved reliability and ease of alignment afforded by wire ignition enabled sustaining LSP down to hundreds of Watts, whereas spark ignition struggled to ignite and sustain LSP below 1 kW. Note that the uncertainties indicated on the wire ignition data reflect the possible range in which the true power threshold lies and is not related to an uncertainty in the power measurement. Zimakov *et al.* [30] presented a model based on balancing input power with heat conduction (P_h) and radiative losses (P_r) under steady conditions, to evaluate the power threshold as a function of pressure P_t . This expression is reproduced here as [Equation 5.1](#):

$$P_t = P_h + P_r \quad (5.1)$$

Zimakov *et al.*'s experiments had experimentally estimated the parameters of this equation for argon as $p^2 P_h = 26 \text{ bar}^2 \text{ kW}$ and $P_r = 240 \text{ W}$. This same model was fitted to this study's wire-ignited LSP data, yielding the following power threshold parameters: $p^2 P_h = 11 \text{ bar}^2 \text{ kW}$ and $P_r = 178 \text{ W}$. These values can be interpreted, respectively, as the minimum laser power to sustain LSP at 1 bar, and the limiting laser power under which no LSP can be sustained even at high pressures. This relation only holds in the steady case—transient conditions would result in an unbalance of [Equation 5.1](#). For instance, a supplied laser power above the threshold power would deposit more heat in the LSP than it could dissipate by conduction and radiation. This would likely result in the growth of the plasma core to increase the strength of both of its heat dissipation mechanisms.

The experimental data suggests that the threshold power required to sustain plasma beyond 10 bar is lower than the nominal average power of the laser used in this project, i.e., 300 W. This would imply that continuous operation of the LSP generator is possible at pressures of 10 bar and above. Attempts were made to achieve continuous operation at the maximum rated pressure of the test section of 20 bar, but neither spark nor wire ignition was successful. In the case of spark ignition, many of the issues discussed in [subsection 5.1.1](#) may have contributed to a failure to ignite. This could have been mitigated by configuring the

spark igniter for repeated sparks, but this was not attempted. In the case of wire ignition, 300 W is likely not sufficient to locally heat the wire to thermionic-emission temperatures before heat is conducted away from the laser-irradiated point. Stepped-pulse profiles were used to circumvent this issue for power-threshold experiments, but the laser was not capable of emitting a stepped-pulse then transition to CW mode without interrupting emission. Continuous LSP operation could thus not be achieved with the stepped-pulse workaround.

Considering that true steady plasma conditions may not have been attained in some cases, it should be noted that the experimentally determined power threshold may be lower than that of continuous LSP operation. The short pulse duration combined with the high ignition power may allow the LSP to remain stable for the duration of the pulse when it may not have done so over a longer timescale, i.e., over several seconds. Further experiments in CW mode should be performed to provide definite power threshold data.

The discrepancy in the power thresholds achieved across different experiments is due in part to the optical quality of the focused beam, as suggested by Lu *et al.* [46], who have so far achieved the lowest power-threshold results for fiber-laser-sustained argon plasma. As the literature data is all from spark-ignited experiments, direct comparisons to wire-ignition tests may be limited. However, this suggests that a low power threshold can be readily achieved by a basic optical train and a simple wire-ignition system combined with stepped pulse profiles, competing with methodologies that require far greater precision and optical quality.

Qualitative observations were made on the LSP's response to the step-down in laser power. As seen in [Figure 5.9](#), the decrease in input power is immediately apparent, with the plasma shrinking and dimming as soon as the power is dropped. The LSP re-adjusts to new power conditions in less than a millisecond. In this particular case, the LSP remained stable until the end of the laser pulse, 14.8 ms after the step-down in power.

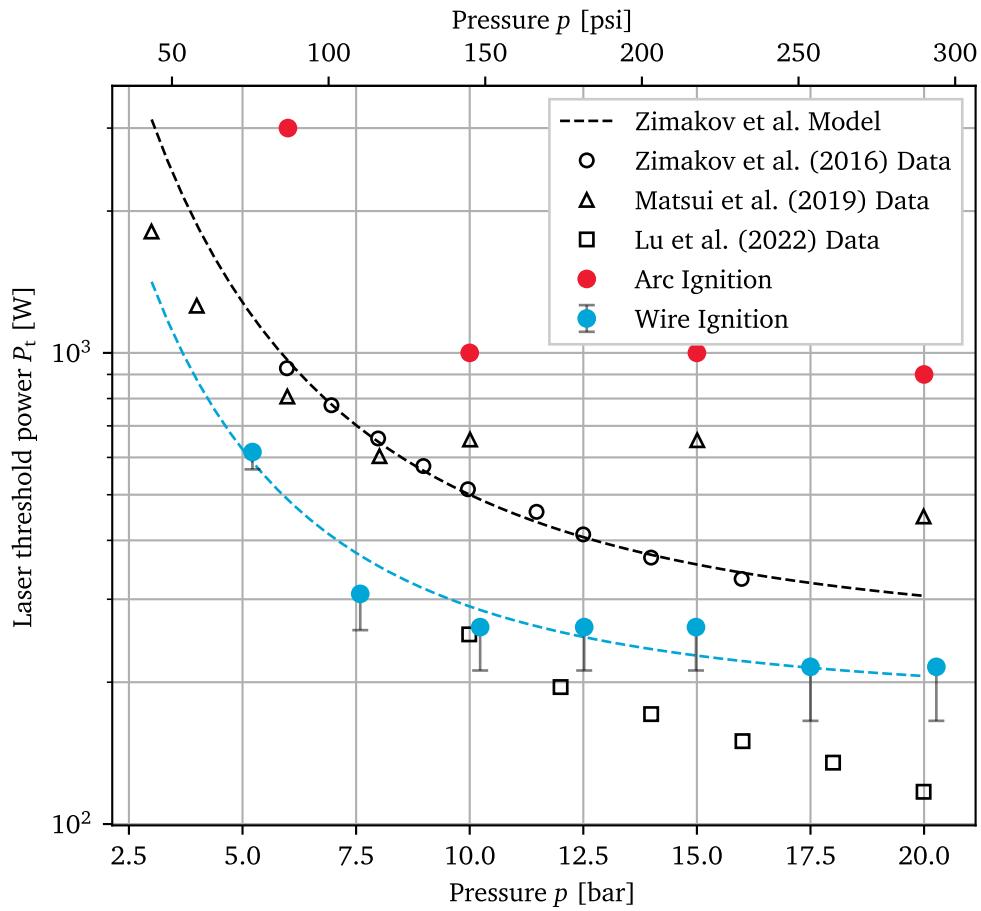


Figure 5.8: Pressure-Power LSP threshold exploration. Zimakov *et al.* [30]’s model is fitted to wire-ignition data as the blue dashed line.

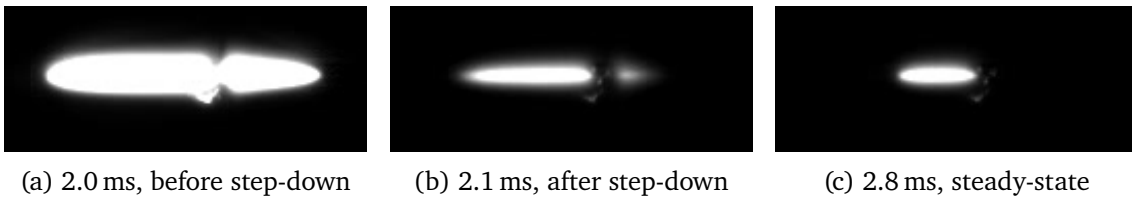


Figure 5.9: LSP adjusting to step-down in power, from 100% to 8.5% (255 W). LSP34_PS28: 0.1 ms, $f/4$, ND2048, pulse profile: 05L8.5_15, pressure: 10.23 bar

5.3 Laser Absorption

Despite the reliability issues of spark ignition, LSP absorption data was successfully acquired at various pressures and laser pulse energies. Incomplete absorption of the incident laser radiation by IB is one of the major sources of inefficient heat deposition, so quantifying this loss is important to control it, reduce it, and eventually optimize an LTP thruster.

5.3.1 Methodology

The Gentec power meter recorded the incident pulse energy for a subset of spark-ignited LSPs. Unfortunately, due to this ignition system's reliability issues, discussed in [Section 5.1](#), a systematic exploration of the variation in absorption due to experimental parameters could not be performed. Nevertheless, some preliminary data was acquired, with some consistency observed at 20 bar of pressure.

Constant-power, 10-ms laser pulses were focused into the test section to ignite LSP. As seen in [Table 3.8](#), a buffer time of 1 ms between the start of the pulse and the spark ignition was used to ensure that the spark was triggered while the laser was on. The laser absorption a by the LSP was defined as follows:

$$a = 1 - \frac{E_{\tau}}{E_{in}} \quad (5.2)$$

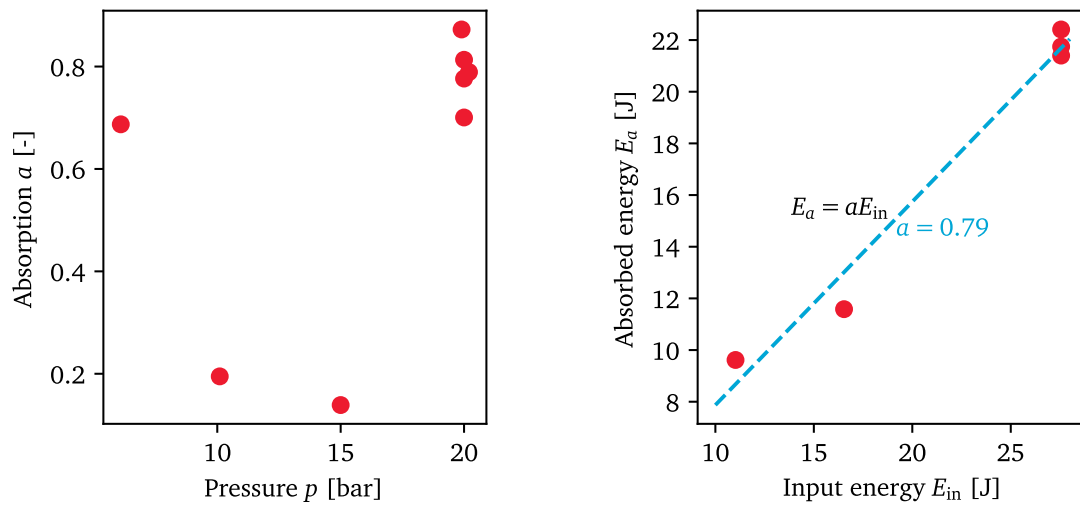
Where E_{τ} is the measured (transmitted) energy reaching the power meter and E_{in} is the pulse energy incident on the LSP. Both variables were determined by correcting both for the losses through the experiment optics (given in [Table 3.7](#)) and the 1-ms buffer time. The laser absorption constitutes one component of the heat deposition efficiency studied in [Section 5.4](#).

5.3.2 Results

Calculated LSP absorption is tabulated in [Table 5.2](#). Although there are a few outliers, overall absorption appears to lie between 70% and 90%. This is visualized in [Figure 5.10a](#). Data for several tests performed at a nominal pressure of 20 bar can be seen in [Figure 5.10b](#), where a linear function was fitted to the data to determine an average absorption factor of 79%.

Table 5.2: LSP energy absorption data. The symbol p is the nominal pressure; E_{pulse} , E_{in} , E_{τ} , and E_a are the laser pulse energy, input energy, transmitted energy, and computed absorption of the LSP, respectively.

Shot ID	p [bar]	E_{pulse} [J]	E_{in} [J]	E_{τ} [J]	a [-]
LSP210_SPX11	20.20	30.80	27.56	5.81	0.79
LSP211_SPX12	20.00	30.80	27.56	6.16	0.78
LSP212_SPX13	20.00	18.48	16.53	4.95	0.70
LSP213_SPX14	19.90	12.32	11.02	1.41	0.87
LSP215_SPX16	20.00	30.80	27.56	5.15	0.81
LSP216_SPX17	6.09	30.80	27.56	8.62	0.69
LSP217_SPX18	10.10	20.54	18.38	14.80	0.19
LSP219_SPX20	15.00	10.16	9.09	7.83	0.14



(a) Absorption across a range of pressure. Variable pulse energy and chamber pressure.

(b) Input energy vs. absorbed energy, calculation of absorption

Figure 5.10: Estimated energy absorption of LSP, 20 bar

Such absorption figures appear to be in agreement with LSP literature stating that most of the laser radiation can be absorbed by the LSP under the right conditions (Keefer [22]). However, much higher absorption was shown to be achievable under some conditions, such as forced convection (Fowler and Smith [32]). For instance, experiments by Toyoda *et al.* [45] show between 80% and 99% absorption depending on the working gas and experimental conditions.

This absorption data can also be paired with LSP footage to approximate the absorption coefficient of the LSP. For instance, Figure 5.11 shows the length measurement of an LSP (10 bar, 3080 W) to be 22 mm at its fullest extent.

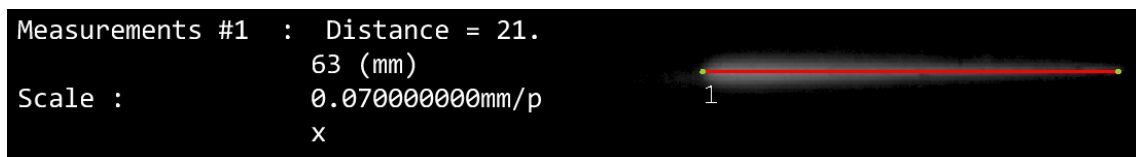


Figure 5.11: Length estimation of LSP. 10.23 bar, 30.8-J pulse. LSP205_SPX6: 0.1 ms, f/11, ND2048

Considering the transmission of radiation through an absorbing medium using the Beer-Lambert law:

$$\frac{I(d)}{I_0} = e^{-\alpha d} \tag{5.3}$$

By considering the energy transmission E_τ/E_{in} to be equivalent to the left-hand side of Equation 5.3, and approximating the path length d as the LSP length, the absorption coefficient can be estimated as follows:

$$\alpha = \frac{\ln(E_\tau/E_{in})}{-d} \tag{5.4}$$

For LSP205_SPX6, this evaluates to 73 m^{-1} . This in fact appears to match the absorption coefficient calculations performed in Chapter 4. Figure 4.3 predicts an absorption coefficient of 67 m^{-1} , while the calculations of Matsui *et al.* [44] predict a value of 58 m^{-1} . While not in perfect agreement with theory, this estimate does appear to provide a value on the same order as predicted by IB absorption models.

As mentioned earlier, the reliability issues of the spark-ignition system prevented the systematic study of LSP absorption characteristics. The α estimate above unfortunately cannot account for the changing absorption/transmission as the LSP grows and assumes a path length based on the final LSP size. Performing absorption measurements under CW regime would improve the measure of α considerably, as measurements could be made once the LSP is fully developed and steady.

5.4 Heat deposition

To fulfill this project's second research objective, i.e., determining LSP heat deposition in the working gas, the change in pressure from initial conditions was monitored with a PCB Piezotronics pressure transducer. As discussed on page 20, this would theoretically allow the estimation of heat deposition without the need to directly track the temperature of the gas, which would have been a major challenge for a millisecond-scale event.

5.4.1 Methodology

The pressure data was collected in parallel with other experiments, all ignited using a wire-ignition method. As seen in Figure 5.1, the pressure transducer was integrated using an instrumentation plug on top of the test section, 1.5 in downstream from the ignition point. The transducer's signal was then processed by a signal conditioner whose output was recorded on an oscilloscope, along with the laser's internal power meter reading. This allowed the synchronization of both the laser's power and the pressure in the test section.

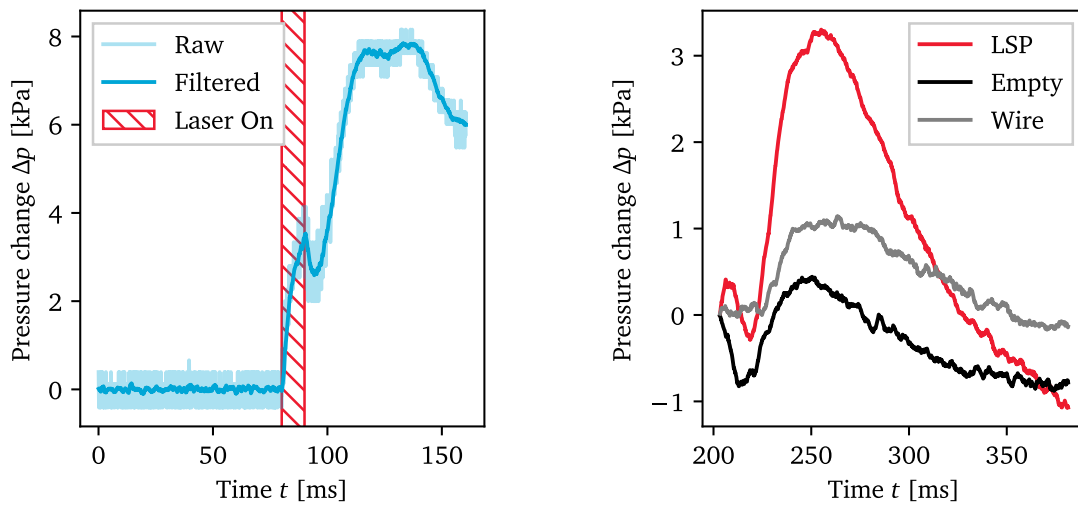
A sample pressure signal is provided in Figure 5.12a. The oscilloscope data featured significant noise, which was filtered out with an infinite impulse response filter to facilitate analysis. Pressure data was acquired for a variety of initial pressures and laser power levels.

To ensure that the resulting pressure rise was primarily caused by the LSP, two tests were performed to rule out the effects of other potential factors:

1. The laser directly incident on the test section walls could heat up the walls which would then heat up the gas
2. The ignition wire heating up could transfer its heat to the surrounding gas.

While either scenario does ultimately heat up the gas, neither mechanism reflects the ideal operation of a laser-thermal thruster, where the plasma itself should be the dominant heat source. To quantify these effects, the following tests were performed at an initial pressure of 10 bar and the resulting pressure rise was recorded:

1. The laser (10 ms, 100%) was pointed into an empty test section, such that the laser would be directly incident on an opaque backplate.
2. A constant 20%, 19.8-ms pulse (equivalent in energy to a 1L20_15 stepped pulse yet insufficient for ignition) was focused on the ignition wire.



(a) Typical pressure change during and after LSP at 3080 W, 20.29 bar

(b) Pressure rise due to alternate heat transfer mechanisms

Figure 5.12: Denoising of pressure data and comparison to other sources of heat

The pressure rise of these tests was then compared to that of a successful LSP at 10 bar, sustained with a 1L20_15 stepped pulse (12.1 J). This is shown in Figure 5.12b. Some measurable effect on pressure is detected from both of these mechanisms, however, the pressure rise from LSP is greater by a factor of three compared to direct heating of the ignition wire. Furthermore, the tests mentioned above represent an absolute worst-case scenario for the magnitude of these heat transfer mechanisms. Absorption measurements discussed in Section 5.3 show that the majority of the laser power is absorbed by the LSP. This leaves less power for heat transfer by wire or chamber wall heating. Heating via the chamber walls in particular is not expected to significantly contribute to overall heat transfer, as the ignition wire would absorb most of any laser power transmitted through the LSP, and direct irradiation had only a minor effect in the first place.

5.4.2 Results

The pressure rise seen in Figure 5.12a exhibits features that were consistently observed at different initial pressures and different laser powers. Namely, the pressure appears to rise continuously while the laser and the LSP is active. As soon as the laser is off and the LSP is extinguished, a small drop in pressure is observed, which is then followed by another, higher rise in pressure. Once the pressure reaches a maximum, usually around 40 ms after the end of the laser pulse, it decreases progressively as the gas loses heat through conduction with the chamber walls. Such a pressure variation is unlikely to be from traveling pressure waves: The speed of sound in argon at 20 °C is 319 mm ms⁻¹, i.e., the test section's length every millisecond, while the observed pressure variation occurs over several hundredths of a second. This suggests that the pressure change observed by the pressure transducer reflects that of the overall test section static pressure.

The continuing pressure rise while the laser (and LSP) is active would suggest that the test-section conditions are in a transient state—the pressure does not stabilize to some level.

This is expected to some degree: 10 ms is unlikely to be enough time for the working gas to reach steady conditions. Furthermore, as these tests are performed in a static mass of argon, the only mechanism to balance this pressure rise is heat transfer out of the test section. This is not expected to occur within that timescale, as the test section would have to heat up significantly to dissipate kW of laser power. In any case, this is not conflicting with the idea that the plasma is approaching/has reached steady conditions. The plasma could certainly reach a state where laser absorption is balanced out by heat dissipation long before the overall test-section conditions have reached steady-state.

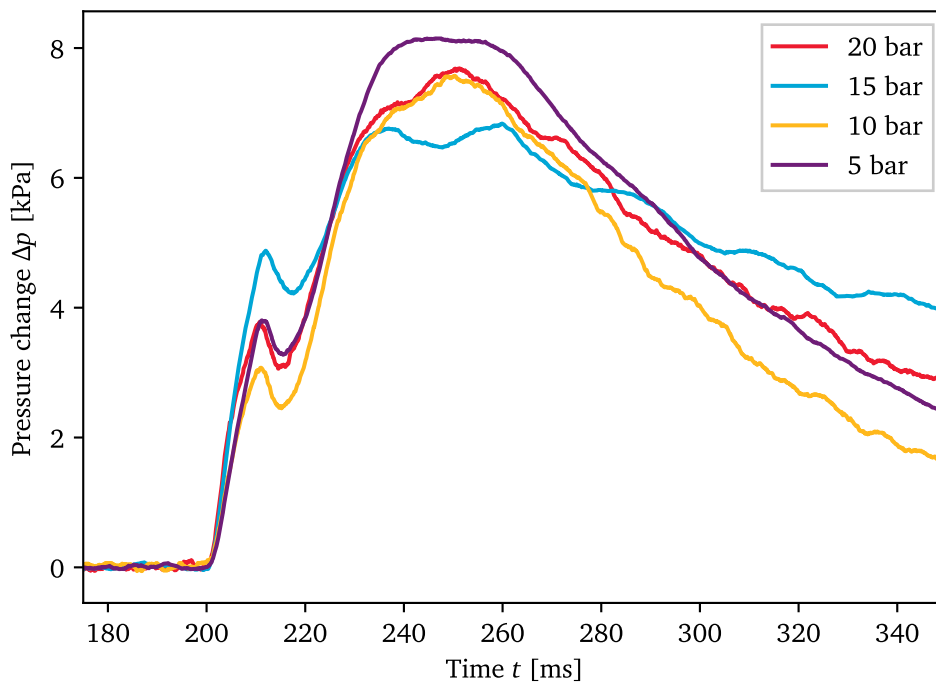


Figure 5.13: Effect of varying initial pressure on pressure rise resulting from LSP

Figure 5.13 shows the pressure variation for a range of initial nominal pressures. As mentioned earlier, the features of this pressure rise remain consistent with a local maximum reached at the end of the laser pulse (10 ms). The magnitude of the pressure change does not appear to be strongly affected by the initial pressure. This consistent pressure profile could be explained as follows: the first rise in pressure appears to be directly linked with the lifetime of the LSP. The growth of the plasma occupies space in the test section at a lower density than the surrounding gas, and the sustained plasma dissipates heat into the test section. Both of these effects contribute to an increase in static pressure, and the change in the gradient of the pressure rise for lower-energy tests seems to support this: the sudden decrease in laser power during a stepped pulse coincides with slower LSP growth (or in some cases, stagnating or decreasing size) and a reduced pressure rise gradient on the pressure plots. This is seen in Figure 5.14. As the laser is turned off, the plasma immediately cools down and shrinks, allowing denser gas to occupy the LSP's volume, reducing the measured static pressure. This decrease is typically less pronounced for lower-energy tests, which would support this hypothesis. The heat remaining in the plasma core as it cools can no longer dissipate as effectively by radiation, and is thus distributed by convection

throughout the test section, resulting in the second pressure rise.

Figure 5.14 shows the effect of reducing the laser pulse energy on the resulting pressure rise. In this case, the peak pressure appears to be correlated with pulse energy, decreasing consistently with decreasing energy. Here again, the change from 20 bar to 10 bar of initial pressure does not appear to have an effect on the resulting heat deposition. The intermediate peak in pressure appears to occur later for lower energy pulses, this is due in part to the longer pulse duration. Another feature of the lower energy pressure rises is a decrease in the rate of change of pressure during the pulse—there is a clear change as the pulse switched from the high setpoint for ignition, to the lower sustained setpoint.

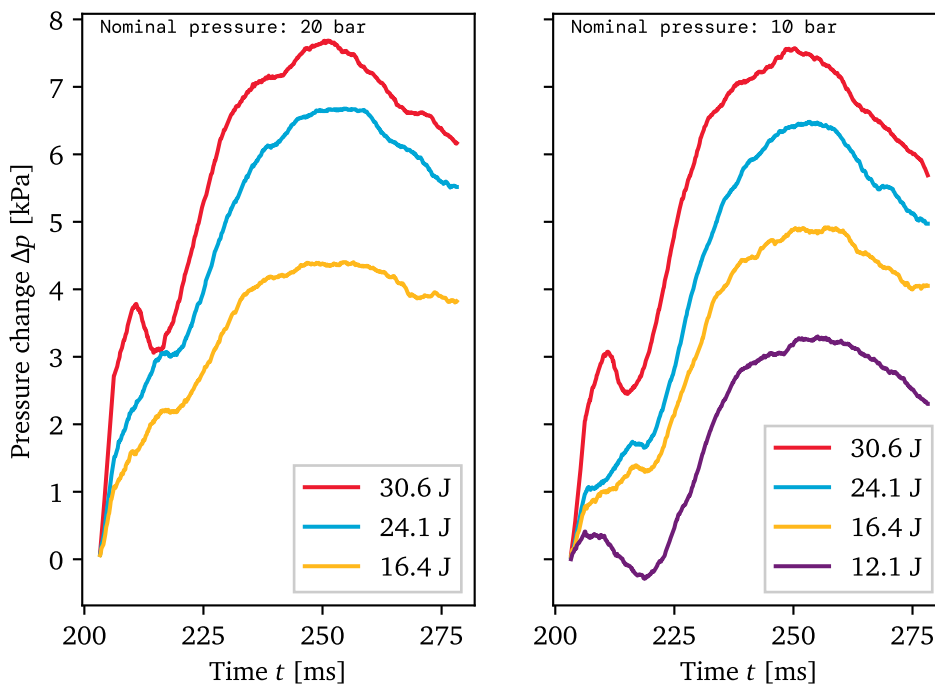


Figure 5.14: Effect of varying laser pulse energy on pressure rise resulting from LSP

A first estimation of the heat deposited in the working gas can be made based on the pressure change, assuming that the observed maximum pressure reflects a state where the heat has been distributed throughout the test section.

$$Q_{\text{in}} = \frac{\Delta p V c_V}{R_g} \quad (5.5)$$

The heat-deposition efficiency η can then be calculated as the ratio $Q_{\text{in}}/E_{\text{in}}$, which captures the overall efficiency of converting the incident laser power on the LSP into heat remaining in the propellant. This would include losses from incomplete laser absorption by the LSP, along with heat lost in the form of radiation, which would heat the chamber walls without really affecting the gas temperature. The detailed results of such a calculation are shown for a single LSP test in Figure 5.15.

Repeating this efficiency calculation for several LSPs sustained at various pressures and pulse energies yields Figure 5.16. Heat-deposition efficiency is seen to be consistent at

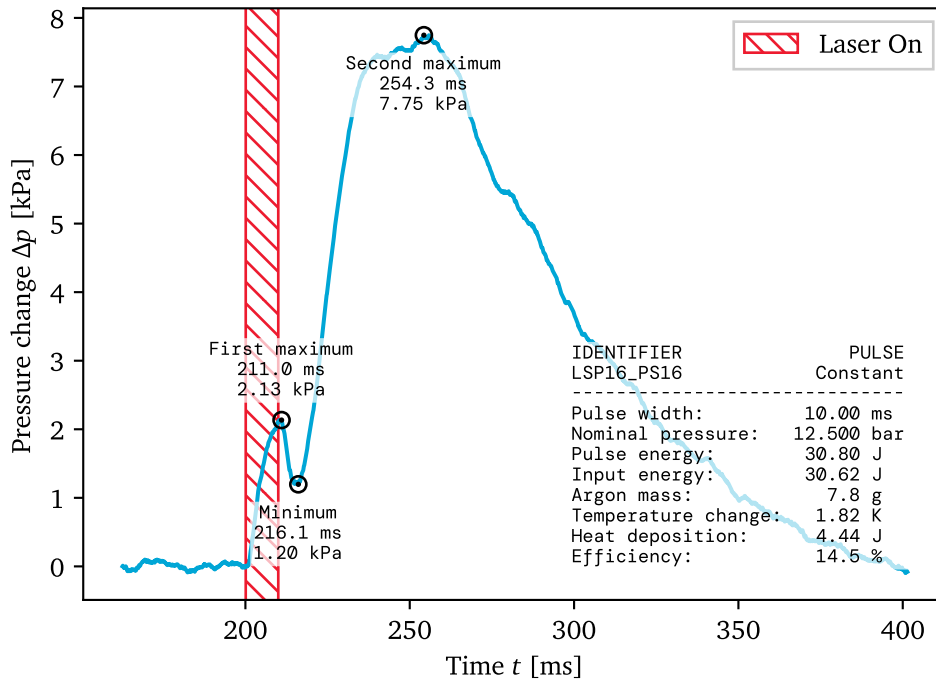


Figure 5.15: Detailed analysis of pressure rise profile, 3080 W, 12.5 bar.

around 15%, regardless of laser power or gas pressure. This apparent independence of heat deposition efficiency could be explained if most of the heat in the LSP is dissipated by radiation. As mentioned in [Chapter 2](#), argon does not have large absorption bands to capture the plasma's emitted radiation, whose continuum spectrum likely lies mostly in the near-UV bands based on Wien's law. Therefore, changing pressures would have little effect on the radiative heat absorption of the cooler surrounding gas and the plasma's radiated heat would be absorbed by the walls.

Other studies have measured heat deposition efficiencies for LSP, usually using CO₂-laser-sustained plasmas. Chen and Mazumder [73] and Mazumder *et al.* [74] have reported heat deposition efficiencies in flowing plasmas ranging from 35–62%. This is significantly greater than the efficiency determined in this study. A possible factor for this discrepancy is the lack of flow in these static experiments. Chen and Mazumder [73] report that greater flow speeds (2–10 m s⁻¹) improve heat deposition efficiencies. As mentioned in [Section 5.3](#), laser absorption by the LSP is one of the major components of the overall heat-deposition efficiency, implying that 20% of the laser energy does not even enter the plasma. Of the 80% that does get absorbed and turned into heat, 81% of it is lost (i.e., 65% of the laser energy), likely by radiation, to the test section walls. This distribution is illustrated in [Figure 5.17](#).

Although useful to estimate heat deposition, the assumption of uniform distribution of heat in the test section does not accurately reflect the actual processes taking place during LSP growth and shortly afterward. This simplifying assumption does not explain the intermediate rise in pressure followed by a short drop immediately after the end of the laser pulse.

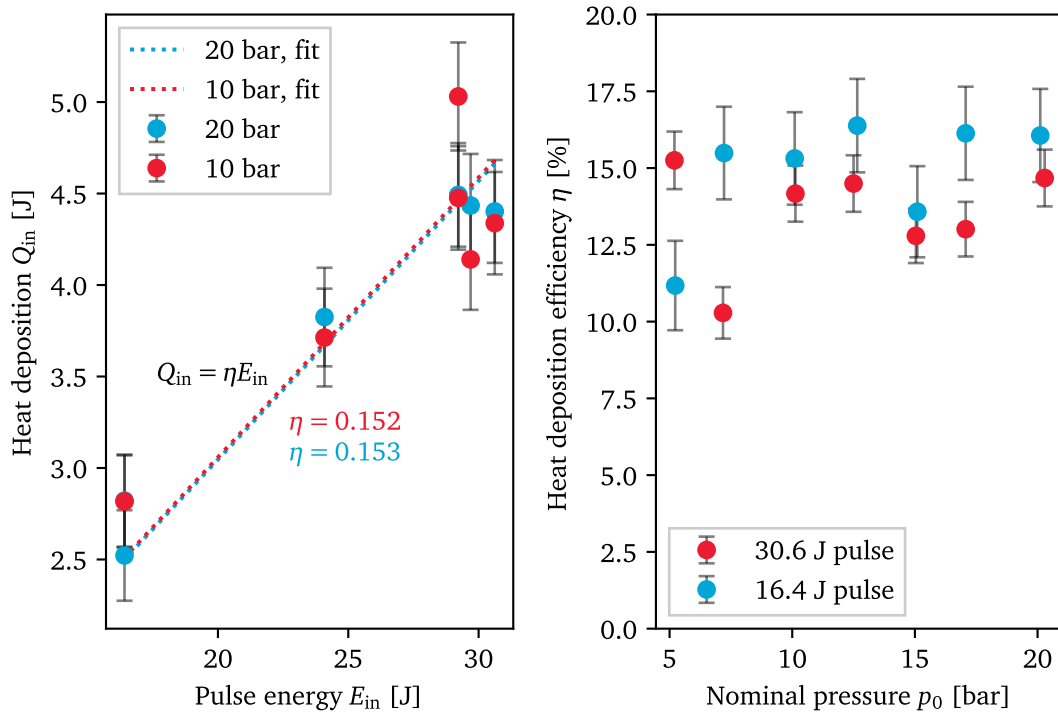


Figure 5.16: Heat-deposition efficiency of LSP. Left: calculation at 20 and 10 bar; right: consistency across a range of pressures, for two different pulse energies

This simple method of determining heat deposition and its efficiency could also be improved on in a few ways. First, replicating these experiments using (a more reliable) spark-ignition system would likely mitigate any heat transfer (although already estimated to be small) occurring via the ignition system. This would also allow the LSP to extend downstream past the ignition point, which may have implications on both laser absorption and overall heat deposition. Second, heat transfer to the walls should be quantified to determine whether this would explain the observed pressure drop after the (global) maximum, and to correct, if deemed necessary, for heat transfer to the walls as the gas is heating up. These changes would likely improve the calculated heat-deposition efficiency.

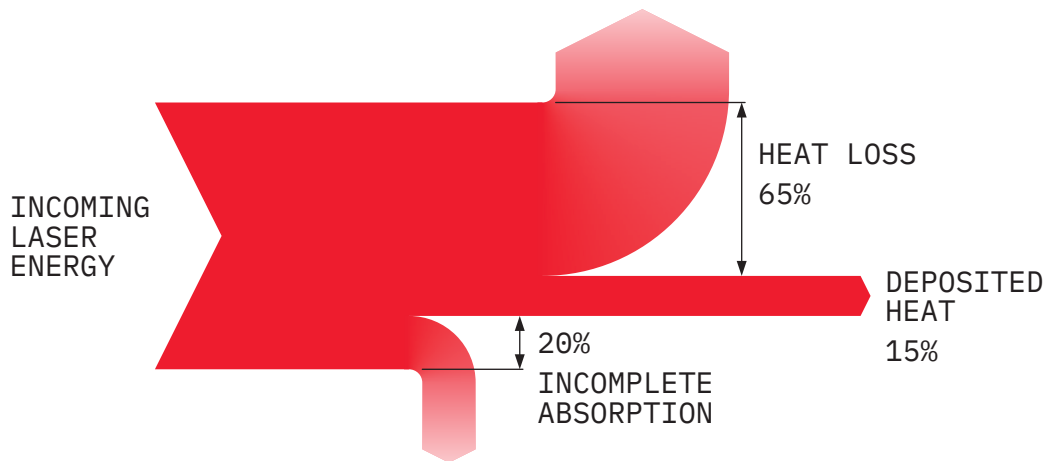


Figure 5.17: Major losses in the overall heat deposition. Diagram to scale.

5.5 Spectroscopic temperature measurement

Spectral data was acquired for several LSP tests, at 20 bar and 10 bar and varying laser power settings. Only one spectral measurement was performed during a test. No collimator was mounted to the fiber termination, allowing the spectrometer to sample a relatively large field of view of the experiment, rather than a single point on the plasma. The sampling area was determined to be approximately 4 cm in diameter at the location of the LSP. This simplified alignment procedures as some part of the LSP's emission was practically guaranteed to be captured by the fiber, and it was assumed that the emitted radiation from the hottest part of the plasma would dominate over that of cooler regions.

Figure 5.18 shows the captured spectral data from an LSP at 20 bar and 3 kW of laser power. Ar I emission lines are clearly visible and closely match the lines tabulated by NIST [47]. Continuum radiation and Ar II emission lines are also seen in the 400–600-nm region, exhibiting the same features seen in spectra captured by Lu *et al.* [46]. However, unlike Lu *et al.*'s data, the captured spectrum shows a drastic difference between the intensity of continuum radiation compared to the Ar I line emissions, almost by an order of magnitude. For instance, the magnitude of the 811-nm line relative to the peak of the continuum radiation (~ 500 nm) in Lu *et al.*'s data is around 5. As seen in Figure 5.18, that ratio is closer to 20 for this project's data. Considering their plasmas were sustained with a 200 W laser, a possible explanation could lie in the difference in laser power magnitude. Not enough spectral data was acquired at comparable power levels to confirm this, however.

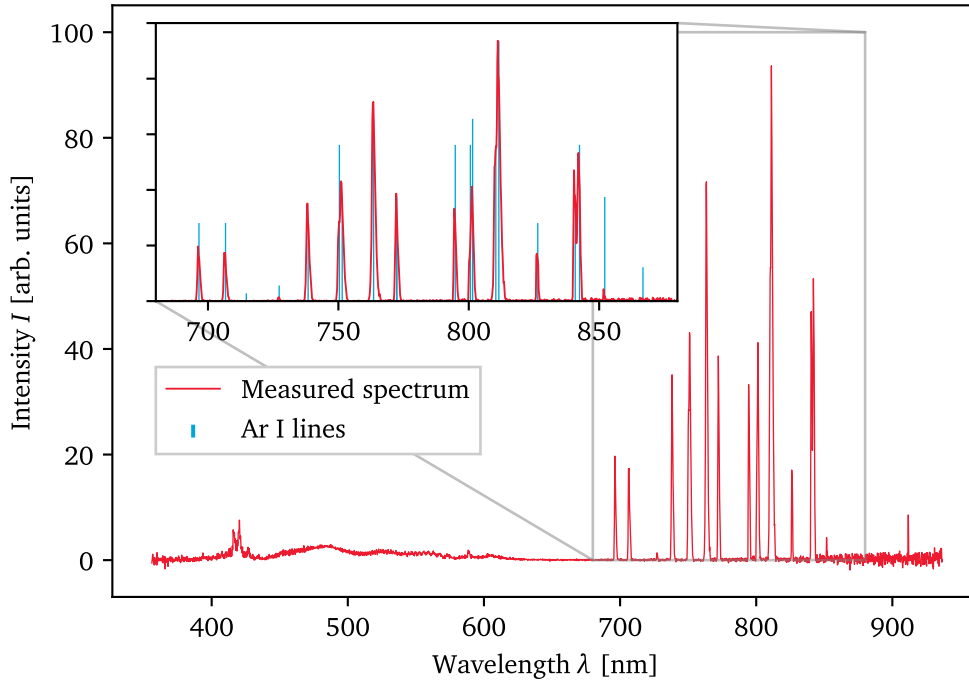


Figure 5.18: Detection of Ar I emission lines in LSP50_X7 in static argon

5.5.1 Boltzmann plot method

Temperature calculation can be performed from spectral data using the Boltzmann plot method, summarized by Ohno *et al.* [75] and discussed in further detail by Griem [76]. The transition of an electron from an upper atomic energy level k to a lower level i generates an emission line at wavelength λ_{ki} with transition probability A_{ki} and degeneracy for level k of g_k . The following equation can be derived to relate these parameters to plasma temperature T :

$$\frac{\epsilon_{ki}\lambda_{ki}}{A_{ki}g_k} = \frac{\hbar cn}{2\mathcal{Z}(T)} \exp\left(-\frac{E_k}{k_B T}\right) \quad (5.6)$$

Where c is the speed of light, n is the atomic number density, $\mathcal{Z}(T)$ is the partition function, and ϵ_{ki} is the spectrally integrated emission line intensity. This equation can be linearized with respect to E_k by taking the natural log of both sides:

$$\ln \frac{\epsilon_{ki}\lambda_{ki}}{A_{ki}g_k} = -\frac{E_k}{k_B T} + \ln \frac{\hbar cn}{2\mathcal{Z}(T)} \quad (5.7)$$

The second term is a constant for a given temperature, so E_k can be plotted against the left-hand side of Equation 5.7, resulting (in theory) in a straight line with gradient $-1/k_B T$. This can then be used to evaluate T . However, as noted by Völker and Gornushkin [77], $\epsilon_{ki}\lambda_{ki}/A_{ki}g_k$ is not dimensionless, and a measure of absolute emission intensity can only be done with appropriate spectrometer calibration, which was not done in this study. There are several methods to resolve these issues, including one that can be used with the relative spectrometry data of this project. This ratio can be normalized by using a reference

transition, denoted with the subscript r . The reference transition functions as a datum and can be arbitrarily selected from the transitions observed in the spectrum, as long as it is consistently used for each data point.

$$\left[\frac{\epsilon_{ki} \lambda_{ki}}{A_{ki} g_k} \right]_r = \frac{\hbar c n_r}{2 \mathcal{Z}_r(T)} \exp \left(-\frac{E_k}{k_B T} \right)_r \quad (5.8)$$

Multiplying either side of the original equation by the reciprocal of the above, then linearizing, yields the following, with the constant term bundled as C :

$$\ln \left(\frac{\epsilon_{ki} \lambda_{ki}}{A_{ki} g_k} \left[\frac{A_{ki} g_k}{\epsilon_{ki} \lambda_{ki}} \right]_r \right) = \frac{-E_k + [E_k]_r}{k_B T} + C \quad (5.9)$$

This normalization enables a temperature to be determined using relative spectral data, as they are all compared to the same reference line in the spectrum. This manipulation has no effect on the gradient of the plot.

5.5.2 Temperature calculation

The acquired spectral data for LSP was processed to extract temperature data using the Boltzmann plot method discussed in the previous section. A subset of emission lines strong enough to be consistently observed for all tests, and well separated from other lines to facilitate identification and spectral integration were selected for this analysis. Relevant properties for these transitions were acquired from the NIST Atomic Spectra Database [47] and are tabulated for the selected lines in Table 5.3. The emission coefficients ϵ_{ki} were computed by fitting a Voigt line profile to the measured spectral lines, and integration was performed on the fitted curve. The 763.51-nm transition was used as the reference line.

Table 5.3: Ar I transitions used to generate Boltzmann plot. The transition wavelength is λ_{ki} , g_k is the degeneracy of the energy level k , A_{ki} the transition probability from level k to i , $\Delta A_{ki}/A_{ki}$ is the relative uncertainty of A_{ki} , and E_k is the energy of level k . Taken from Kramida *et al.* [47].

λ_{ki} [nm]	$g_k A_{ki}$ [s^{-1}]	$\Delta A_{ki}/A_{ki}$ [-]	E_k [eV]
696.54	1.90×10^7	0.07	13.328
706.72	1.90×10^7	0.10	13.302
738.40	4.20×10^7	0.10	13.302
763.51	1.22×10^8	0.10	13.172
794.82	5.58×10^7	0.10	13.283
826.45	4.59×10^7	0.07	13.328

Sample Boltzmann plots generated from LSP with 20.14-bar argon at 3.08 kW are shown in Figure 5.19. It is immediately apparent that the data points are very loosely correlated, providing low confidence in the resulting temperature, which was calculated to be 8000 K and 5000 K. This does not appear possible, as ionization calculations such as the ones done in Section 4.1 suggest argon is not in a plasma state at these temperatures, and that little to no free electrons are available to absorb radiation via inverse bremsstrahlung. Although other absorption mechanisms exist, none appear likely to absorb 1070-nm laser radiation.

Bound-bound electronic energy transitions in Ar I do not feature a 1070-nm band. Absorption lines exist at 1068.3 nm and 1073.4 nm, but they are faint ($g_k A_{ki} \sim 10^5 \text{ s}^{-1}$) [47]. Bound-free transitions (photoionization) would require photons with enough energy to ionize argon. The energy E of a photon can be calculated by Equation 5.10, the Planck–Einstein relation:

$$E = \frac{2\pi\hbar c}{\lambda} \quad (5.10)$$

Evaluating Equation 5.10 for 1070-nm radiation yields 1.16 eV, less than the 15.76-eV ionization energy of Ar I. Only UV and shorter-wavelength radiation carry sufficient energy. Another factor undermining the confidence in these temperature values is their sensitivity to the subset of data used in the calculation: the selection of a different set of transition lines results in major variations in the computed temperature, sometimes suggesting negative absolute temperatures (characterized by a positive slope on the plot). Given these inconsistencies, few conclusive observations can be made from this spectroscopic analysis.

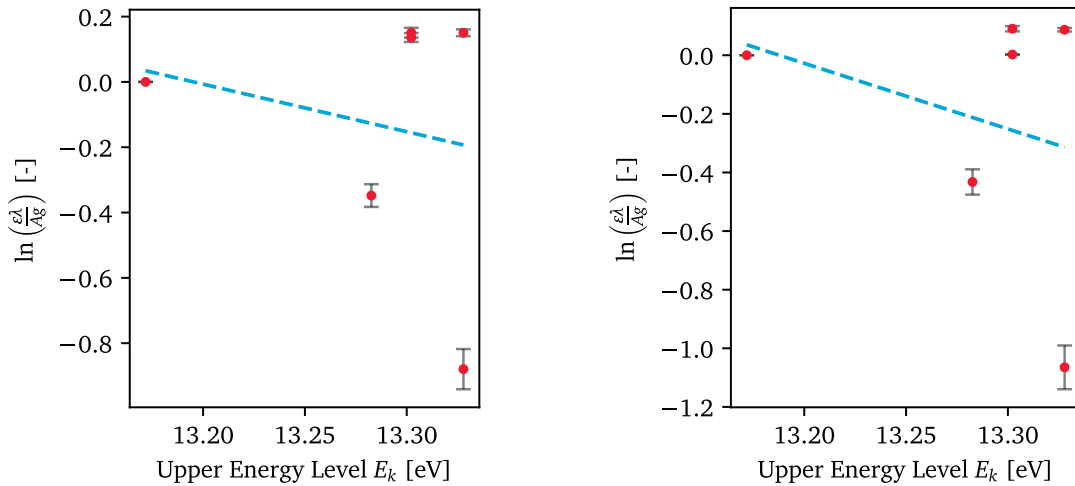
(a) 20 bar, LSP50_X7: $T \approx 8000 \text{ K}$ (b) 10 bar, LSP60_S9: $T \approx 5000 \text{ K}$

Figure 5.19: Boltzmann plots of selected LSP sustained at 3 kW

There may be several reasons for this poor accuracy. The first is that the upper energy levels E_k of most Ar I emission lines are clustered near 13.25 eV, providing a poor sampling range for a linear regression. This is often the case when considering the relative line intensities only for a given atom or ion, as pointed out by Griem [76]: excitation energies are often clustered together. Comparing an Ar I line to an Ar II line would mitigate clustering, but doing so requires knowledge of electron density and a measure of Ar II emission lines. These lines are present in the experimental data, in the range of 400 nm to 500 nm, but are much fainter than the Ar I lines, far more clustered together, and blended into the continuum radiation of the plasma, making detection and integration difficult.

Another possible factor for poor temperature results is that the spectrometer fiber sampled a relatively large area in the test section, and that contrary to the assumption made before this experiment, the emitted radiation of the hottest parts of the LSP do not dominate over colder areas, at least not for the emission lines. Nassar [64] used a collimator to sample the spectrum from specific points in the plasma and had better success in determining temperature.

5.6 Flowing experiments

To inform the design and test of dedicated thruster prototypes, the test section of this study was also designed such that it could be configured for flowing/thruster operation, by replacing the downstream end of the system with a backplate featuring an NPT-threaded port onto which various small nozzles could be inserted. Both the effects of forced flow on LSP properties, and the resulting thrust were of interest. Unlike some of the experiments discussed in [Section 2.3](#), it should be noted no attempt was made at straightening the flow or quantifying its uniformity, as the test section did not provide an easy way to do this. This configuration is illustrated in [Figure 5.20](#). Due to the use of an opaque nozzle module, the power meter could no longer be used for absorption measurements. The facility was fitted on a thrust stand to attempt to measure any changes in the thrust of the apparatus due to the LSP.

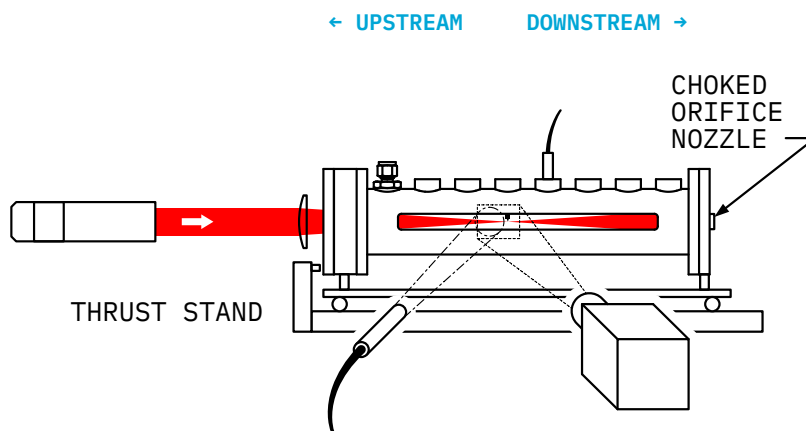


Figure 5.20: Flowing configuration of the test section

Flow rate was controlled by a delivery pressure set by a regulator and choked orifice nozzles of varying diameter, made by drilling out blank NPT plugs. The test section static pressure was set such that choking conditions could be guaranteed, i.e., the ambient pressure was lower than the sonic pressure. This allows the calculation of the mass flow rate using [Equation 4.16](#). Assuming incompressible conditions in the test section, the bulk fluid velocity v_c can be determined from [Equation 4.16](#) and conservation of mass, resulting in [Equation 5.11](#), where D_c is the test section internal diameter (1.5 in).

$$v_c = K_m \frac{D_t^2}{D_c^2} R_g \sqrt{T_0} \quad (5.11)$$

Relatively large nozzle sizes were used to force flow in the test sections at speeds on the same order as the LSP growth speed ($\sim 10 \text{ m s}^{-1}$), to determine the LSP could be modified or blown out by fast enough flows. This is relevant for the thrust chamber design of an LTP thruster, as this could place constraints on the chamber dimensions. Unfortunately, the maximum nozzle diameter was limited to about 4 mm, as this was the feed system's internal diameter. Using larger nozzles would have resulted in choking at the inlet, capping the mass flow rate (and test section flow velocity). The available nozzles under this diameter theoretically provided bulk flow velocities and mass flow rates tabulated in [Table 5.4](#). The

resulting flow speeds in the test section are relatively low and may not reflect those of a dedicated thruster prototype.

Table 5.4: Specifications for choked orifice nozzles used for flowing tests, for 10 bar of test section pressure. The nozzle diameter D , test-section bulk flow velocity v_c , and mass flow rate \dot{m} are given.

D [mm]	v_c [m s^{-1}]	\dot{m} [g s^{-1}]
2.67	0.88	16.5
3.05	1.15	21.5
3.81	1.80	33.6

Figure 5.21 compares the LSP size between the static and flowing case. What is apparent is a noticeably slower growth of the LSP in the upstream direction, suggesting that the forced flow does affect LSP dynamics. The upstream tip of the flowing LSP settles closer to the ignition point than for the static LSP. Forced flow also appears to help the LSP sever the ignition wire, allowing it to extend further past the ignition point, which was not always the case in static conditions. While the overall length of the flowing LSP is longer, it may not be appropriate to compare it to the static case as the wire prevents downstream growth.

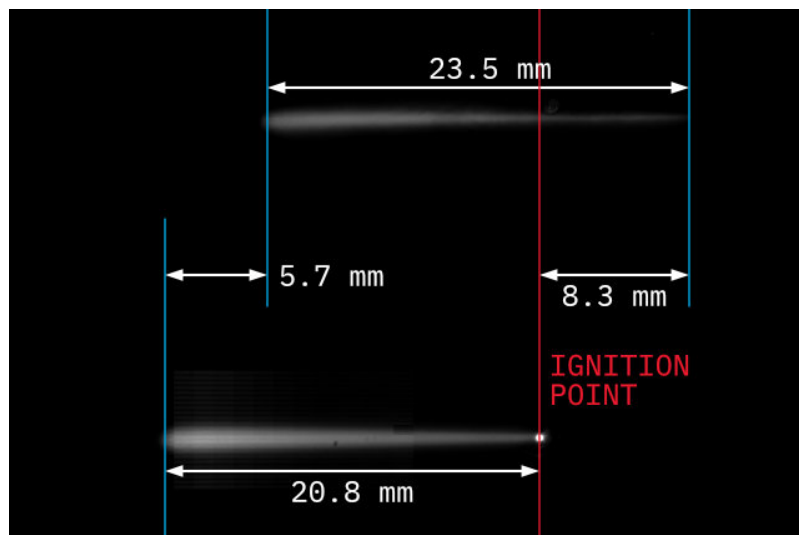
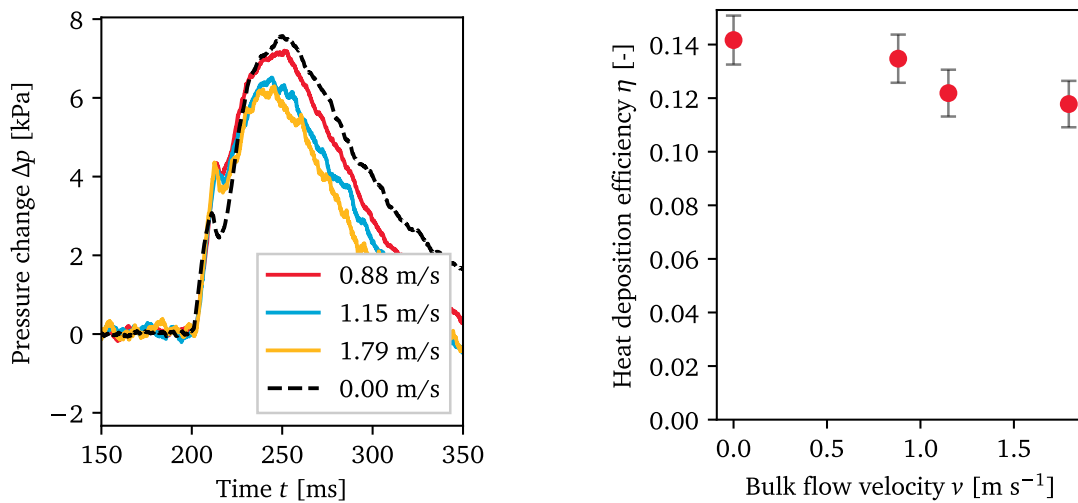


Figure 5.21: Comparison of LSP under forced flow (top) and static LSP (bottom). 10 bar, 3080 W, the bulk flow velocity was 1.8 m s^{-1}

Although bulk flow velocities capable of blowing out the LSP were not attained, LSP stability was observed to be susceptible to flow conditions. As seen in Section 2.3, past LTP facilities such as those of Toyoda *et al.* [45] had features to distribute flow evenly in the test section with little turbulence. This was not the case in this project, as the gas was injected from a single orifice a few inches upstream of the LSP, through the side of the test section rather than co-axially. This likely results in flow with significant, unsteady, rotational and/or radial velocity components by the time it reaches the LSP. Disturbances to the LSP were observed, such as dissipation before the end of the laser pulse, separation of one LSP into two cores, which could sometimes reconnect, and localized variations in plasma brightness during a laser pulse.

Figure 5.22 presents the acquired pressure data for some flowing tests, including heat-deposition efficiency calculations. The pressure profile matches the same pattern observed in static conditions. Although the data suggests a slightly lower heat deposition compared to the static case, the sample size is small, and the flow velocities remain low, almost comparable to static conditions. Definite conclusions based on this limited data may thus be premature. Furthermore, as stated earlier, experiments by Mazumder *et al.* [74] suggest that increased flow rates result in improved heat deposition efficiencies. As their results were obtained at flow rates of 2–10 m s^{-1} , it may be that greater flow rates are necessary to observe a significant and consistent change in heat deposition efficiency. Nevertheless, one noticeable and consistent difference between the static and flowing cases is the intermediate pressure maximum—it appears to be 40% greater than in the static case.

Spectral data was acquired for flowing tests, but exhibited little difference compared to spectra acquired at comparable pressures under static conditions.



(a) Pressure rise

(b) Calculated heat-deposition efficiency

Figure 5.22: Pressure change and heat-deposition efficiency in flowing LSP. 10 bar, 30.6 J input energy.

Chapter 6

Conclusion and further work

Already identified as an alternative to chemical propulsion in the 1970s, laser-thermal propulsion promises the high specific impulse and thrust necessary to unlock rapid transit in the solar system. Whether this promise can be achieved in practice and at scale is however yet to be seen. McGill University's Interstellar Flight Experimental Research Group hopes to revive practical research on LSP for propulsion applications, by attempting to replicate and move beyond the work done in the late 20th century with the fiber-optic lasers considered for use in other directed-energy propulsion concepts such as interstellar lightsails and laser-electric propulsion. By contrast with more recent LSP research which focused on non-propulsion applications, this project aimed to study the thermal, heat deposition, and thrust characteristics of LSP.

A brief review of LTP and LSP literature was provided. DEP and LTP concepts were discussed, including their advantages and drawbacks. Research on LSP was summarized, starting with the physics of inverse bremsstrahlung (i.e., the physical mechanism powering LSP) and moving on the models and observations made through an intense period of research between 1970 and 1990. Researchers at the time were considering the use of CO₂ lasers emitting 10.6 μm radiation, and the implications of a switch to 1.06- μm fiber-optic lasers were mentioned: while the range of these lasers is an order of magnitude greater, the lower IB absorption coefficient at this wavelength mandates higher laser power and/or pressure to sustain LSP. The design of past LSP facilities was briefly reviewed to provide context for the design choices made in creating such a facility at McGill, for the purposes of studying heat deposition and resulting thrust characteristics of argon LSP.

The design process of the LTP thruster laboratory model was then reported in detail. The system's design was driven in large part by the constraints set by the laser available for this experiment, capable of emitting 3-kW pulses, but only for 10 ms. The reasoning behind the decision to retrofit existing apparatus instead of opting for a clean-sheet design was discussed at length: given the many practical uncertainties surrounding the system, and the short timeline available for this project, the retrofit of a perhaps unoptimized test section was deemed preferable to inform the future design of a dedicated thruster model. This came at the cost of hindering thrust experiments, but this tradeoff paid off with the lessons learned in designing and rapidly testing an ignition system, developing diagnostic methodologies, and actually performing LSP experiments.

Some modelling work was performed as part of this thesis, mainly to gain an understanding

6. CONCLUSION AND FURTHER WORK

of the physics involved in inverse bremsstrahlung and the relevant parameters driving laser-sustained plasma. Namely, chamber pressure is a key parameter of any thermal propulsion system, with high pressures providing greater thrust. In LTP, higher pressures are also beneficial to improve LSP absorption properties. Predicting peak absorption (with respect to temperature) is also helpful to estimate the maximum temperature reached in the LSP, as it has been found to be correlated. A simple model for LSP sizing prediction based on deposited laser energy was discussed, yielding temperature and size estimates on the same order as reported in literature and observed in experiment, respectively. The effects of heat deposition in the test section are also modelled, providing the means to estimate the heat deposition efficiency of LSP from experimental measurements. The modelling effort ends with an analysis of the expected performance of an LTP thruster model, suggesting that a dedicated thruster prototype should exhibit significant changes in thrust and exhaust velocity when powered by a laser—as long as the mass-flow rate is lower than 1 g s^{-1} .

Finally, the first results of a series of experiments were reported. Preliminary ignition tests quickly revealed the challenges posed by spark ignition. The use of such a system when constrained by a short laser pulse requires careful design to consistently align the laser focus and the spark. Successful LSP ignition using this system was difficult, but was achieved a few times, enough to build a small dataset on the laser absorption ability of LSP, which was observed to range from 70 to 90%. Initial estimates on the absorption coefficient, derived from the absorption data and high-speed footage, appear to agree with this study's modelling, although a more systematic absorption study would be needed to confirm this. For other experiments, wire ignition was found to be far more reliable than spark ignition and allowed the replication of power threshold studies done in other LSP literature, finding that this ignition system provides a competitively low power threshold without the need of high precision optics. Spectral data acquired during these experiments should theoretically provide a measure of peak plasma temperature, but there appears to be methodology and/or processing issues to be resolved to provide a realistic temperature estimate. Flowing experiments were performed to explore the impact of incoming flow on LSP properties, but the feed system limitations only allowed for a cursory exploration.

The recorded pressure change during and shortly after the LSP provided an insight into the heat deposition into the gas volume by the LSP. This ability will be crucial in a fully realized LTP system: to provide specific impulse on the order of 3000 s yet high thrust, the LSP is meant to heat the surrounding propellant, and not be exhausted by itself (which would result in higher specific impulse but only for low thrust). The experimental data suggests a low heat-deposition efficiency of around 15%, relative to the laser power incident on the LSP. Combined with the measured absorption, this builds an overall picture of the major loss factors involved in LSP: incomplete laser absorption and heat radiated to the walls or outside the test section appear to be responsible for 20% and 65% of the energy losses, respectively. This provides a baseline on efficiency that can now be improved on with a variety of strategies suggested in the LTP literature. The peculiar shape of the pressure profile, with its local maximum and minimum, should be the subject of further study.

The objectives set for this project, to build an argon LTP thruster model, may not have been entirely met. Issues encountered with the unoptimized test section and its impact on thrust measurement meant that meaningful thrust experiments could not be performed. However, a method to determine heat deposition into the working gas was developed based on the pressure change of the test section, providing a baseline on heat-deposition efficiency, which can be used to design the next iteration of an LTP thruster at McGill University. In

this regard, the project is successful in initiating a new experimental research effort on LTP at the IFERG, and the questions and issues raised across various aspects of this project could motivate several new, more targeted studies.

6.1 Further work

As this thesis project's *raison d'être* was to lay the groundwork for experimental research on LSP and LTP at McGill, there are many opportunities for further work. A selection of such opportunities is given below.

Optimization of the test section Although the retrofit of the cavitation experiment's test section enabled rapid experimentation, its non-optimal design posed several challenges, some of which were already discussed in [subsection 3.2.1](#). The test section mass was particularly problematic for thrust experiments. Further research on LSP and LTP will be limited without the development of a new LSP generator or prototype thruster optimized for this project. Such optimizations would include:

- Opting for a lighter material for the pressure vessel, likely aluminum, to minimize weight
- Reducing the overall length and diameter of the vessel. This would both provide more flexibility in terms of beam geometry, allowing the use of shorter lenses or placing the laser focus at different locations in the chamber, to potentially optimize the LSP location relative to the nozzle. Smaller dimensions would also reduce the overall weight and result in a greater measured change in temperature and pressure, as implied by [Equation 5.5](#).
- Smaller observation windows. Although the current side windows offer excellent visibility throughout the length of the test section, their slender geometry and length mandated the use of heavy steel mounting clamps. Opting for lighter, smaller round windows bolted directly into the pressure vessel's body may be sufficient.

Such improvements would greatly facilitate the development of an appropriate thrust stand and provide greater beam-shaping flexibility without compromising on laser absorption measurements.

Improved spark-ignition system As discussed in [Section 5.1](#), the original spark-igniter design for this study proved difficult to work with, as the large spark gap and side-by-side electrodes created inconsistent arc paths that would rarely intersect with the laser beam path. Although good results were obtained with wire ignition, spark ignition is still thought to be optimal for future experiments, as its advantages over wire ignition would be worth the additional development efforts. As a reminder, they are as follows:

- An uninterrupted laser beam path allows determining the absorbed laser power and the absorption coefficient. It also does not impede the downstream growth of the LSP.
- Sparks can be generated at will without consuming material between each test. Several experiments could potentially be done in quick succession without re-aligning optics or replacing the ignition wire.

In order to improve spark consistency and ignition reliability, several improvements could be made to both the spark-plug design and how it integrates in the test section:

- The electrodes should be in a co-axial configuration, as was done for several LSP experiments in the literature (Zimakov *et al.* [30], Matsui *et al.* [44], and Lu *et al.* [46]). This may improve the consistency of the arc path and would enable precise mechanical control of electrode distance more easily than with side-by-side electrodes.
- To accommodate for such an electrode arrangement, the test section should be modified with instrumentation ports along the opposite wall of the cylinder. Each port should ideally be precisely matched with another port facing it.
- Electrode tip distance should be reduced down to about a millimeter to favor arcing even at 20 bar and to constraint possible arc paths to those intersecting with the laser focus. Ideally, this gap should be adjustable in order to adapt the electrode distance based on the test pressure.
- Discussions with researchers experienced with spark igniters suggested that a sharp tipped electrode paired with a rounded electrode gave better results.

Specific impulse measurement One of the ultimate goals of the LTP project at McGill University is to demonstrate the feasibility of the concept and show that a specific impulse of 1000 s to 3000 s is possible under the right conditions. While the roadmap to this sort of performance is long and would involve a switch to hydrogen as a working gas, the experiment should be set-up such that mass-flow rates can be controlled and/or measured, enabling the calculation of exhaust velocity when combined with thrust data. This can be done using a mass flowmeter or by controlling mass flow by operating the facility in a double-choked configuration (choked at inlet and exhaust nozzle).

Absorption measurements in flowing conditions The nozzles used in this study could be easily fabricated and swapped on the test section but made it impossible to acquire an accurate measure of the laser power transmitted through the LSP and out of the test section, as the orifice size was significantly smaller than the laser beam. Designing a nozzle module that allows such a measurement would permit the study of the effect of flow on laser absorption. Poor laser absorption is one of the main efficiency loss mechanisms for an LTP thruster, so being able to measure it in flowing conditions would be valuable. This can be done either by using a regular laser window mount with an off-axis nozzle, or by designing an annular nozzle around the laser window (whether this option is worth the considerable design effort is debatable).

Additional spectrometry and thermal imaging As discussed in [Section 5.5](#), there is much room to improve this experiment's spectroscopy methodologies. The spectrometer's fiber termination should be equipped with a collimator to sample precise points in the LSP, which should improve the spectral data for temperature estimation with the Boltzmann plot method. Once this is corrected, the collimator could be mounted on opto-mechanical stages to precisely position it relative to the LSP, enabling the construction of temperature maps of the LSP, which could be compared to axisymmetric numerical models currently in development at McGill (Bao and Higgins [78]). In addition to spectroscopy, infrared thermal imaging could potentially be used to study the change in temperature of the cooler surrounding gas, providing additional data on the effective heat deposition from the LSP.

References

- [1] E. Tiesinga, P. J. Mohr, D. B. Newell, and B. N. Taylor. “Fundamental Physical Constants from NIST,”
The NIST Reference on Constants, Units, and Uncertainty. (May 2019), [Online]. Available: <https://physics.nist.gov/cuu/Constants/index.html>.
- [2] L3Harris. “RL10 Engine,” L3Harris® Fast. Forward. (Jul. 28, 2023), [Online]. Available: <https://www.l3harris.com/all-capabilities/rl10-engine> (visited on 2023-07-28).
- [3] R. E. Bilstein, “Fire, Smoke, and Thunder: The Engines,”
in *Stages to Saturn: A Technological History of the Apollo/Saturn Launch Vehicles*, ser. NASA History Series,
Washington, DC: National Aeronautics and Space Administration, 1996.
[Online]. Available: <https://history.nasa.gov/SP-4206/ch5.htm>.
- [4] T. Berger *et al.*, “Long term variations of galactic cosmic radiation on board the International Space Station, on the Moon and on the surface of Mars,”
Journal of Space Weather and Space Climate, vol. 10, p. 34, 2020, ISSN: 2115-7251.
DOI: [10.1051/swsc/2020028](https://doi.org/10.1051/swsc/2020028). [Online]. Available: <https://www.swsc-journal.org/articles/swsc/abs/2020/01/swsc200013/swsc200013.html> (visited on 2021-06-19).
- [5] A. Kantrowitz, “The Relevance of Space,”
Bulletin of the Atomic Scientists, vol. 27, no. 4, pp. 32–33, Apr. 1, 1971,
ISSN: 0096-3402. DOI: [10.1080/00963402.1971.11455353](https://doi.org/10.1080/00963402.1971.11455353). [Online]. Available: <https://doi.org/10.1080/00963402.1971.11455353>.
- [6] D. L. Nored, “Application of high power lasers to space power and propulsion,”
in *2d NASA Conf. on Laser Energy Conversion*,
National Aeronautics and Space Administration, Jan. 1, 1976.
[Online]. Available: <https://ntrs.nasa.gov/citations/19760014427>.
- [7] P. Lubin, “A Roadmap to Interstellar Flight,”
Journal of the British Interplanetary Society, vol. 69, no. 2, pp. 40–72, Feb. 2016.
DOI: [10.48550/arXiv.1604.01356](https://doi.org/10.48550/arXiv.1604.01356). [Online]. Available: <http://arxiv.org/abs/1604.01356>.
- [8] L3Harris. “RS-25 Engine,” L3Harris® Fast. Forward. (Jul. 28, 2023), [Online]. Available: <https://www.l3harris.com/all-capabilities/rs-25-engine> (visited on 2023-07-28).
- [9] A. G. Belluscio. “SpaceX advances drive for Mars rocket via Raptor power,”
NASASpaceFlight.com. (Mar. 7, 2014),

REFERENCES

- [Online]. Available: <https://www.nasaspaceflight.com/2014/03/spacex-advances-drive-mars-rocket-raptor-power/>.
- [10] Aerojet Rocketdyne, *NEXT-C NASA Evolutionary Xenon Thruster-Commercial*, Jan. 2022. [Online]. Available: https://www.rocket.com/sites/default/files/documents/NEXT-C_Data_sheet_01_2022_FINAL_DIGITAL.pdf.
- [11] G. Woodcock, "Evaluation of Solar Thermal Propulsion for In-Space Propulsion Application," in *39th AIAA/ASME/SAE/ASEE Joint Propulsion Conference and Exhibit*, American Institute of Aeronautics and Astronautics, Jul. 2003. DOI: 10.2514/6.2003-5029. [Online]. Available: <https://arc.aiaa.org/doi/abs/10.2514/6.2003-5029>.
- [12] E. Duplay, Z. F. Bao, S. Rodriguez Rosero, A. Sinha, and A. Higgins, "Design of a rapid transit to Mars mission using laser-thermal propulsion," *Acta Astronautica*, vol. 192, pp. 143–156, Mar. 1, 2022, ISSN: 0094-5765. DOI: 10.1016/j.actaastro.2021.11.032. [Online]. Available: <https://www.sciencedirect.com/science/article/pii/S0094576521006305>.
- [13] J. Shoji and V. Larson, "Performance and heat transfer characteristics of the laser-heated rocket - A future space transportation system," in *12th International Electric Propulsion Conference*, ser. International Electric Propulsion Conference, American Institute of Aeronautics and Astronautics, Nov. 14, 1976. DOI: 10.2514/6.1976-1044. [Online]. Available: <https://arc.aiaa.org/doi/10.2514/6.1976-1044>.
- [14] D. R. Koenig, "Experience Gained from the Space Nuclear Rocket Program (Rover)," Los Alamos National Laboratory, LA-10062-H, May 1986. [Online]. Available: <http://nuke.fas.org/space/la-10062.pdf>.
- [15] Ad Astra. "Technology," Ad Astra Rocket Company. (2013), [Online]. Available: <https://web.archive.org/web/20130522003114/http://www.adastrarocket.com/aarc/Technology>.
- [16] E. Duplay, "Review of Laser-Thermal Propulsion Literature," Delft University of Technology, Delft, Literature Review, Dec. 13, 2022. [Online]. Available: <http://resolver.tudelft.nl/uuid:14d92747-9882-492e-b013-8ef197a5a578>.
- [17] Gemini Observatory. "The Sites," Gemini Observatory. (Apr. 3, 2020), [Online]. Available: <https://www.gemini.edu/observing/telescopes-and-sites/sites#0.9-2.7um>.
- [18] H.-A. Eckel and W. Schall, "Laser Propulsion Systems," in *Advanced Propulsion Systems and Technologies, Today to 2020*, American Institute of Aeronautics and Astronautics, 2008, pp. 357–406, ISBN: 978-1-56347-929-8. DOI: 10.2514/5.9781600866937.0357.0406. [Online]. Available: <https://arc.aiaa.org/doi/abs/10.2514/5.9781600866937.0357.0406>.
- [19] W. Hettel *et al.*, "Beam propagation simulation of phased laser arrays with atmospheric perturbations," *Applied Optics*, vol. 60, no. 17, pp. 5117–5123, Jun. 10, 2021, ISSN: 2155-3165.

REFERENCES

- DOI: [10.1364/AO.422337](https://doi.org/10.1364/AO.422337). [Online]. Available: <https://www.osapublishing.org/ao/abstract.cfm?uri=ao-60-17-5117>.
- [20] L. N. Myrabo, “Power-Beaming Technology for Laser Propulsion,” in *Orbit-Raising and Maneuvering Propulsion: Research Status and Needs*, New York: American Institute of Aeronautics and Astronautics, Jan. 1, 1984, ISBN: 978-0-915928-82-8 978-1-60086-563-3. DOI: [10.2514/4.865633](https://doi.org/10.2514/4.865633). [Online]. Available: <https://arc.aiaa.org/doi/book/10.2514/4.865633>.
- [21] J. T. Kare, “Laser-powered heat exchanger rocket for ground-to-orbit launch,” *Journal of Propulsion and Power*, vol. 11, no. 3, pp. 535–543, May 1995, ISSN: 0748-4658, 1533-3876. DOI: [10.2514/3.23875](https://doi.org/10.2514/3.23875). [Online]. Available: <https://arc.aiaa.org/doi/10.2514/3.23875>.
- [22] D. Keefer, “Laser-Sustained Plasmas,” in *Laser Induced Plasmas and Applications*, New York: Marcel Dekker Inc., 1989, ISBN: 0-8247-8078-7.
- [23] B. T. C. Zandbergen, *AE4-S01 Thermal Rocket Propulsion*, 2.08. TU Delft, Aug. 20, 2020.
- [24] A. Kascak, “Nozzle and Cavity Wall Cooling Limitations on Specific Impulse of a Gas-Core Nuclear Rocket,” in *Joint Conference on Sensing of Environmental Pollutants*, American Institute of Aeronautics and Astronautics, 1971. DOI: [10.2514/6.1971-1527](https://doi.org/10.2514/6.1971-1527). [Online]. Available: <https://arc.aiaa.org/doi/abs/10.2514/6.1971-1527> (visited on 2021-03-10).
- [25] R. J. Glumb and H. Krier, “Concepts and status of laser-supported rocket propulsion,” *Journal of Spacecraft and Rockets*, vol. 21, no. 1, pp. 70–79, Jan. 1, 1984, ISSN: 0022-4650. DOI: [10.2514/3.8610](https://doi.org/10.2514/3.8610). [Online]. Available: <https://arc.aiaa.org/doi/10.2514/3.8610>.
- [26] A. Campargue, S. Kassi, K. Pachucki, and J. Komasa, “The absorption spectrum of H₂: CRDS measurements of the (2-0) band, review of the literature data and accurate ab initio line list up to 35 000 cm⁻¹,” *Physical Chemistry Chemical Physics*, vol. 14, no. 2, pp. 802–815, Dec. 8, 2011, ISSN: 1463-9084. DOI: [10.1039/C1CP22912E](https://doi.org/10.1039/C1CP22912E). [Online]. Available: <https://pubs.rsc.org/en/content/articlelanding/2012/cp/c1cp22912e> (visited on 2023-12-05).
- [27] T. W. Johnston and J. M. Dawson, “Correct values for high-frequency power absorption by inverse bremsstrahlung in plasmas,” *The Physics of Fluids*, vol. 16, no. 5, pp. 722–722, May 1, 1973, ISSN: 0031-9171. DOI: [10.1063/1.1694419](https://doi.org/10.1063/1.1694419). [Online]. Available: <https://pubs.aip.org/pfl/article/16/5/722/823978/Correct-values-for-high-frequency-power-absorption> (visited on 2023-08-01).
- [28] Y. P. Raizer, “Subsonic Propagation of a Light Spark and Threshold Conditions for Maintenance of a Plasma by Radiation,” *Soviet Physics Journal of Experimental and Theoretical Physics*, vol. 31, no. 6, Dec. 1970. [Online]. Available: <https://www.osti.gov/biblio/4116864>.
- [29] N. A. Generalov, V. P. Zimakov, G. I. Kozlov, V. A. Masyukov, and Yu. P. Raizer, “Continuous optical discharge,” *Soviet Journal of Experimental and Theoretical Physics Letters*, vol. 11, pp. 302–304, 1970.

REFERENCES

- [30] V. P. Zimakov, V. A. Kuznetsov, N. G. Solovyov, A. N. Shemyakin, A. O. Shilov, and M. Yu. Yakimov, "Interaction of near-IR laser radiation with plasma of a continuous optical discharge," *Plasma Physics Reports*, vol. 42, no. 1, pp. 68–73, Jan. 2016, ISSN: 1063-780X, 1562-6938. DOI: [10.1134/S1063780X15110100](https://doi.org/10.1134/S1063780X15110100). [Online]. Available: <http://link.springer.com/10.1134/S1063780X15110100> (visited on 2023-01-06).
- [31] R. Welle, D. Keefer, and C. Peters, "Energy conversion efficiency in high-flow laser-sustained argon plasmas," in *AIAA/ASME 4th Fluid Mechanics, Plasma Dynamics and Lasers Conference*, Atlanta, May 1986. [Online]. Available: <https://ui.adsabs.harvard.edu/abs/1986aiaa.confT...K>.
- [32] M. C. Fowler and D. C. Smith, "Ignition and maintenance of subsonic plasma waves in atmospheric pressure air by cw CO2 laser radiation and their effect on laser beam propagation," *Journal of Applied Physics*, vol. 46, no. 1, pp. 138–150, Jan. 1975, ISSN: 0021-8979. DOI: [10.1063/1.322197](https://doi.org/10.1063/1.322197). [Online]. Available: <https://aip.scitation.org/doi/10.1063/1.322197>.
- [33] S.-M. Jeng and D. Keefer, "Numerical study of laser-sustained hydrogen plasmas in a forced convective flow," in *22nd Joint Propulsion Conference*, ser. Joint Propulsion Conferences, American Institute of Aeronautics and Astronautics, Jun. 16, 1986. DOI: [10.2514/6.1986-1524](https://doi.org/10.2514/6.1986-1524).
- [34] J. H. Batteh and D. R. Keefer, "Two Dimensional Generalization of Raizer's Analysis for the Subsonic Propagation of Laser Sparks," *IEEE Transactions on Plasma Science*, vol. 2, no. 3, pp. 122–129, Sep. 1, 1974. DOI: [10.1109/TPS.1974.4316825](https://doi.org/10.1109/TPS.1974.4316825). [Online]. Available: <https://www.osti.gov/biblio/4232630>.
- [35] C. D. Moody, "Maintenance of a gas breakdown in argon using 10.6- μ cw radiation," *Journal of Applied Physics*, vol. 46, no. 6, pp. 2475–2482, Jun. 1975, ISSN: 0021-8979, 1089-7550. DOI: [10.1063/1.322232](https://doi.org/10.1063/1.322232). [Online]. Available: <http://aip.scitation.org/doi/10.1063/1.322232>.
- [36] H. Krier, J. Mazumder, T. Rockstroh, T. Bender, and R. Glumb, "Continuous wave laser gas heating by sustained plasmas in flowing argon," *AIAA Journal*, vol. 24, no. 10, pp. 1656–1662, Oct. 1986, ISSN: 0001-1452. DOI: [10.2514/3.9497](https://doi.org/10.2514/3.9497). [Online]. Available: <https://arc.aiaa.org/doi/10.2514/3.9497>.
- [37] M. V. Gerasimenko, G. I. Kozlov, and V. A. Kuznetsov, "Laser plasmatron," *Soviet Journal of Quantum Electronics*, vol. 13, no. 4, p. 438, Apr. 30, 1983, ISSN: 0049-1748. DOI: [10.1070/QE1983v013n04ABEH004189](https://doi.org/10.1070/QE1983v013n04ABEH004189). [Online]. Available: <https://iopscience-iop-org.tudelft.idm.oclc.org/article/10.1070/QE1983v013n04ABEH004189/meta>.
- [38] H. Krier, J. Mazumder, D. K. Zerkle, A. Mertogul, and S. Schwartz, "Energy Conversion Measurements in Laser-Sustained Argon Plasmas for Application to Rocket Propulsion," Department of Mechanical and Industrial Engineering University of Illinois at Urbana-Champaign, Technical Report UIIU-ENG-88-4006, Apr. 15, 1988, p. 85. [Online]. Available: <https://apps.dtic.mil/sti/citations/ADA194931>.

REFERENCES

- [39] J. Black, H. Krier, and R. J. Glumb, "Laser Propulsion 10-kW Thruster Test Program results," *Journal of Propulsion and Power*, vol. 11, no. 6, pp. 1307–1316, Nov. 1995, ISSN: 0748-4658, 1533-3876. DOI: [10.2514/3.23973](https://doi.org/10.2514/3.23973). [Online]. Available: <https://arc.aiaa.org/doi/10.2514/3.23973>.
- [40] S. Schwartz *et al.*, "Laser-sustained gas plasmas for application to rocket propulsion," in *25th Joint Propulsion Conference*, Monterey, CA, U.S.A.: American Institute of Aeronautics and Astronautics, Jul. 12, 1989. DOI: [10.2514/6.1989-2631](https://doi.org/10.2514/6.1989-2631). [Online]. Available: <https://arc.aiaa.org/doi/10.2514/6.1989-2631>.
- [41] D. Keefer, R. Welle, and C. Peters, "Power absorption in laser-sustained argon plasmas," *AIAA Journal*, vol. 24, no. 10, pp. 1663–1669, Oct. 1986, ISSN: 0001-1452. DOI: [10.2514/3.9498](https://doi.org/10.2514/3.9498). [Online]. Available: <https://arc.aiaa.org/doi/10.2514/3.9498>.
- [42] T. Inoue *et al.*, "Oscillation phenomenon of laser-sustained plasma in a CW laser propulsion," *Vacuum*, The 4th International Symposium on Applied Plasma Science, vol. 73, no. 3, pp. 433–438, Apr. 19, 2004, ISSN: 0042-207X. DOI: [10.1016/j.vacuum.2003.12.063](https://doi.org/10.1016/j.vacuum.2003.12.063). [Online]. Available: <https://www.sciencedirect.com/science/article/pii/S0042207X03002926>.
- [43] M. Matsui, S. Yoneda, K. Komurasaki, Y. Yamagiwa, and Y. Arakawa, "Atomic-Oxygen-Flow Generation by Laser-Driven Plasma Wind Tunnel as Low-Earth-Orbit-Environment Simulator," *AIAA Journal*, vol. 52, no. 8, pp. 1806–1810, Aug. 2014, ISSN: 0001-1452, 1533-385X. DOI: [10.2514/1.J052991](https://doi.org/10.2514/1.J052991). [Online]. Available: <https://arc.aiaa.org/doi/10.2514/1.J052991> (visited on 2022-12-08).
- [44] M. Matsui, T. Ono, T. Kamei, and K. Mori, "Generating conditions of argon laser-sustained plasma by disk, fiber and diode lasers," *Vacuum*, vol. 167, pp. 490–494, Sep. 1, 2019, ISSN: 0042-207X. DOI: [10.1016/j.vacuum.2018.05.012](https://doi.org/10.1016/j.vacuum.2018.05.012). [Online]. Available: <https://www.sciencedirect.com/science/article/pii/S0042207X18301751>.
- [45] K. Toyoda, K. Komurasaki, and Y. Arakawa, "Thrust performance of a CW laser thruster in vacuum," *Vacuum*, 3rd International Symposium on Applied Plasma Science (ISAPS 01), vol. 65, no. 3, pp. 383–388, May 27, 2002, ISSN: 0042-207X. DOI: [10.1016/S0042-207X\(01\)00446-8](https://doi.org/10.1016/S0042-207X(01)00446-8). [Online]. Available: <https://www.sciencedirect.com/science/article/pii/S0042207X01004468>.
- [46] Q. Lu *et al.*, "Characteristic Diagnostics of a Laser-Stabilized High-Pressure Argon Plasma by Optical Emission Spectroscopy," *IEEE Transactions on Plasma Science*, vol. 50, no. 9, pp. 2578–2587, Sep. 2022, ISSN: 1939-9375. DOI: [10.1109/TPS.2022.3172977](https://doi.org/10.1109/TPS.2022.3172977).
- [47] A. Kramida, Yu. Ralchenko, J. Reader, and NIST ASD Team, *NIST Atomic Spectra Database*, version 5.10. Gaithersburg, MD: National Institute of Standards and Technology, 2022. [Online]. Available: <https://physics.nist.gov/asd> (visited on 2023-10-05).
- [48] T. F. Sheerin, E. Petro, K. Winters, P. Lozano, and P. Lubin, "Fast Solar System transportation with electric propulsion powered by directed energy," *Acta Astronautica*, vol. 179, pp. 78–87, Feb. 1, 2021, ISSN: 0094-5765. DOI: [10.1016/j.actaastro.2020.09.016](https://doi.org/10.1016/j.actaastro.2020.09.016). [Online]. Available: <https://www.sciencedirect.com/science/article/pii/S0094576520305567>.

REFERENCES

- [49] Thorlabs. “N-BK7 Plano-Convex Lenses (AR Coating: 1050 - 1700 nm) -> Damage Thresholds,” Thorlabs, Inc. - Your Source for Fiber Optics, Laser Diodes, Optical Instrumentation and Polarization Measurement & Control. (), [Online]. Available: https://www.thorlabs.com/newgrouppage9.cfm?objectgroup_id=3281 (visited on 2023-08-06).
- [50] Ocean Optics,
USB4000 Fiber Optic Spectrometer Installation and Operation Manual, 2008.
[Online]. Available:
<https://www.oceaninsight.com/globalassets/catalog-blocks-and-images/manuals--instruction-ocean-optics/spectrometer/usb4000operatinginstructions.pdf>.
- [51] R. Nave. “Diffraction grating resolution,” HyperPhysics Concepts. (2000), [Online]. Available: <http://hyperphysics.phy-astr.gsu.edu/hbase/phyopt/gratres.html#c4> (visited on 2023-12-06).
- [52] J. C. Kokkalis, “Onset of Cavitation in a Dynamically Loaded Piston-Cylinder,” M.Sc. Thesis, McGill University, Montreal, Jul. 2023.
- [53] Brookhaven National Laboratory,
Guide for Glass and Plastic Window Design for Pressure Vessels, Dec. 2005.
- [54] Thorlabs. “WG12012-C - Ø2” N-BK7 Broadband Precision Window, AR Coated: 1050 - 1700 nm, t = 12 mm,” Thorlabs, Inc. - Your Source for Fiber Optics, Laser Diodes, Optical Instrumentation and Polarization Measurement & Control. (), [Online]. Available:
<https://www.thorlabs.com/thorproduct.cfm?partnumber=WG12012-C>.
- [55] GS Plastic Optics. “Transmission Curves of Optics Materials,” GS Plastic Optics. (), [Online]. Available: <https://www.gsoptics.com/transmission-curves/>.
- [56] Shalom EO. “JGS1,”
Shalom EO- Laser Components, IR optics, Scintillators, Crystals wafers. (), [Online]. Available:
<https://shalomeo.com/jgs1-datasheet-shalomeo.html>.
- [57] AEM Performance Electronics,
Instruction Manual 30-2853 HIGH OUTPUT IGBT COIL.
[Online]. Available: https://www.aemelectronics.com/sites/default/files/aem_product_instructions/30-2853%20High%20Output%20Inductive%20Smart%20Coil.pdf.
- [58] M. A. Lieberman and A. J. Lichtenberg,
Principles of Plasma Discharges and Materials Processing, 1st ed. Wiley, Apr. 8, 2005, ISBN: 978-0-471-72001-0 978-0-471-72425-4.
DOI: [10.1002/0471724254](https://doi.org/10.1002/0471724254). [Online]. Available:
<https://onlinelibrary.wiley.com/doi/book/10.1002/0471724254>.
- [59] J. G. Theis, G. R. Werner, T. G. Jenkins, and J. R. Cary, “Computing the Paschen curve for argon with speed-limited particle-in-cell simulation,”
Physics of Plasmas, vol. 28, no. 6, p. 063 513, Jun. 1, 2021,
ISSN: 1070-664X, 1089-7674. DOI: [10.1063/5.0051095](https://doi.org/10.1063/5.0051095). [Online]. Available:
<https://pubs.aip.org/pop/article/28/6/063513/974018/Computing-the-Paschen-curve-for-argon-with-speed> (visited on 2023-09-04).
- [60] A.-J. Takken,
“Development of a high-temperature Solar Thermal Propulsion engine,”
M.S. thesis, Delft University of Technology, Delft, 2021. [Online]. Available:

REFERENCES

- <https://repository.tudelft.nl/islandora/object/uuid%3Ae6cc6c72-bcfb-4927-a0bf-d935a6ba32f8>.
- [61] E. H. W. Jansen, "Improvement and validation of test stand performance for novel micropropulsion systems," M.S. thesis, Delft University of Technology, Delft, 2016. [Online]. Available: <https://repository.tudelft.nl/islandora/object/uuid%3A28f0b7fa-1288-4e32-88fd-2e138745714a>.
- [62] H. Greenhouse, R. Lowry, and B. Romenesko, *Hermeticity of Electronic Packages*, 2nd ed. Oxford, Waltham, Mass.: Elsevier ; William Andrew, 2012, ISBN: 978-1-4377-7878-6.
- [63] R. Akarapu, A. R. Nassar, S. M. Copley, and J. A. Todd, "Numerical model of a laser-sustained argon plasma," *Journal of Laser Applications*, vol. 21, no. 4, pp. 169–175, Nov. 2009, ISSN: 1042-346X. DOI: [10.2351/1.3263120](https://doi.org/10.2351/1.3263120). [Online]. Available: <https://lia.scitation.org/doi/10.2351/1.3263120> (visited on 2023-04-17).
- [64] A. R. Nassar, "Investigation of laser-sustained plasma and the role of plasma in carbon dioxide laser nitriding of titanium," Ph.D. dissertation, Pennsylvania State University, Oct. 3, 2012. [Online]. Available: <https://etda.libraries.psu.edu/catalog/16162> (visited on 2023-04-14).
- [65] M. N. Saha and A. Fowler, "On a physical theory of stellar spectra," *Proceedings of the Royal Society of London. Series A, Containing Papers of a Mathematical and Physical Character*, vol. 99, no. 697, pp. 135–153, Jan. 1997. DOI: [10.1098/rspa.1921.0029](https://doi.org/10.1098/rspa.1921.0029). [Online]. Available: <https://doi.org/10.1098/rspa.1921.0029> (visited on 2023-10-16).
- [66] S. G. Lias, "Ionization Energy Evaluation," in *NIST Chemistry WebBook, NIST Standard Reference Database Number 69*, P. J. Linstrom and W. G. Mallard, Eds., Gaithersburg, MD: National Institute of Standards and Technology, 2023. [Online]. Available: <https://doi.org/10.18434/T4D303>.
- [67] A. S. Richardson, "2019 NRL Plasma Formulary," US Naval Research Laboratory, Washington, DC, Technical Report, Handbook, Sep. 20, 2019. [Online]. Available: <https://apps.dtic.mil/sti/citations/AD1116543> (visited on 2023-04-17).
- [68] S. Gordon and B. J. McBride, "Computer program for calculation of complex chemical equilibrium compositions and applications. Part 1: Analysis," NASA Reference Publication NASA-RP-1311, Oct. 1, 1994. [Online]. Available: <https://ntrs.nasa.gov/citations/19950013764> (visited on 2023-12-14).
- [69] V. Pozzobon, W. Levasseur, K.-V. Do, B. Palpant, and P. Perré, "Household aluminum foil matte and bright side reflectivity measurements: Application to a photobioreactor light concentrator design," *Biotechnology Reports*, vol. 25, e00399, Mar. 1, 2020, ISSN: 2215-017X. DOI: [10.1016/j.btre.2019.e00399](https://doi.org/10.1016/j.btre.2019.e00399). [Online]. Available: <https://www.sciencedirect.com/science/article/pii/S2215017X1930373X> (visited on 2023-12-13).
- [70] E. W. Lemmon, I. H. Bell, M. L. Huber, and M. O. McLinden, "Thermophysical Properties of Fluid Systems,"

REFERENCES

- in *NIST Chemistry WebBook, NIST Standard Reference Database Number 69*, P. J. Linstrom and W. G. Mallard, Eds., Gaithersburg, MD: National Institute of Standards and Technology, 2023. [Online]. Available: <https://doi.org/10.18434/T4D303>.
- [71] T. I. Awan, A. Bashir, A. Tehseen, and S. Bibi, “Chapter 7 - Electrons in nanostructures,” in *Chemistry of Nanomaterials*, T. I. Awan, A. Bashir, and A. Tehseen, Eds., Elsevier, Jan. 1, 2020, pp. 179–206, ISBN: 978-0-12-818908-5. DOI: [10.1016/B978-0-12-818908-5.00007-X](https://doi.org/10.1016/B978-0-12-818908-5.00007-X). [Online]. Available: <https://www.sciencedirect.com/science/article/pii/B978012818908500007X> (visited on 2023-12-06).
- [72] Royal Society of Chemistry. “Tungsten - Element information, properties and uses | Periodic Table,” Periodic Table - Royal Society of Chemistry. (2023), [Online]. Available: <https://www-rsc-org.tudelft.idm.oclc.org/periodic-table/element/74/tungsten>.
- [73] X. Chen and J. Mazumder, “Emission spectroscopy of cw CO₂ laser-sustained argon plasma: Effects of gas-flow speed,” *Journal of Applied Physics*, vol. 66, no. 12, pp. 5756–5762, Dec. 15, 1989, ISSN: 0021-8979, 1089-7550. DOI: [10.1063/1.343644](https://doi.org/10.1063/1.343644). [Online]. Available: <https://pubs.aip.org/jap/article/66/12/5756/17184/Emission-spectroscopy-of-cw-CO2-laser-sustained> (visited on 2023-12-16).
- [74] J. Mazumder, T. J. Rockstroh, and H. Krier, “Spectroscopic studies of plasma during cw laser gas heating in flowing argon,” *Journal of Applied Physics*, vol. 62, no. 12, pp. 4712–4718, Dec. 15, 1987, ISSN: 0021-8979, 1089-7550. DOI: [10.1063/1.339022](https://doi.org/10.1063/1.339022). [Online]. Available: <https://pubs.aip.org/jap/article/62/12/4712/173881/Spectroscopic-studies-of-plasma-during-cw-laser> (visited on 2023-12-16).
- [75] N. Ohno, M. A. Razzak, H. Ukai, S. Takamura, and Y. Uesugi, “Validity of Electron Temperature Measurement by Using Boltzmann Plot Method in Radio Frequency Inductive Discharge in the Atmospheric Pressure Range,” *Plasma and Fusion Research*, vol. 1, pp. 028–028, 2006. DOI: [10.1585/pfr.1.028](https://doi.org/10.1585/pfr.1.028).
- [76] H. R. Griem, “Spectroscopic temperature measurements,” in *Principles of Plasma Spectroscopy*, ser. Cambridge Monographs on Plasma Physics, Cambridge: Cambridge University Press, 1997, pp. 279–299, ISBN: 978-0-521-61941-7. DOI: [10.1017/CB09780511524578.012](https://doi.org/10.1017/CB09780511524578.012). [Online]. Available: <https://www.cambridge.org/core/books/principles-of-plasma-spectroscopy/spectroscopic-temperature-measurements/5C92816F17C248B71022694D704D983F> (visited on 2023-10-06).
- [77] T. Völker and I. B. Gornushkin, “Importance of physical units in the Boltzmann plot method,” *Journal of Analytical Atomic Spectrometry*, vol. 37, no. 10, pp. 1972–1974, 2022. DOI: [10.1039/D2JA00241H](https://doi.org/10.1039/D2JA00241H). [Online]. Available: <https://pubs.rsc.org/en/content/articlehtml/2022/ja/d2ja00241h> (visited on 2023-10-06).

REFERENCES

- [78] Z. F. Bao and A. J. Higgins,
“Two-Dimensional Simulation of Laser Thermal Propulsion Heating Chamber,”
in *AIAA Propulsion and Energy 2020 Forum*,
American Institute of Aeronautics and Astronautics. doi: [10.2514/6.2020-3518](https://doi.org/10.2514/6.2020-3518).
[Online]. Available: <https://arc.aiaa.org/doi/abs/10.2514/6.2020-3518>
(visited on 2023-11-27).

Appendix A

YLR-300/3000-QCW-MM-AC calibration report



TEST RESULTS
YTTERBIUM FIBER LASER
Model YLR-300/3000-QCW-MM-AC
S/N PLMP31901422

Form:
Revision:
Spec:
Page:

P69-00051
1
G22-29650 rev.4
1 of 6

This product is covered by the U.S. Pat. Nos. 5,422,897 and 5,774,484 and any foreign counterparts thereof, and other patents pending.

The information and the following charts provided below is the result of tests performed in controlled environments by IPG Photonics. These provided useful, but not warranted, information about the functions and performance of the product.

N	Characteristic	Symbol	Test Conditions	Min	Typ.	Max	Test Results	Unit
Optical characteristics								
1.1	Operation Mode			Pulsed / CW			Pulsed / CW	
1.2	Maximum Average Power	$P_{average}$	Pulsed mode	300			307.9	W
		P_{CW}	CW mode	300			342.0	W
1.3	Maximum Peak Power	P_{peak}	Pulsed mode				3079.25	W
1.4	Duty Cycle	DC	Pulsed mode			50 ¹⁾	Tested	%
1.5	Pulse Duration	τ	Pulsed mode	0.2		50 ²⁾	0.2-50	ms
1.6	Maximal Pulse Energy	E_{max}	Pulsed mode	30			30.8	J
1.7	Emission Wavelength	λ			1070		1069.6	nm
1.8	Emission Linewidth	$\Delta\lambda$	Pulsed mode maximum output power		5	6	1	nm
1.9	Long-term Power Instability		T = const maximum output power CW & Pulsed mode		± 0.5	± 1	± 0.5	%
Optical output								
2.1	Output Fiber Termination			QBH-compatible connector			Tested	
2.2	Beam Quality	BPP ³⁾	50µm core fiber pulsed mode	1		2	2	mm x mrad
General characteristics								
3.1	Cooling Method			Forced Air				
Electrical characteristics								
4.1	Operating Voltage, single phase			200-240 VAC, 50/60 Hz				VAC

¹⁾ Maximum duty cycle limit is inversely proportional to peak power: 10% for 3000W, 15% for 2000W, ..., 50% for 600W and lower.

²⁾ Maximum pulse duration limit is inversely proportional to peak power: 10ms for 3000W, 15ms for 2000W, ..., 50ms for 600W and lower.

³⁾ Measurement tolerance for BPP is +/- 10%.



TEST RESULTS
YTTERBIUM FIBER LASER
Model YLR-300/3000-QCW-MM-AC
S/N PLMP31901422

Form:
Revision:
Spec:
Page:

P69-00051
1
G22-29650 rev.4
2 of 6

N	Characteristic	Test Conditions	Test Results
Laser interfaces			
5.1	Control	Analog	Tested
		RS-232	Tested
		Ethernet	Tested

Date: 29.10.2019

Tested by: Henry Thepsimoung

Approved by: Thomas Rogers

This document has been created automatically and is valid without a signature

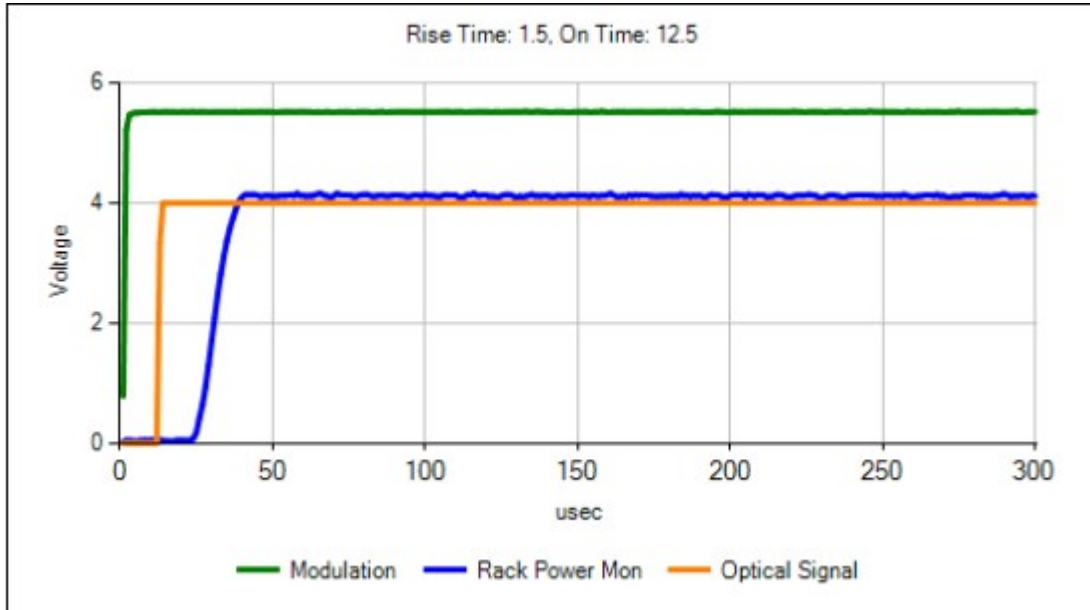


Fig. 1 Switching ON characteristic at nominal output power

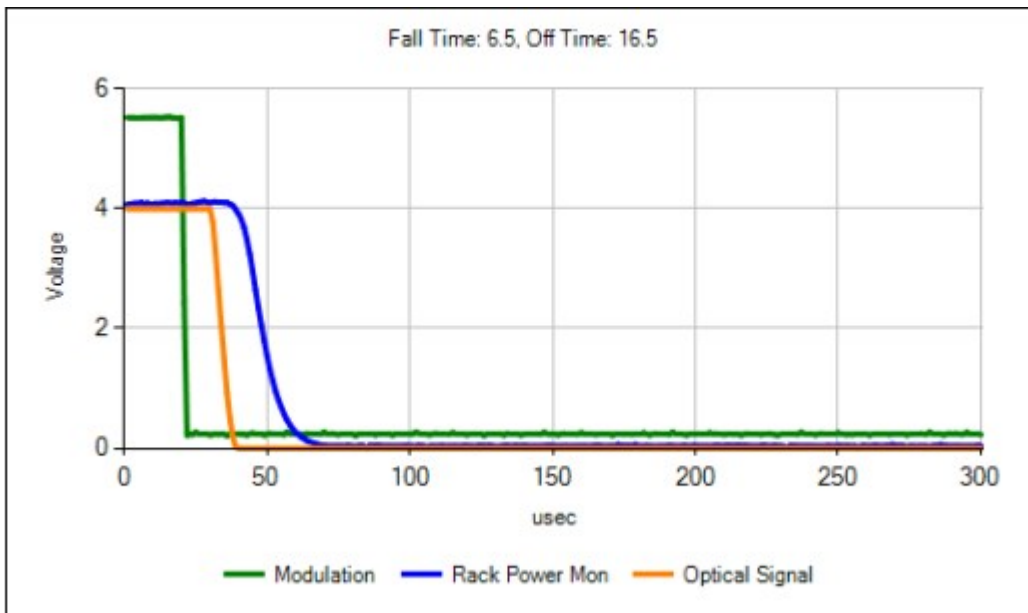


Fig. 2 Switching OFF characteristic at nominal output power

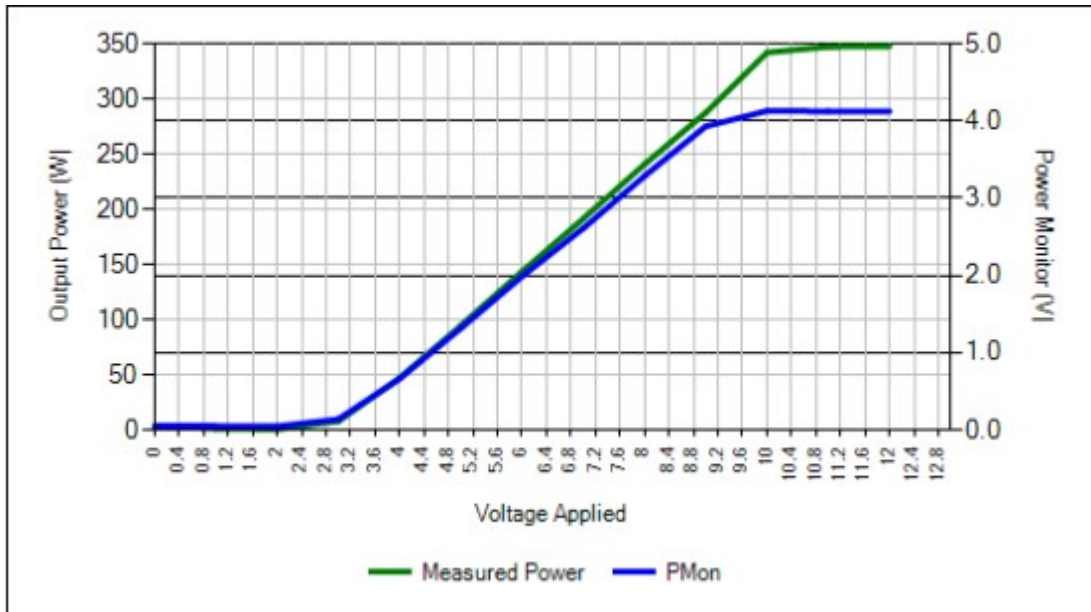


Fig. 3 CW Mode: Output Power vs. Analog Voltage

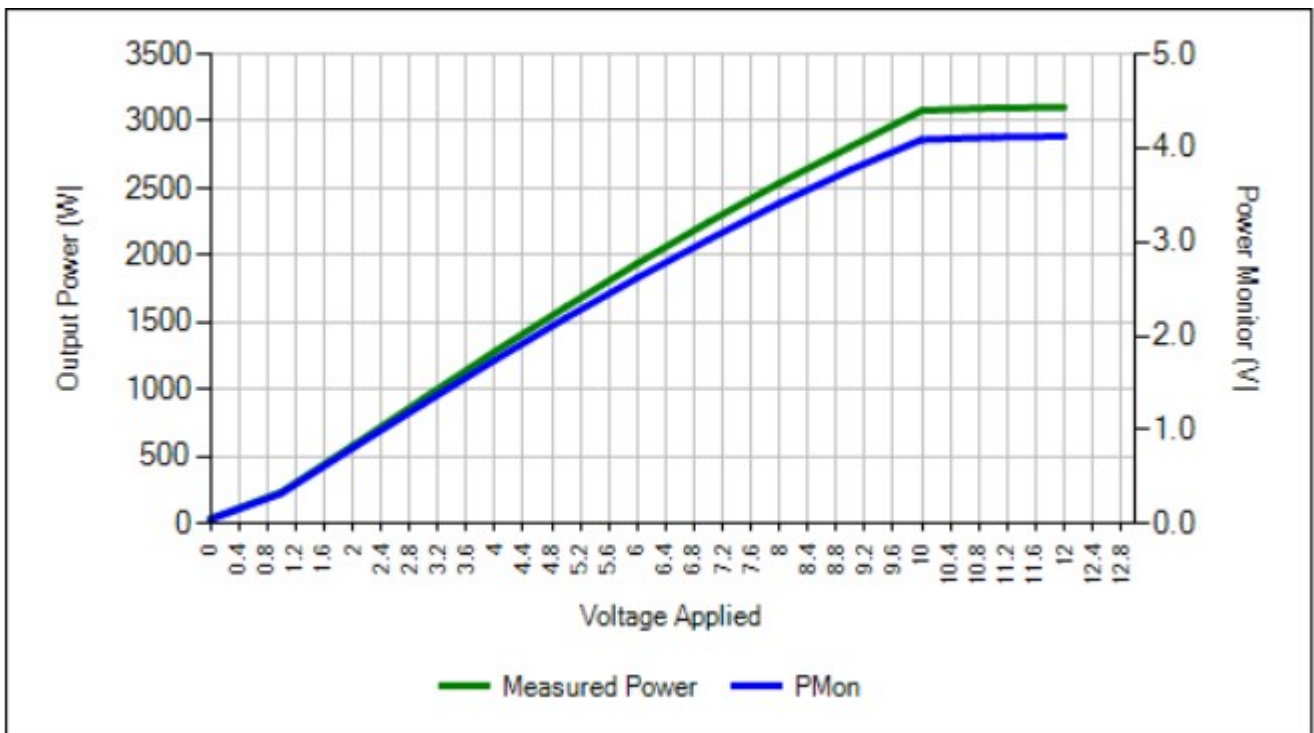


Fig. 4 Pulsed Mode: Peak Output vs. Analog Voltage at RR=10Hz, 10% Duty Cycle

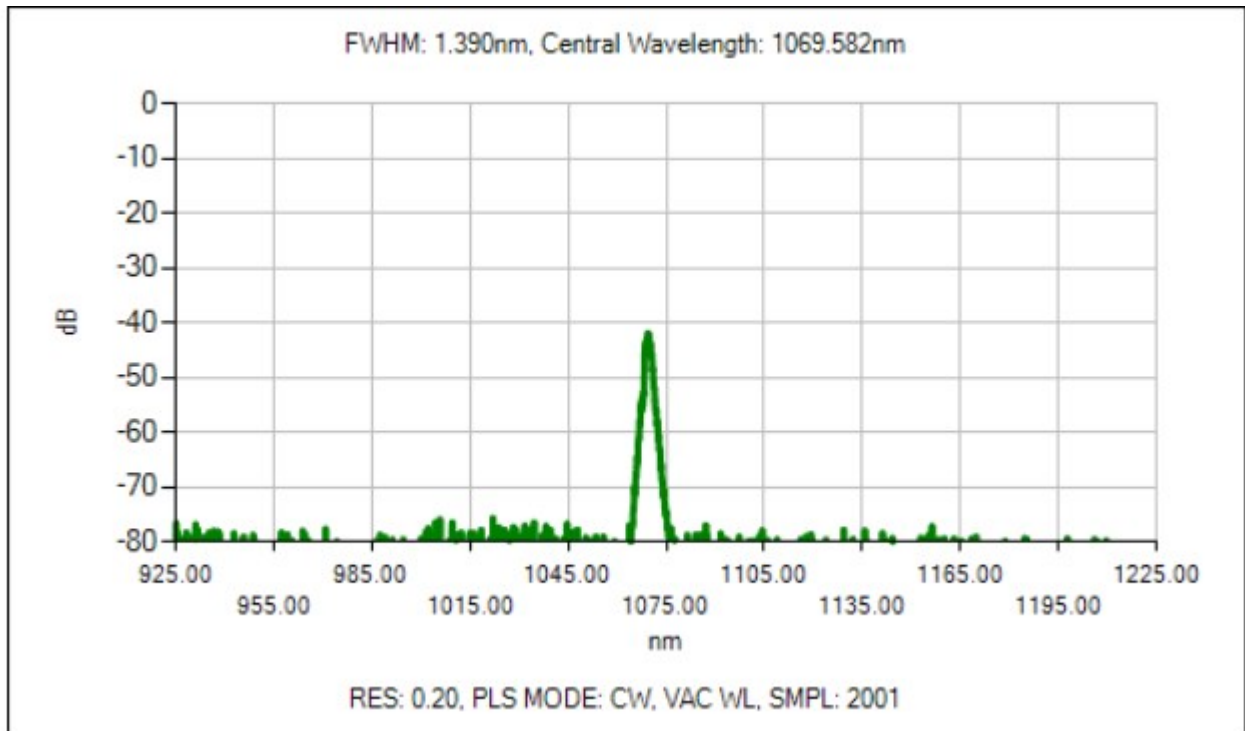


Fig. 5 Output Spectrum at Nominal Output Power

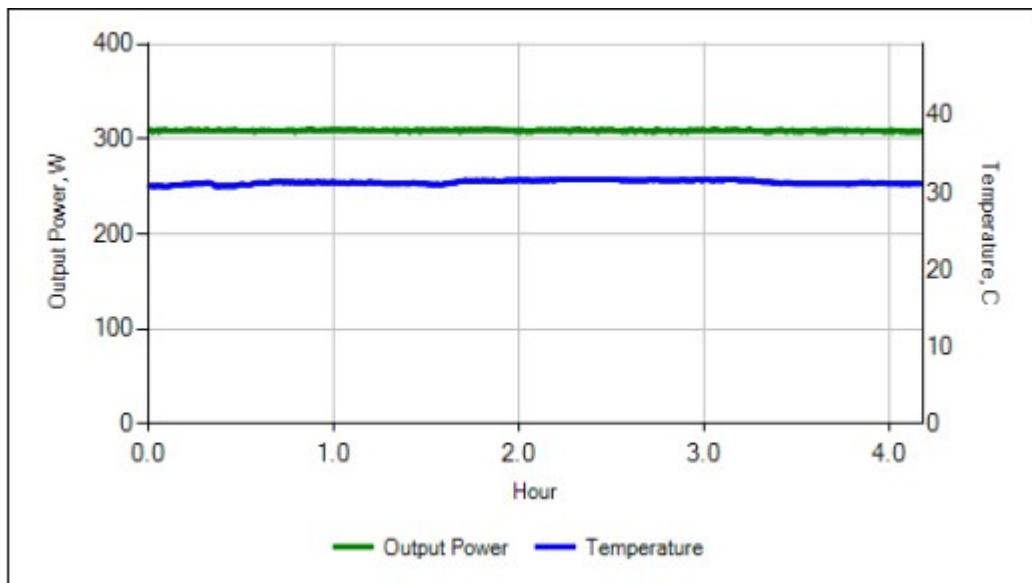


Fig. 6 Output Power Stability Chart

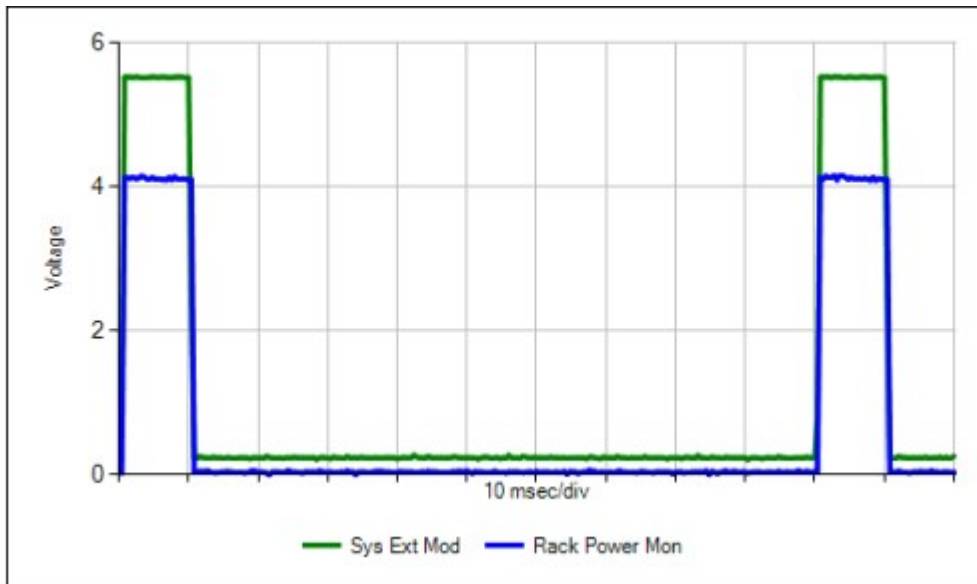


Fig. 7 Pulsed Mode: Laser Output Signal Frequency 10Hz (10% Duty Cycle)

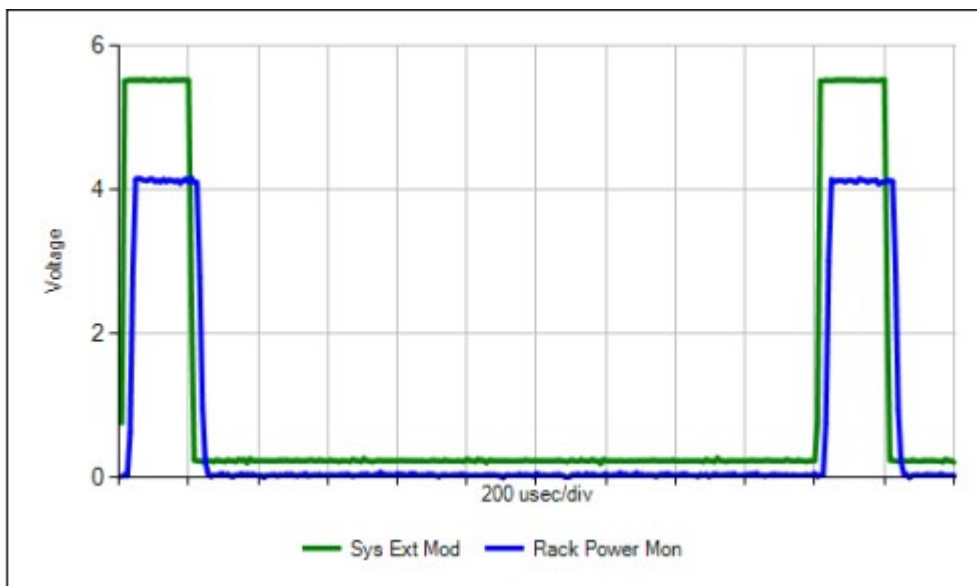


Fig. 8 Pulsed Mode: Laser Output Signal Frequency 500Hz (10% Duty Cycle)

Appendix B

P30 collimator calibration report

	Model:	P30-001736
	Serial Number:	CO211706
	Date:	3/29/2022 3:11:04 PM
	Tested By:	Ketsana Chanthavangso

Collimator Test Results Sheet

Characteristic	Conditions	Min.	Typical	Max.	Tested	Units
Z-Position	Measured at Beam Waist				-0.066	m
BPP	Algo. 2nd 100 W			2.5	1.472	mm*mrad
Safety Interlock	Circuit Continuity Tested				Pass	-
Leak Testing	80psi Air for 15min.					-

Raw-Beam: ✕

Raw-Beam:

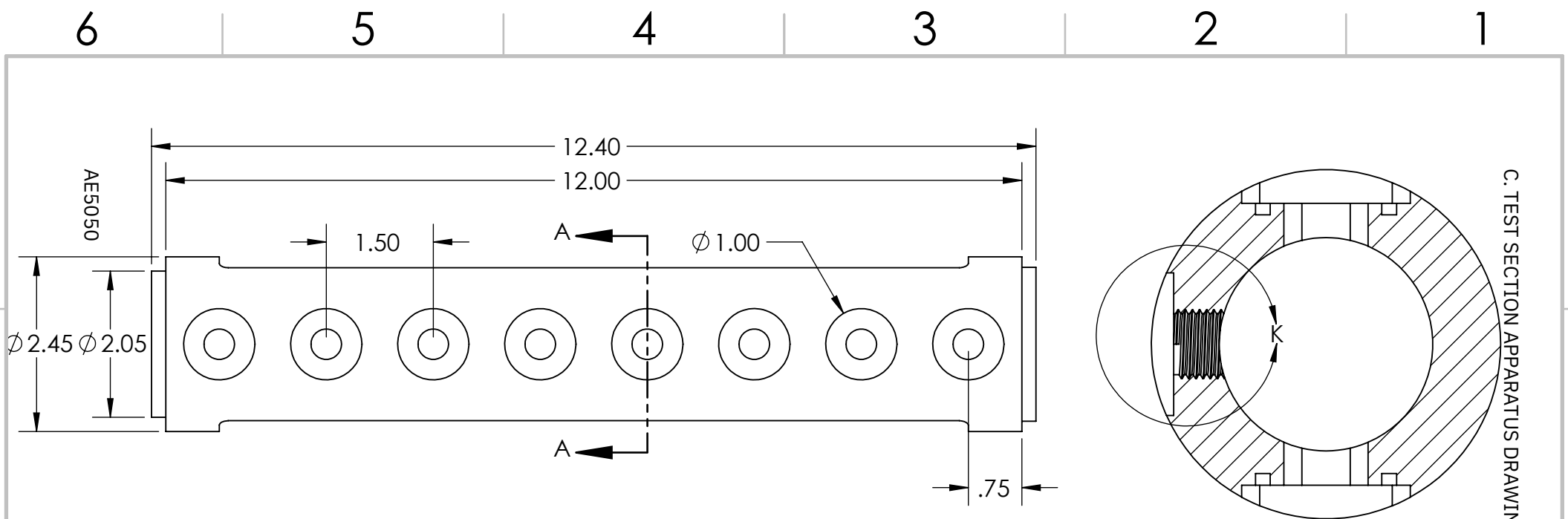
Position Z:	-66.288 [mm]
Position Z(X):	-3.131 [m]
Position Z(Y):	3.635 [m]
Raw-Beam Radius:	6.813 [mm]
Raw-Beam Radius (X):	6.614 [mm]
Raw-Beam Radius (Y):	6.917 [mm]
Rayleigh length:	31.531 [m]
Rayleigh length X:	29.099 [m]
Rayleigh length Y:	33.790 [m]
Divergence Angle:	0.432[mrad]
Divergence Angle (X):	0.455[mrad]
Divergence Angle (Y):	0.409[mrad]
Raw-Beam Dia. at Laser	13.626[mm]

Exit

Appendix C

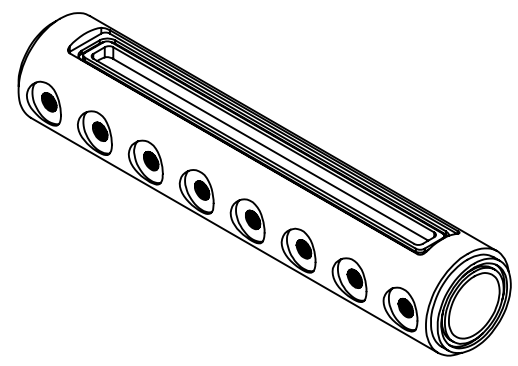
Test section apparatus drawings

The test section used in this thesis was originally designed to study the onset of cavitation in piston-cylinder assemblies. These drawings were drafted by John Kokkalis at McGill University, reproduced here with his permission. Although the apparatus represented here was not the iteration used in his final work, the final iteration of this system can be found in his Master's thesis [[52](#)].

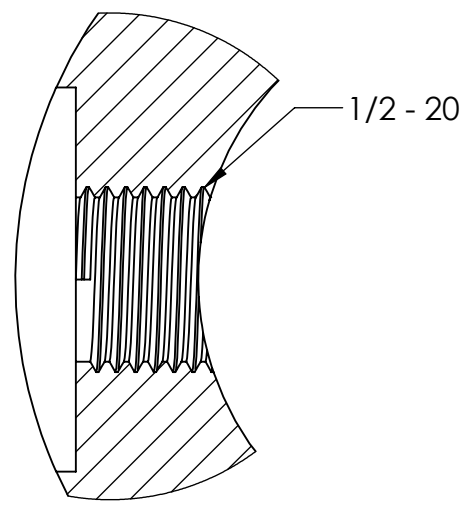


C. TEST SECTION APPARATUS DRAWINGS

SECTION A-A
SCALE 1 : 1

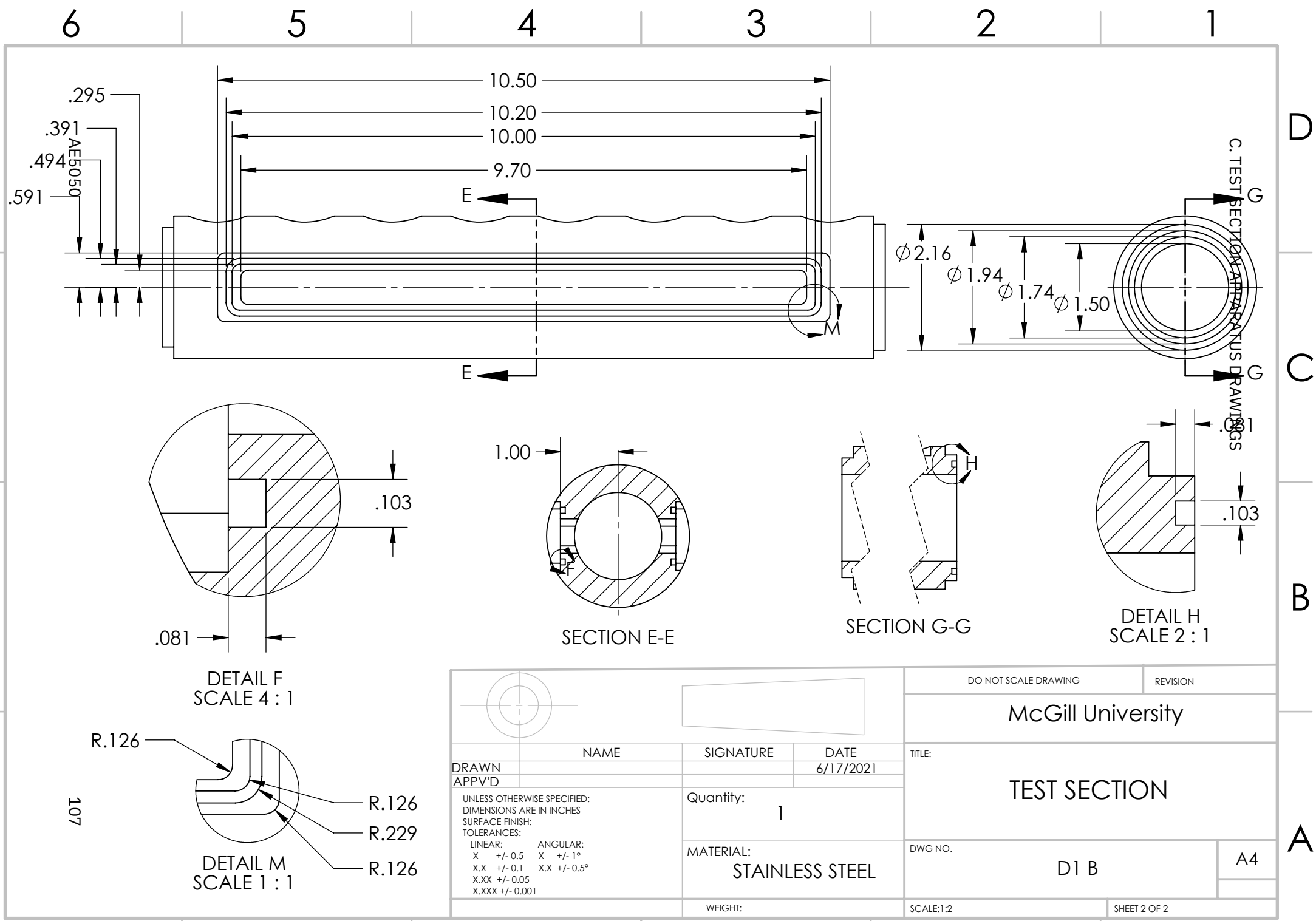


- NOTE:
- 1) Leave the exterior of tube as provided.
 - 2) Equal spacing between grooves.
 - 3) Bore groove until flat (shown in Detail k).



DETAIL K
SCALE 2 : 1

		DO NOT SCALE DRAWING		REVISION	
		McGill University			
DRAWN APPV'D		NAME	SIGNATURE	DATE	TITLE:
UNLESS OTHERWISE SPECIFIED: DIMENSIONS ARE IN INCHES SURFACE FINISH: TOLERANCES: LINEAR: ANGULAR: X +/- 0.5 X +/- 1° X.X +/- 0.1 X.X +/- 0.5° X.XX +/- 0.05 X.XXX +/- 0.001		Quantity: 1		6/17/2021	
		MATERIAL: STAINLESS STEEL		TEST SECTION	
		WEIGHT:		DWG NO. D1 A	
				A4	
				SCALE:1:2	
				SHEET 1 OF 2	



C. TEST SECTION APPARATUS DRAWINGS

DETAIL F
SCALE 4 : 1

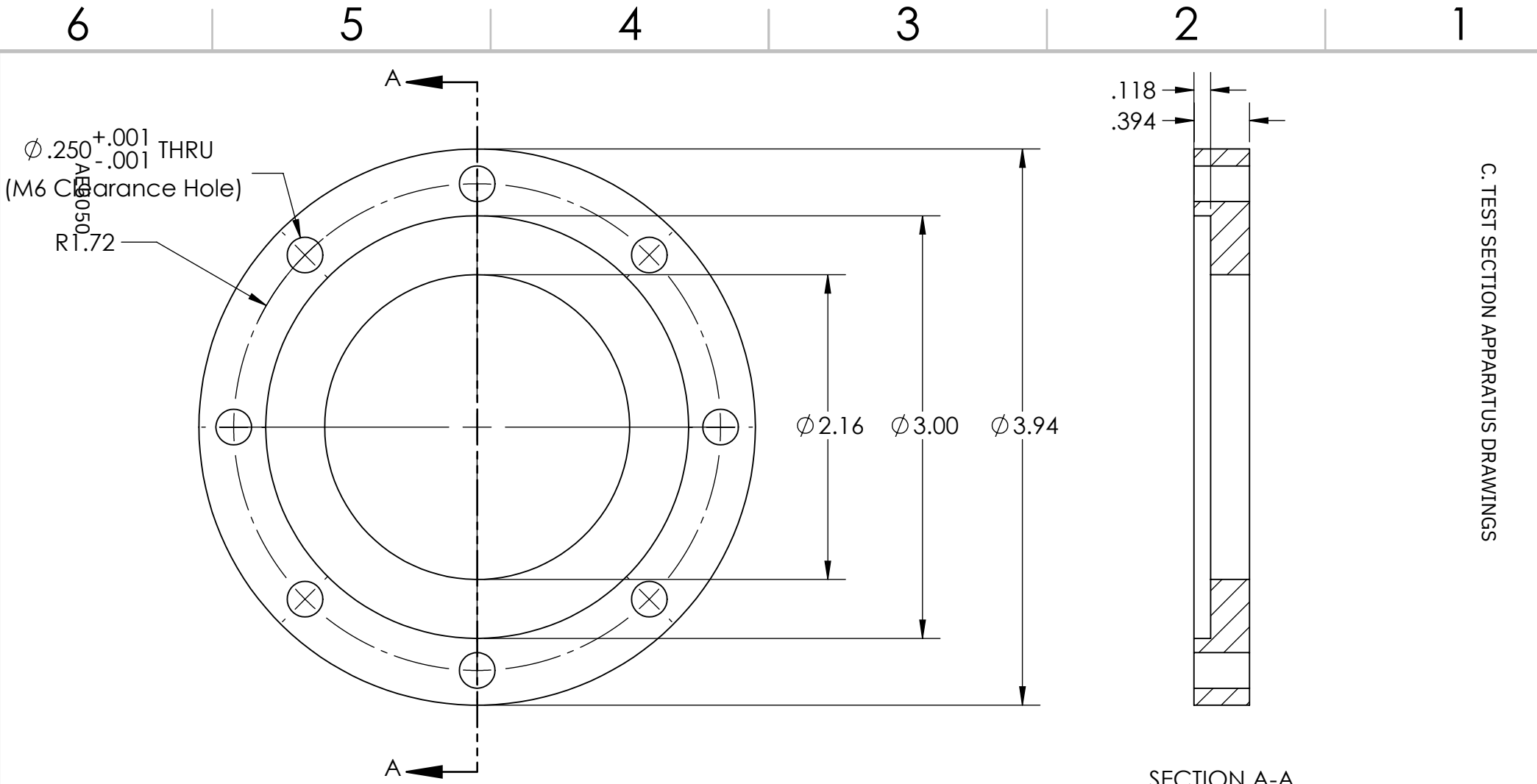
SECTION E-E

SECTION G-G

DETAIL H
SCALE 2 : 1

DETAIL M
SCALE 1 : 1

			DO NOT SCALE DRAWING		REVISION	
			McGill University			
DRAWN APPV'D			NAME	SIGNATURE	DATE 6/17/2021	
UNLESS OTHERWISE SPECIFIED: DIMENSIONS ARE IN INCHES SURFACE FINISH: TOLERANCES: LINEAR: ANGULAR: X +/- 0.5 X +/- 1° X.X +/- 0.1 X.X +/- 0.5° X.XX +/- 0.05 X.XXX +/- 0.001			Quantity:		1	
			MATERIAL:		STAINLESS STEEL	
			WEIGHT:		DWG NO. D1 B	
					A4	
			SCALE:1:2		SHEET 2 OF 2	



SECTION A-A

C. TEST SECTION APPARATUS DRAWINGS

				DO NOT SCALE DRAWING		REVISION
				McGill University		
DRAWN APPV'D	NAME	SIGNATURE	DATE	TITLE:		
UNLESS OTHERWISE SPECIFIED: DIMENSIONS ARE IN INCHES SURFACE FINISH: TOLERANCES: LINEAR: ANGULAR: X +/- 0.5 X +/- 1° X.X +/- 0.1 X.X +/- 0.5° X.XX +/- 0.05 X.XXX +/- 0.001		Quantity: 1		FLANGE		
		MATERIAL: STAINLESS STEEL				
		WEIGHT:		DWG NO. D2	A4	
				SCALE: 1:1	SHEET 1 OF 1	

108

6 5 4 3 2 1

D

C

B

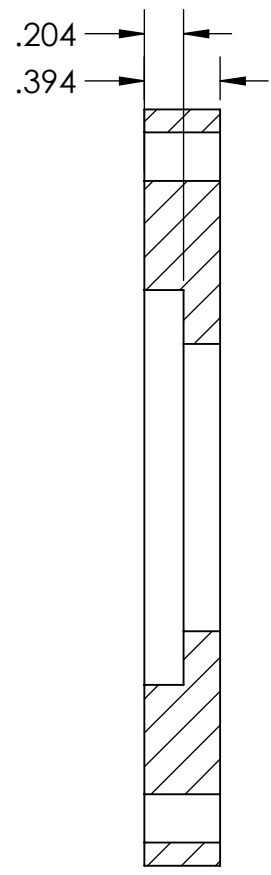
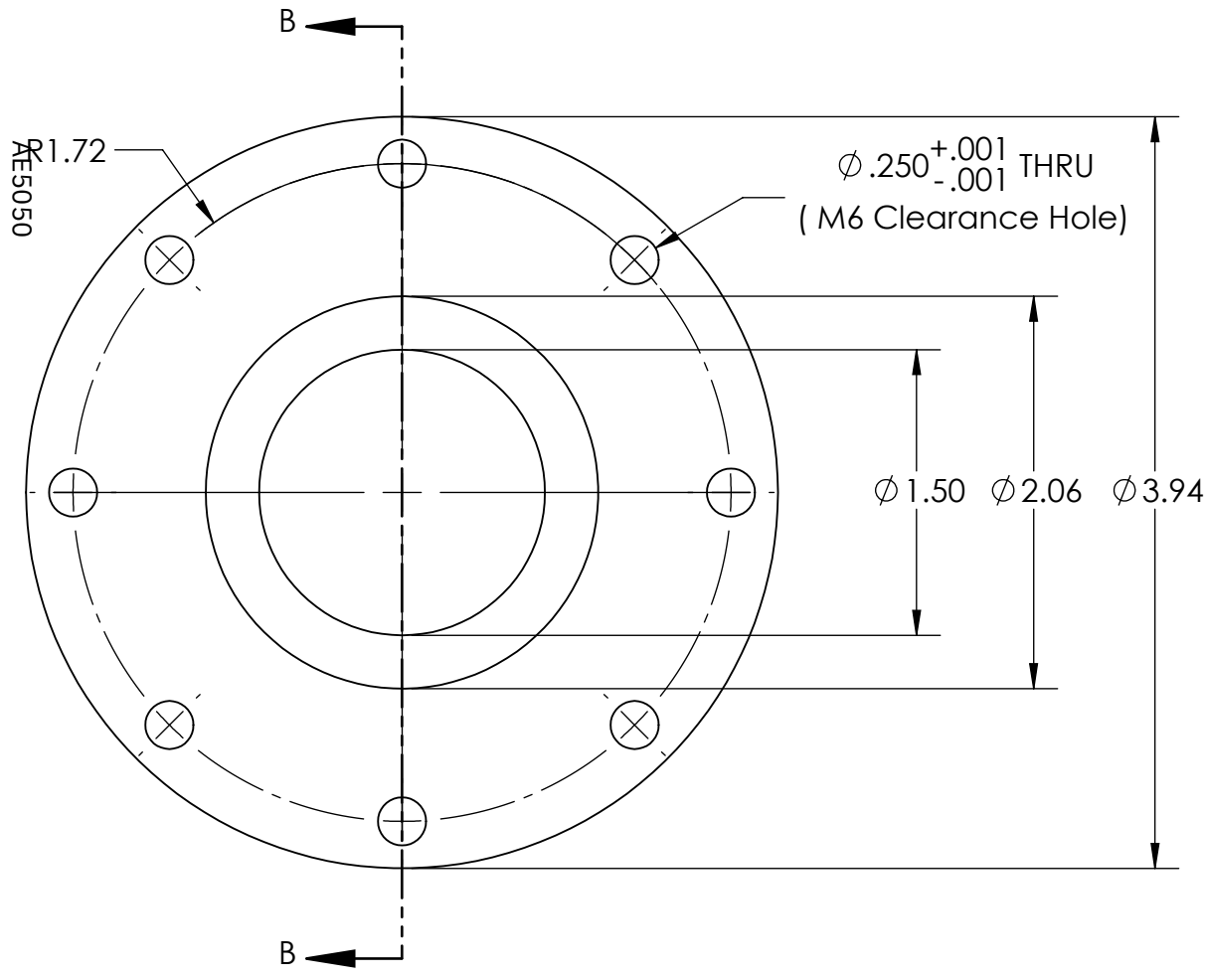
A

D

C

B

A



SECTION B-B
SCALE 1 : 1

C. TEST SECTION APPARATUS DRAWINGS

109

				DO NOT SCALE DRAWING		REVISION
				McGill University		
DRAWN APPV'D	NAME	SIGNATURE	DATE	TITLE:		
UNLESS OTHERWISE SPECIFIED: DIMENSIONS ARE IN INCHES SURFACE FINISH: TOLERANCES: LINEAR: ANGULAR: X +/- 0.5 X +/- 1° X.X +/- 0.1 X.X +/- 0.5° X.XX +/- 0.05 X.XXX +/- 0.001		Quantity:	1	End Flange		
		MATERIAL:	STAINLESS STEEL			
		WEIGHT:		DWG NO.	D3	A4
				SCALE:1:2	SHEET 1 OF 1	

6 5 4 3 2 1

6

5

4

3

2

1

D

D

C

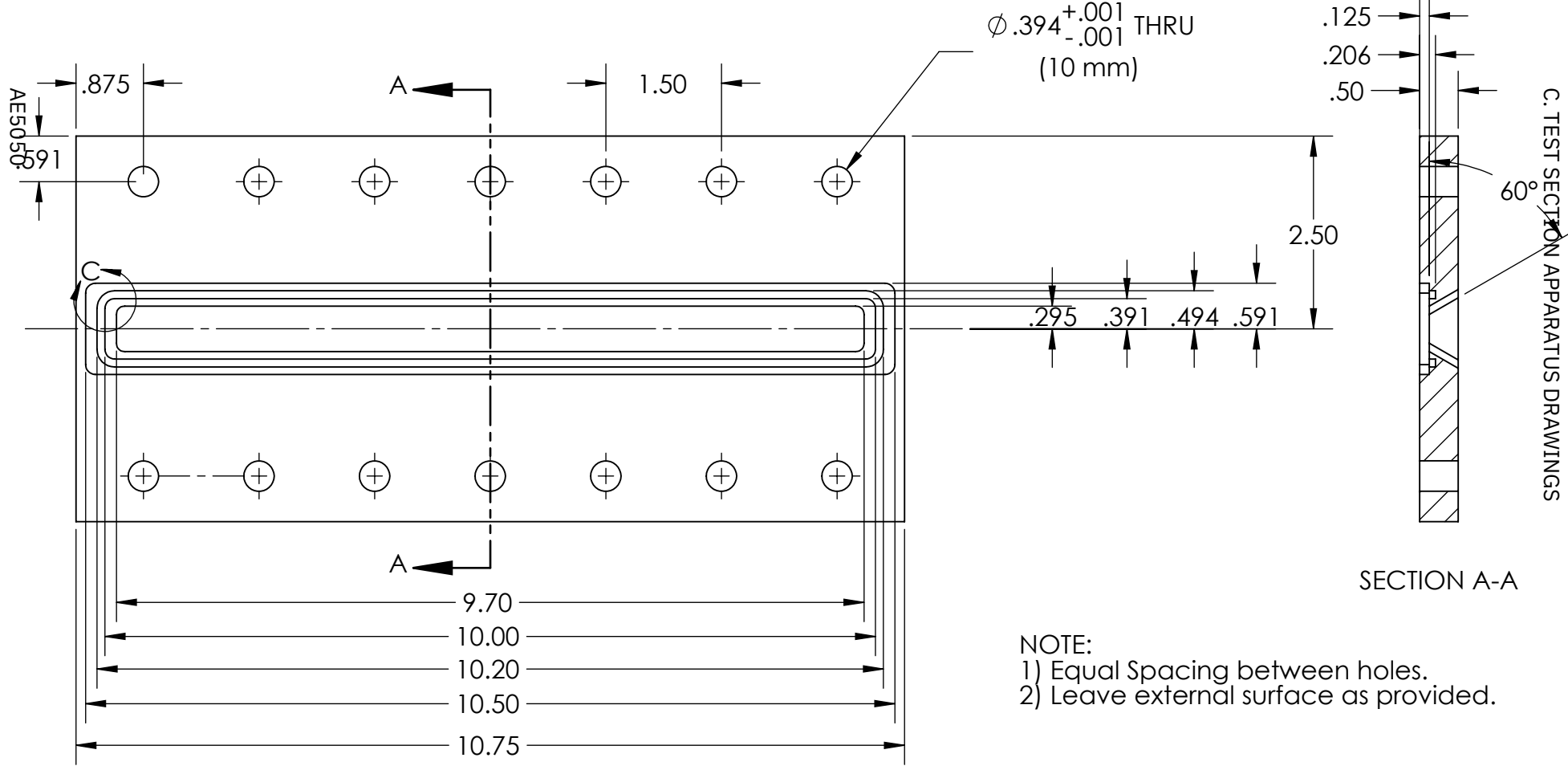
C

B

B

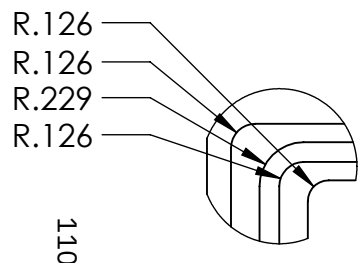
A

A



SECTION A-A

NOTE:
 1) Equal Spacing between holes.
 2) Leave external surface as provided.



DETAIL C
SCALE 1 : 1

			
DRAWN APPV'D	NAME	SIGNATURE	DATE 6/7/2021
UNLESS OTHERWISE SPECIFIED: DIMENSIONS ARE IN INCHES SURFACE FINISH: TOLERANCES: LINEAR: ANGULAR: X +/- 0.5 X +/- 1° X.X +/- 0.1 X.X +/- 0.5° X.XX +/- 0.05 X.XXX +/- 0.001		Quantity: 2	MATERIAL: STAINLESS STEEL
		WEIGHT:	SCALE: 1:2

DO NOT SCALE DRAWING		REVISION	
McGill University			
TITLE: External Clamp			
DWG NO.		A4	
D4		SHEET 1 OF 1	

6

5

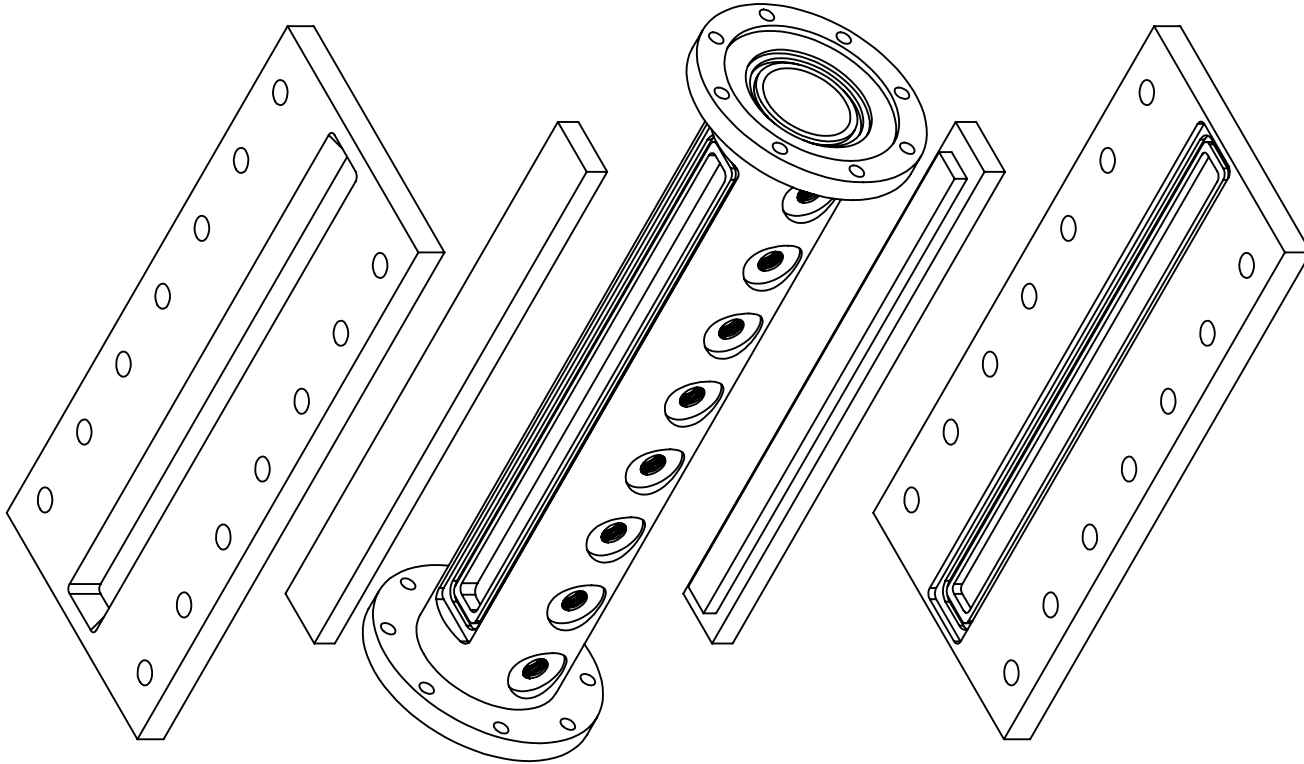
4

3

2

1

AE5050



C. TEST SECTION APPARATUS DRAWINGS

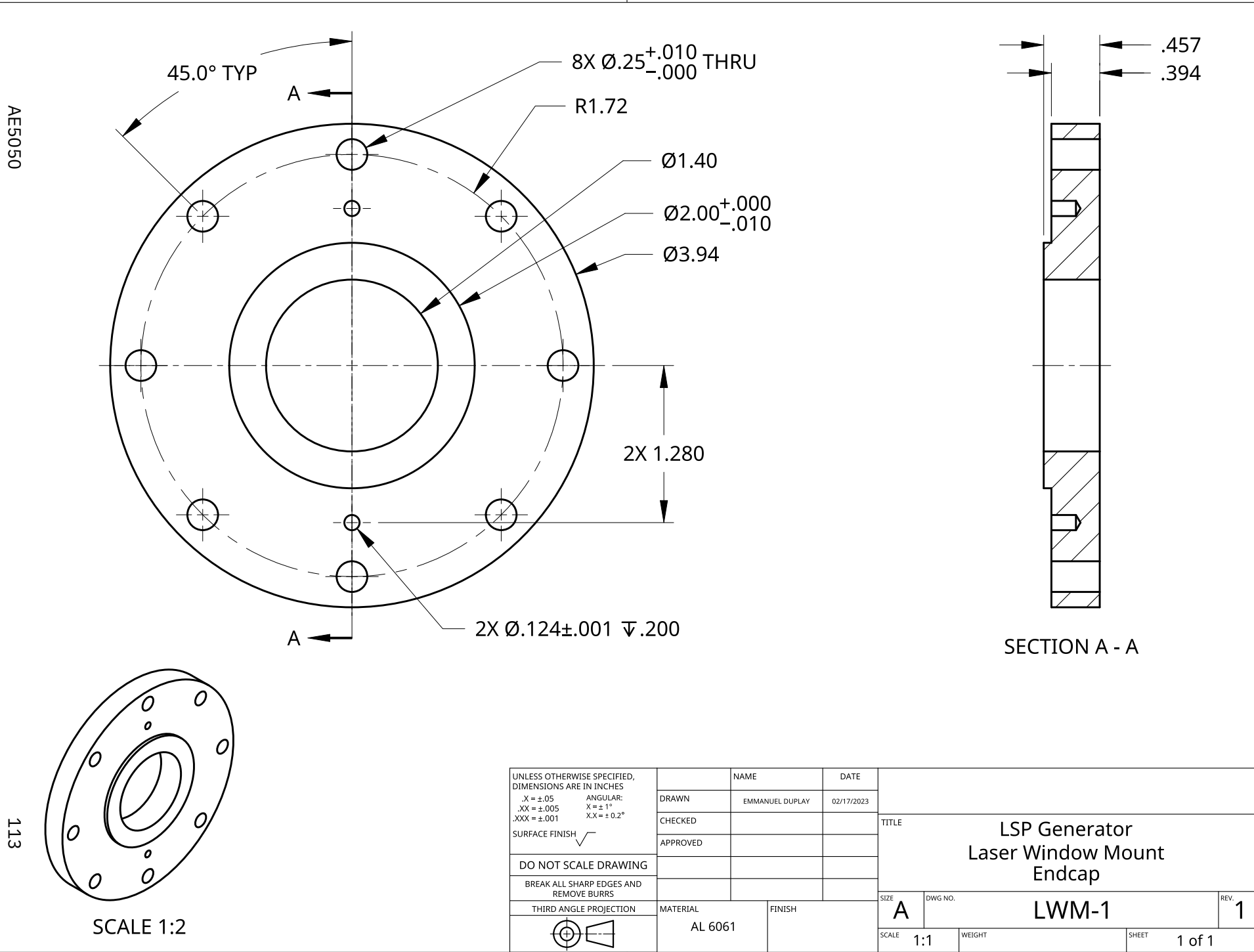


DRAWN APPV'D	NAME	SIGNATURE	DATE
			6/22/2021
UNLESS OTHERWISE SPECIFIED: DIMENSIONS ARE IN INCHES SURFACE FINISH: TOLERANCES: LINEAR: ANGULAR: X +/- 0.5 X +/- 1° X.X +/- 0.1 X.X +/- 0.5° X.XX +/- 0.05 X.XXX +/- 0.001		Quantity:	
		MATERIAL:	
		WEIGHT:	

DO NOT SCALE DRAWING		REVISION
McGill University		
TITLE: Assembly Drawing		
DWG NO.	D5	A4
SCALE:1:2	SHEET 1 OF 1	

Appendix D

Laser window mount drawings



AE5050

B

A

113

SCALE 1:2

UNLESS OTHERWISE SPECIFIED,
DIMENSIONS ARE IN INCHES
.X = ±.05 ANGULAR:
.XX = ±.005 X = ± 1°
.XXX = ±.001 .XX = ± 0.2°
SURFACE FINISH

DO NOT SCALE DRAWING

BREAK ALL SHARP EDGES AND REMOVE BURRS

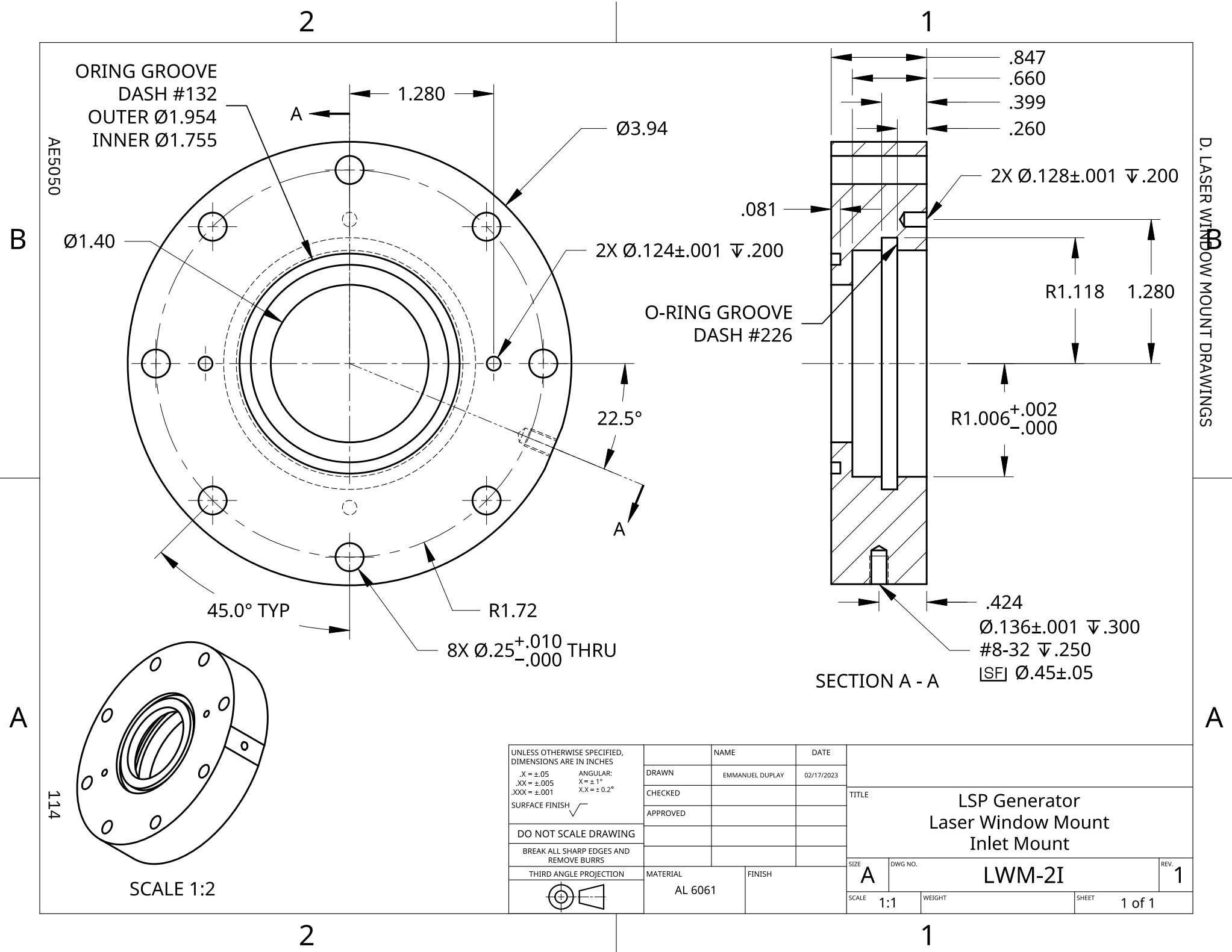
THIRD ANGLE PROJECTION

	NAME	DATE
DRAWN	EMMANUEL DUPLAY	02/17/2023
CHECKED		
APPROVED		
MATERIAL	FINISH	
AL 6061		

TITLE		
LSP Generator Laser Window Mount Endcap		
SIZE	DWG NO.	REV.
A	LWM-1	1
SCALE	WEIGHT	SHEET
1:1		1 of 1

D. LASER WINDOW MOUNT DRAWINGS

A



D. LASER WINDOW MOUNT DRAWINGS

ORING GROOVE
DASH #132
OUTER Ø1.954
INNER Ø1.755

AE5050

B

Ø1.40

Ø3.94

2X Ø.124±.001 ∇.200

O-RING GROOVE
DASH #226

22.5°

45.0° TYP

R1.72

8X Ø.25^{+0.010}_{-.000} THRU

1

.847
.660
.399
.260

2X Ø.128±.001 ∇.200

.081

R1.118 1.280

R1.006^{+0.002}_{-.000}

SECTION A - A

.424
Ø.136±.001 ∇.300
#8-32 ∇.250
[SF] Ø.45±.05

A

A

114

SCALE 1:2

UNLESS OTHERWISE SPECIFIED,
DIMENSIONS ARE IN INCHES
.X = ±.05 ANGULAR:
.XX = ±.005 X = ±1°
.XXX = ±.001 XX = ± 0.2°
SURFACE FINISH

DO NOT SCALE DRAWING

BREAK ALL SHARP EDGES AND
REMOVE BURRS

THIRD ANGLE PROJECTION



	NAME	DATE
DRAWN	EMMANUEL DUPLAY	02/17/2023
CHECKED		
APPROVED		

TITLE		LSP Generator Laser Window Mount Inlet Mount	
SIZE	DWG NO.	REV.	
A	LWM-2I	1	
SCALE	WEIGHT	SHEET	1 of 1
1:1			

2

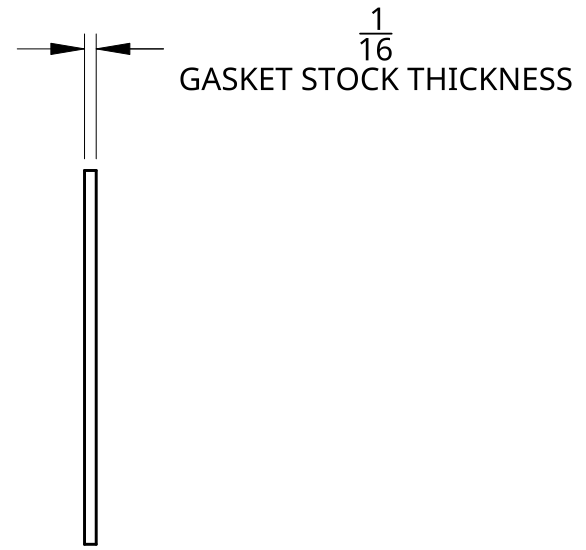
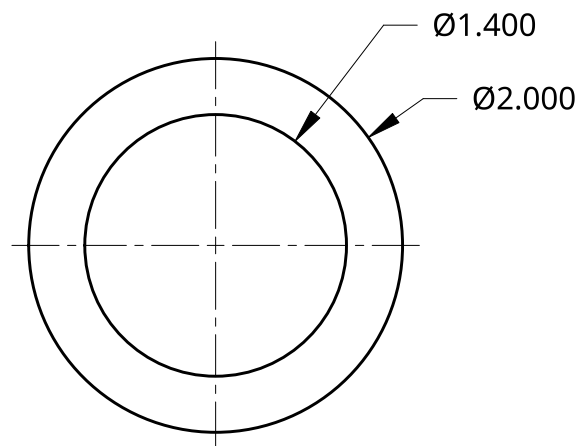
1

2

1

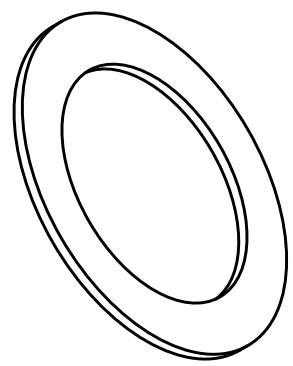
AE5050

B



D. LASER WINDOW MOUNT DRAWINGS

A



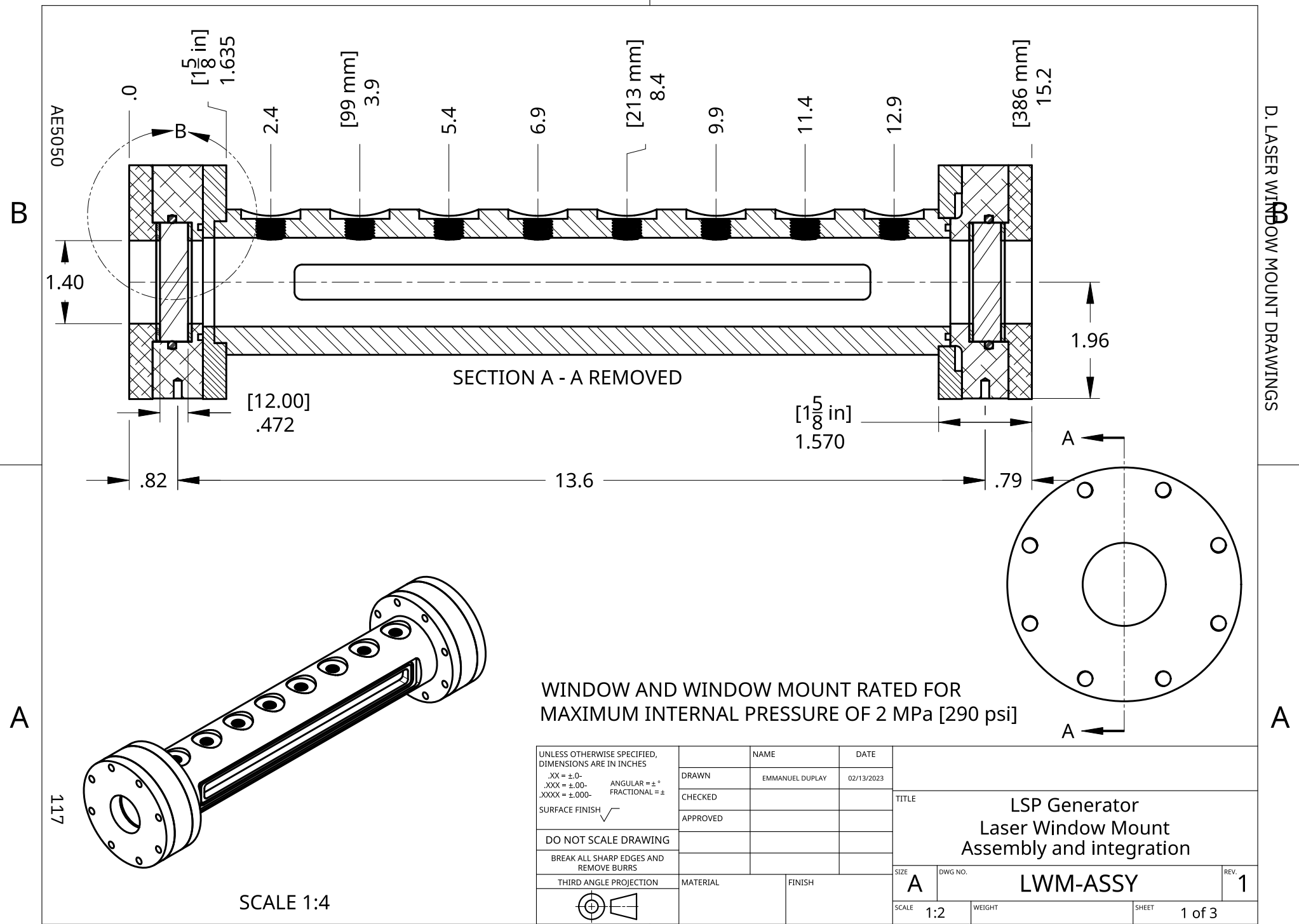
116

A

UNLESS OTHERWISE SPECIFIED, DIMENSIONS ARE IN INCHES		NAME	DATE	TITLE LSP Generator Laser Window Mount Gasket		
.X = ±.05	ANGULAR: X = ± 1°	DRAWN	EMMANUEL DUPLAY			02/17/2023
.XX = ±.005	X.X = ± 0.5°	CHECKED				
.XXX = ±.001		APPROVED				
SURFACE FINISH				SIZE	REV.	
DO NOT SCALE DRAWING				A	0	
BREAK ALL SHARP EDGES AND REMOVE BURRS				DWG NO. LWM-G		
THIRD ANGLE PROJECTION		MATERIAL	FINISH	SCALE	SHEET	
		BUNA-N RUBBER		1:1	1 of 1	

2

1



WINDOW AND WINDOW MOUNT RATED FOR
MAXIMUM INTERNAL PRESSURE OF 2 MPa [290 psi]

UNLESS OTHERWISE SPECIFIED, DIMENSIONS ARE IN INCHES		NAME	DATE	TITLE	
.XX = ±0-	ANGULAR = ±°	DRAWN	02/13/2023	LSP Generator Laser Window Mount Assembly and integration	
.XXX = ±0.0-	FRACTIONAL = ±	CHECKED			
.XXXX = ±.000-		APPROVED			
SURFACE FINISH <input checked="" type="checkbox"/>		MATERIAL		SIZE	REV.
DO NOT SCALE DRAWING		FINISH		A	1
BREAK ALL SHARP EDGES AND REMOVE BURRS		THIRD ANGLE PROJECTION		SCALE	1 of 3
				1:2	1

2

1

AE5050

B

D. LASER WINDOW MOUNT DRAWINGS



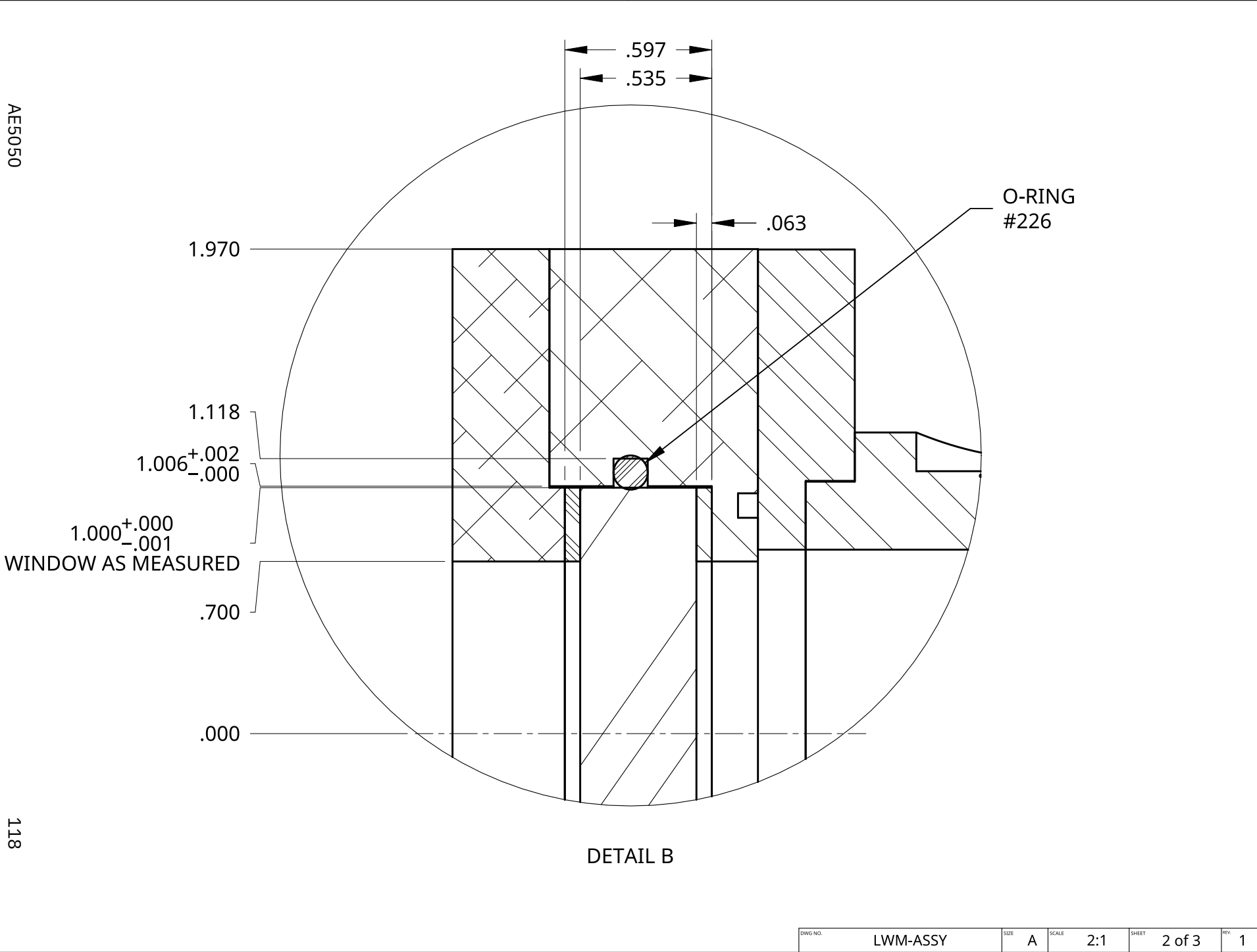
A

A

118

2

1



DETAIL B

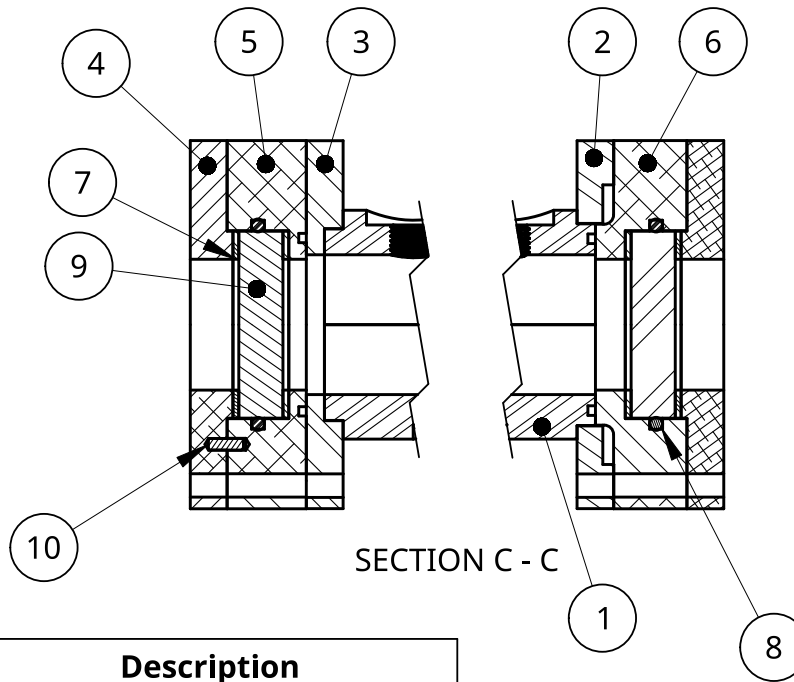
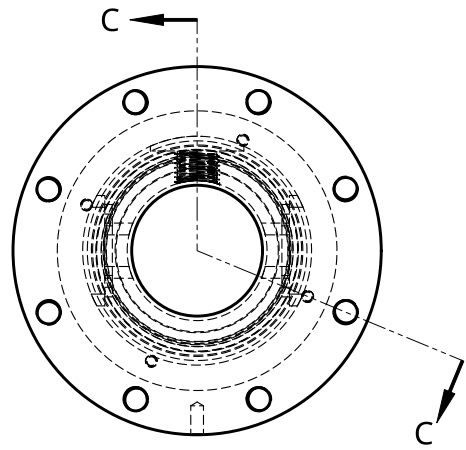
DWG NO.	LWM-ASSY	SIZE	A	SCALE	2:1	SHEET	2 of 3	REV	1
---------	----------	------	---	-------	-----	-------	--------	-----	---

2

1

AE5050

B



SECTION C - C

D. LASER WINDOW MOUNT DRAWINGS

A

A

119

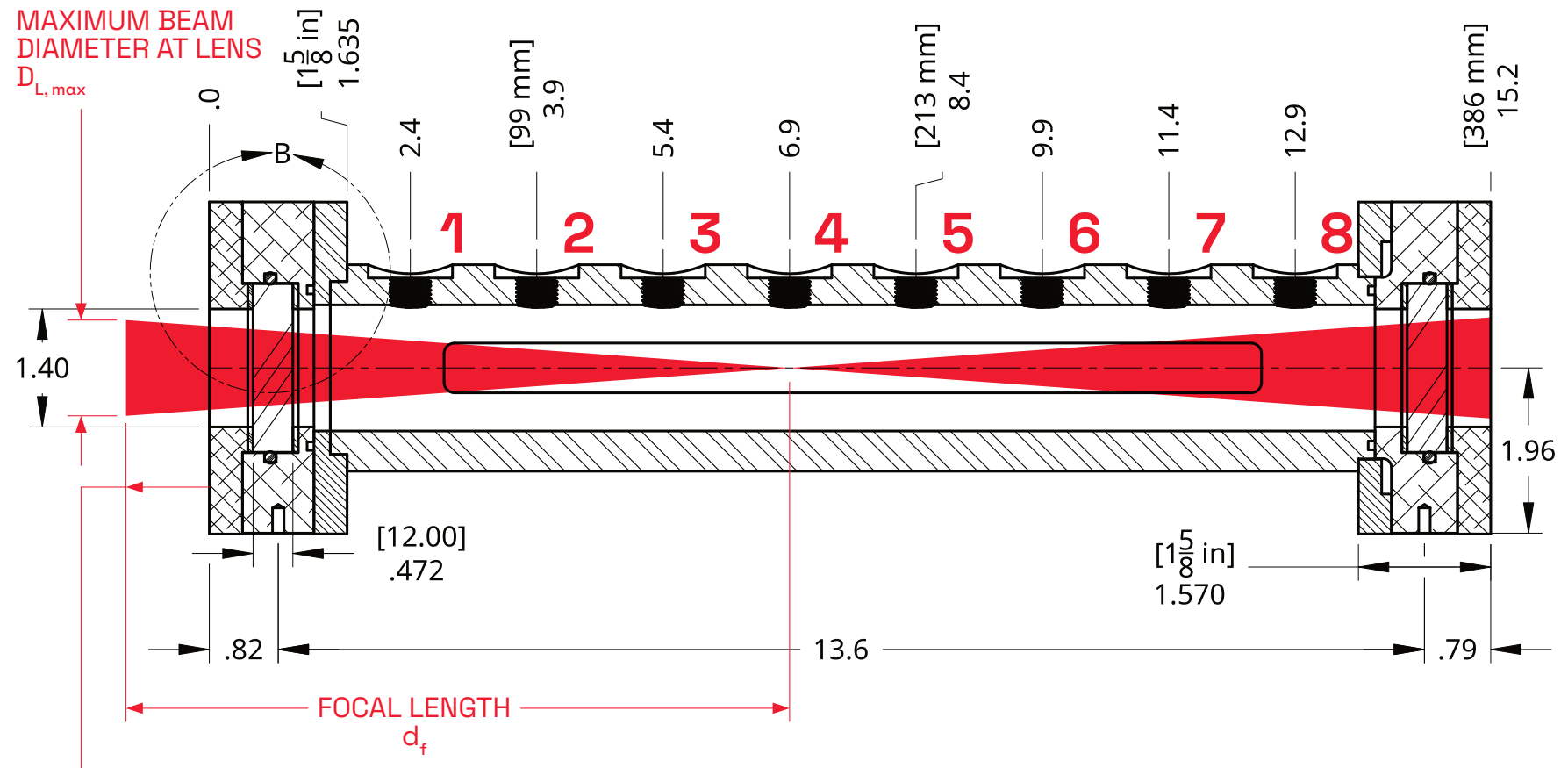
Item	Quantity	Part number	Description
1	1	FDV4-D1	Test section
2	1	FDV4-D2	Test section flange
3	1	FDV4-D3	Test section end flange
4	2	LWM-1	Window mount endcap
5	1	LWM-2I	Window mount, inlet
6	1	LWM-2O	Window mount, outlet
7	4	LWM-G	Window mount gasket
8	2	9452K64	Window o-ring (McMaster-Carr)
9	2	WG12012-C	N-BK7 window (Thorlabs)
10	4	98381A302	Dowel pins (McMaster-Carr)

DWG NO.	LWM-ASSY	SIZE	A	SCALE	1:2	SHEET	3 of 3	REV	1
---------	----------	------	---	-------	-----	-------	--------	-----	---

2

1

AE5050



D. LASER WINDOW MOUNT DRAWINGS

d_f [mm]	Sparkplug port #	$D_{L,max}$		d_o		f-number
		[mm]	[in]	[mm]	[in]	
60	1	5.61	0.221	-0.58	-0.023	10.69
100	2	10.59	0.417	1.32	0.052	9.44
150	3	18.34	0.722	13.21	0.520	8.18
200	4	28.85	1.136	25.12	0.989	6.93

120

1:2

Appendix E

Instrumentation datasheets and calibration reports

CERTIFICATE OF CALIBRATION



Certificate #: 308803-230223	Customer Name:
Model: UP55N-300F-H12-BLU-D0	V5
Serial Number: 308803	Instrument ID:
Cal. Procedure: 420- 19325	Date of Calibration: February 22, 2023
	Calibration Due Date: August 22, 2024

Calibration Data and Measurement Condition

Calibration Data				Measurement Conditions							
λ	Sensitivity	Instrument Uncertainty	Power Level		Cooling		Ambient Temp.	Relative Humidity	0-95% Risetime	Into Load	Beam Ø
			Power	Rep. Rate	Temp	Flow Rate					
μm	mV/W	% **	Watts	Hz	°C	l/min.	°C	%	s	Ω	mm
^P 1.064	0.0520	± 2.5	99.0	CW	N/A	N/A	21	12	2.0	N/A	40.0

^S Value Corrected According To Spectral Absorption Curve
^P Sensitivity programmed in detector head
^{**} % of Reading + ±5μV
^λ The detector is calibrated using a laser emitting at 1.070 μm

Test Equipment and Standards Used

ID#	Description	Serial#	Last Cal.	By	Certificate #
EOC-1235	IPG, YLR-500-MM-WC-Y14, Ytterbium Fiber CW Laser, beam profile: Gaussian	PLMP31801343	N/A	N/A	N/A
EOCE-919	Gentec-EO, UP55G, wattmeter	259592	Nov. 29, 2022	NIST	686198-O-0000042275
EOCE-753	Gentec-EO, UP Calibrator	240865	Jan. 24, 2023	Gentec-EO	240865-230124
EOCE-752	Gentec-EO, UP Calibrator	240863	Jan. 24, 2023	Gentec-EO	240863-230124

Declaration of Conformity

Gentec Electro-Optics certifies that, at the time of calibration, the above listed instrument meets or exceeds all specifications. It has been calibrated using standards traceable to the International System of Units (SI) through the National Institute of Standards and Technology (NIST), the National Research Council Canada (NRC) or other National Metrology Institutes. Calibration results relate only to the instrument being calibrated. Calibration activities are compliant to ISO 9001:2015 and ISO/IEC 17025:2017. Total expanded uncertainties are reported with a coverage factor k=2, providing a level of confidence of approximately 95%. Any statement of compliance is made without taking measurement uncertainty into account and is based on the instrument's uncertainty.

Signature Signature	Alexandre Loranger Calibrated by Charles Lalancette Quality Assurance	February 23, 2023 Date of Issue Feb. 27, 2023 Date of Inspection
------------------------	---	--

Variance Report

	Last Calibration	As Received	New Calibration
Date	N/A	N/A	February 22, 2023
Sensitivity (mV/W)	N/A	N/A	0.0520
Difference (from last calibration)	N/A	N/A	N/A
Change (%)	N/A	N/A	N/A
Status	N/A	N/A	Within Tolerance

Remark : there is no "Last Calibration" and "As Received" calibration for a new instrument.

No reproduction of this document is permitted except in full

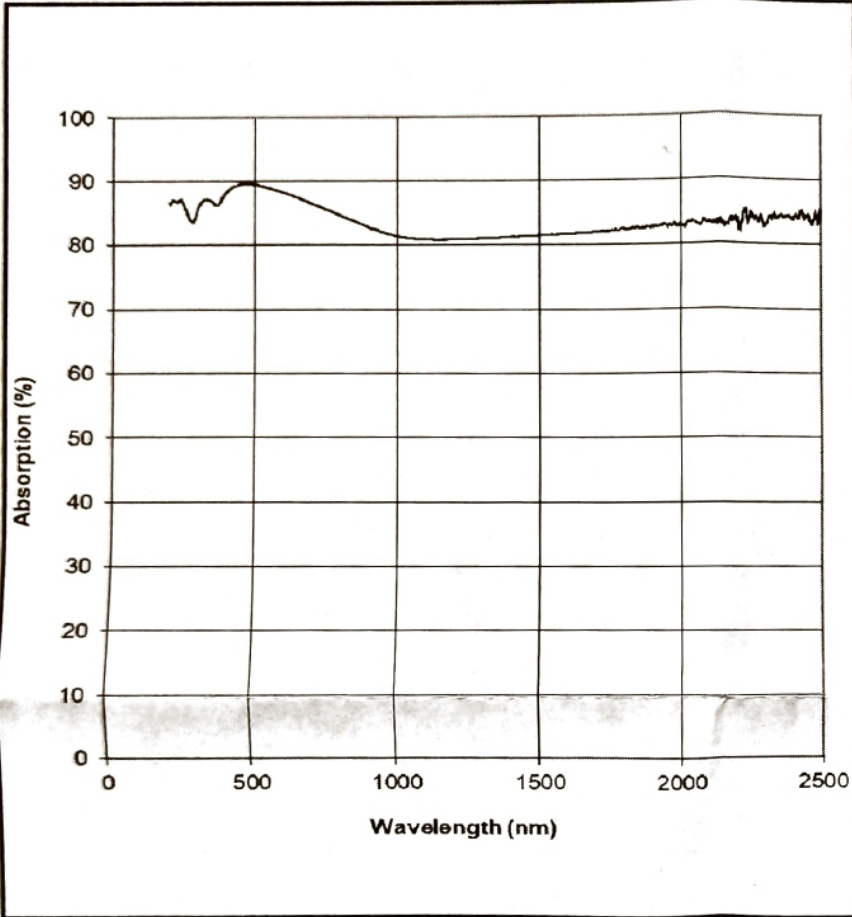
190059 Rev AZ
ACI-4026



Personal wavelength correction™ Certificate

Spectral Absorption Plot measured for: UP55N-300F-H12-BLU-D0 Power Detector

Serial #308803



Personal Wavelength Correction™		
Measurement Condition	Calibration Data	
Wavelength (nm)	Multiplier	Uncertainty
193	0.943	N/A
213	0.930	N/A
248	0.936	± 2.5 %
266	0.959	± 2.5 %
308	0.934	± 1.0 %
337	0.930	± 1.0 %
355	0.935	± 1.0 %
488	0.904	± 1.0 %
514	0.906	± 1.0 %
532	0.908	± 1.0 %
578	0.915	± 1.0 %
632	0.923	± 1.0 %
694	0.935	± 1.0 %
720	0.940	± 1.0 %
810	0.959	± 1.0 %
980	0.992	± 1.0 %
1064 *	1.000	N/A
1550	0.992	± 1.0 %
2100	0.973	± 1.0 %
10600 **	0.944	N/A

* Calibration wavelength
 ** Typical value

Adjustment multiplier for wavelength under 248 nm are not traceable.

For Gentec-EO monitors, select the proper wavelength in menu

For other monitors, multiply by the correction multiplier
 Power corrected = Power read x correction multiplier
 Example: Power (720 nm) = 10mW x 0.94 = 9.4 mW

Test Equipment and Standards Used

ID#	Description	Serial#	Last Cal.	By	Certificate #
EOC-1102	Varian, CARY 5000, Spectrophotometer	NY1605001	N/A	N/A	N/A
EOCE-223	Labsphere, Spectralon Reflectance Standard 5%	05AA01-1115-4910	Jul. 11, 2022	NRC-CNRC	PAR-2022-3900
EOCE-224	Labsphere, Spectralon Reflectance Standard 20%	20AA-0-0116-4909	Jul. 11, 2022	NRC-CNRC	PAR-2022-3900

Declaration of Conformity

Gentec Electro-Optics, Inc. certifies that, at the time of calibration, the above listed instrument meets or exceeds all specifications. It has been calibrated using standards traceable to the International System of Units (SI) through the National Institute of Standards and Technology (NIST), the National Research Council Canada (NRC) or other National Metrology Institutes. Calibration results relate only to the instrument being calibrated. Calibration activities are compliant to ISO 9001 : 2015 and ISO/IEC 17025 : 2017. Total expanded uncertainties are reported with a coverage factor k=2, providing a level of confidence of approximately 95%. Any statement of compliance is made without taking measurement uncertainty into account and is based on the instrument's uncertainty.

Signature _____

 Signature _____

BRUNO RENAUD
 Calibrated by
 Charles Lalancette
 Quality Assurance

February 22, 2023
 Date of Issue
 Feb 27 2023
 Date of Inspection

No reproduction of this document is permitted except in full

CALIBRATION CERTIFICATE



Model: 113B28
Serial #: LW41871
Description: Pressure Sensor
Type: ICP

Time Constant: 2.4 sec

Date: 5/6/2019
By: William Swanson, Cal. Tech.
Station: 903 Pulse #3 (Test procedure AT601-6)

Sensitivity*: 103.0 mV/PSI
 14.94 mV/kPa

Temp: 76 deg F [24deg C]
Humidity: 40 %

Linearity*: 0.3% FS
Uncertainty:** +/- 1 %

Cert #: 748769

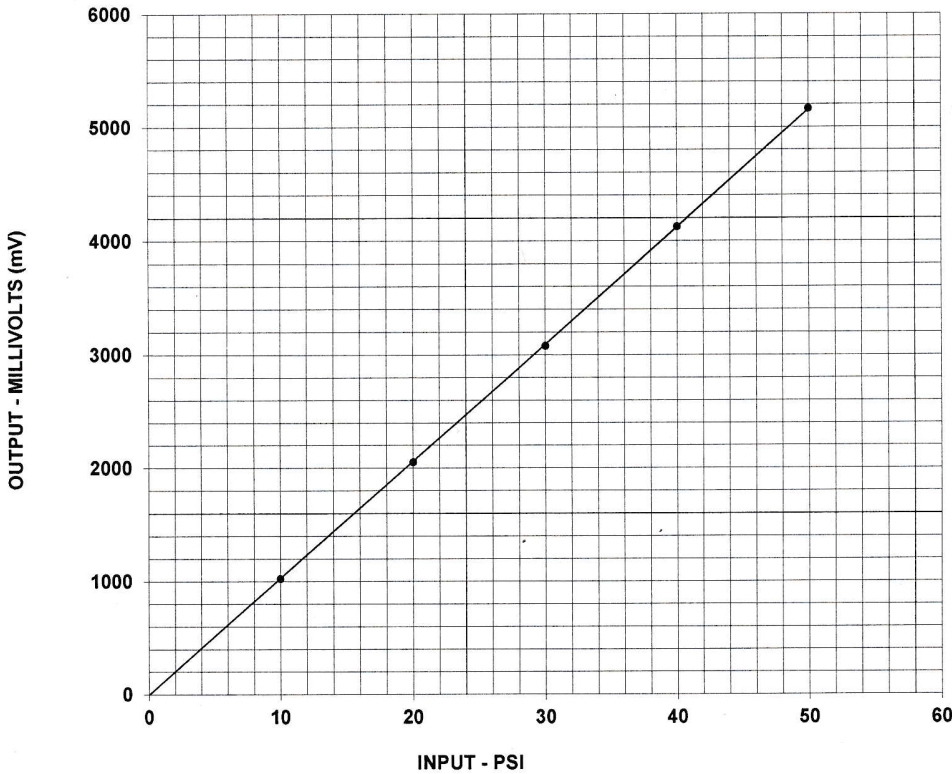
Bias: 14.8 VDC

* Zero based, least-squares straight line.

** Measurement uncertainty represented using a coverage factor of k=2 which provides a level of confidence of approximately 95 %.

Condition of Unit:

As Found: Not applicable
As Left: In tolerance, new unit



TEST DATA

INPUT (PSI)	OUTPUT (mV)
10.0	1027
20.0	2051
30.0	3078
40.0	4124
50.0	5163

Notes:

- 1 STATION #17
- 2 Calibration is traceable to NIST and is in compliance with ISO 17025 and ANSI/NCSL Z540.3.
- 3 NIST traceability through PCB control # CA 1296.
- 4 This certificate may not be reproduced, except in full, without written approval from PCB Piezotronics, Inc.



Tel: 716-684-0001 Fax: 716-684-0987 Email: sales@pcb.com
 3425 Walden Avenue, Depew NY 14043

Appendix F

Calculation examples

F.1 Absorption coefficient

Calculation of the absorption coefficient α of an argon plasma for 1070-nm radiation at a temperature T of 15 000 K and a pressure p of 10 bar.

Givens

$$\begin{aligned}E_{\text{ion}} &= 15.76 \text{ eV} \\p &= 10 \times 10^5 \text{ Pa} \\T &= 15\,000 \text{ K} \\\lambda &= 1.07 \times 10^{-6} \text{ m}\end{aligned}$$

F.1.1 Electron density calculation

We begin with the calculation of electron density n_e , using the Saha ionization equation:

$$\frac{n_e^2}{n_0 - n_e} = \frac{n_e^2}{n_{\text{Ar}}} = \frac{2}{\Lambda_{\text{th}}^3} \frac{\mathcal{Z}_{\text{Ar}^+}}{\mathcal{Z}_{\text{Ar}}} \exp\left(-\frac{E_{\text{ion, Ar}}}{k_B T}\right) \quad (4.1 \text{ revisited})$$

Calculating necessary parameters: the thermal DeBroglie wavelength Λ_{th} , the initial atomic number density n_0 , the partition function ratio $\mathcal{Z}_{\text{Ar}^+}/\mathcal{Z}_{\text{Ar}}$ (from NIST), and the ionization energy E_{ion} in J.

$$\Lambda_{\text{th}} = \sqrt{\frac{2\pi\hbar^2}{m_e k_B T}} = \sqrt{\frac{2\pi(1.05457 \times 10^{-34} \text{ J s})^2}{(9.10938 \times 10^{-31} \text{ kg})(1.38065 \times 10^{-23} \text{ J K}^{-1})(15\,000 \text{ K})}}$$
$$\Lambda_{\text{th}} = 6.0860 \times 10^{-10} \text{ m}$$

$$n_0 = \frac{N_A p}{R_u T} = \frac{(6.02214 \times 10^{23} \text{ mol}^{-1})(10 \times 10^5 \text{ Pa})}{(8.31446 \text{ J K}^{-1} \text{ mol}^{-1})(15\,000 \text{ K})}$$
$$n_0 = 4.8286 \times 10^{24} \text{ m}^{-3}$$

$$\frac{\mathcal{Z}_{\text{Ar}^+}}{\mathcal{Z}_{\text{Ar}}} = \frac{(5.74)}{(1.02)}$$

$$\frac{\mathcal{Z}_{\text{Ar}^+}}{\mathcal{Z}_{\text{Ar}}} = 5.627$$

$$E_{\text{ion}} = (15.76 \text{ eV}) \left(\frac{1.60218 \times 10^{-19} \text{ J}}{1 \text{ eV}} \right)$$

$$E_{\text{ion}} = 2.5250 \times 10^{-18} \text{ J}$$

Evaluating Equation 4.1 with the above parameters then yields the ratio $n_e^2/(n_0 - n_e)$, which will be represented by S for convenience:

$$\frac{n_e^2}{n_0 - n_e} = S = \frac{2(5.627)}{(6.0860 \times 10^{-10} \text{ m})^3} \exp \left(-\frac{(2.5250 \times 10^{-18} \text{ J})}{(1.38065 \times 10^{-23} \text{ J K}^{-1})(15000 \text{ K})} \right)$$

$$\frac{n_e^2}{n_0 - n_e} = S = 2.5308 \times 10^{23} \text{ m}^{-3}$$

The electron density can then be determined by solving the quadratic equation:

$$\frac{n_e^2}{n_0 - n_e} = S \implies n_e^2 + Sn_e - Sn_0 = 0$$

$$n_e = \frac{-S + \sqrt{S^2 - 4(-Sn_0)}}{2}$$

$$n_e = 9.8612 \times 10^{23} \text{ m}^{-3} = 9.8612 \times 10^{17} \text{ cm}^{-3}$$

F.1.2 Absorption coefficient

For convenience, the IB absorption coefficient α formula is reproduced here, yielding a result in m^{-1} :

$$\alpha = \frac{7.8 \times 10^{-7} Z n_e^2 \ln \Lambda}{\nu^2 (k_B T_e)^{3/2}} \left(1 - \frac{\nu_p^2}{\nu^2} \right)^{-1/2} \quad [\text{m}^{-1}] \quad (2.2 \text{ revisited})$$

It should be noted, again, that this form of the absorption coefficient expression is only valid with n_e in cm^{-3} and $k_B T_e$ in eV (i.e., 1.293 eV). The Coulomb logarithm can be computed first—both approaches discussed in Section 4.1 will be performed to compare their results. First is the following approximation, with n_e [cm^{-3}] and $T_{E,e}$ [eV]:

$$\begin{aligned} \ln \Lambda &= 23 - \ln (n_e^{1/2} Z T_{E,e}^{-3/2}) \\ &= 23 - \ln ((9.8612 \times 10^{17} \text{ cm}^{-3})^{1/2} (1)(1.293 \text{ eV})^{-3/2}) \end{aligned}$$

$$\ln \Lambda = 2.669$$

The alternate evaluation of the Coulomb logarithm is that of Johnston and Dawson [27]:

$$\ln \Lambda = \ln \left(\frac{v_T}{\max(\nu, \nu_p) \rho_{\min}} \right)$$

$$\nu_T = \sqrt{\frac{k_B T}{m_e}} = \sqrt{\frac{(1.380\,65 \times 10^{-23} \text{ J K}^{-1})(15\,000 \text{ K})}{(9.109\,38 \times 10^{-31} \text{ kg})}}$$

$$\nu_T = 476\,800 \text{ m s}^{-1}$$

Figure 4.2a already showed that the laser frequency ν is much greater than the plasma frequency ν_p , but both will be compared here explicitly for completeness.

$$\nu = \frac{c}{\lambda} = \frac{(2.997\,92 \times 10^8 \text{ m s}^{-1})}{(1.07 \times 10^{-6} \text{ m})}$$

$$\nu = 2.80 \times 10^{14} \text{ s}^{-1}$$

$$\nu_p = \frac{1}{2\pi} \sqrt{\frac{e^2}{\epsilon_0 m_e}} \sqrt{n_e} = (8978.85 \text{ cm}^{3/2} \text{ s}^{-1}) \sqrt{(9.8612 \times 10^{17} \text{ cm}^{-3})}$$

$$\nu_p = 8.92 \times 10^{12} \text{ s}^{-1}$$

$$\max(\nu, \nu_p) = \max((2.80 \times 10^{14} \text{ s}^{-1}), (8.92 \times 10^{12} \text{ s}^{-1}))$$

$$\max(\nu, \nu_p) = 2.80 \times 10^{14} \text{ s}^{-1}$$

The minimum impact parameter ρ_{\min} for electron-ion collisions is calculated as follows:

$$\rho_{\min} = \max\left(\frac{Ze^2}{k_B T}, \frac{\hbar}{\sqrt{m_e k_B T}}\right)$$

$$\frac{Ze^2}{k_B T} = \frac{(1)(1.602\,18 \times 10^{-19} \text{ C})^2}{(1.380\,65 \times 10^{-23} \text{ J K}^{-1})(15\,000 \text{ K})}$$

$$\frac{Ze^2}{k_B T} = 1.239 \times 10^{-19} \text{ m}$$

$$\frac{\hbar}{\sqrt{m_e k_B T}} = \frac{(1.054\,57 \times 10^{-34} \text{ J s})}{\sqrt{(9.109\,38 \times 10^{-31} \text{ kg})(1.380\,65 \times 10^{-23} \text{ J K}^{-1})(15\,000 \text{ K})}}$$

$$\frac{\hbar}{\sqrt{m_e k_B T}} = 2.428 \times 10^{-10} \text{ m}$$

$$\rho_{\min} = \max\left(\frac{Ze^2}{k_B T}, \frac{\hbar}{\sqrt{m_e k_B T}}\right) = \max((1.239 \times 10^{-19} \text{ m}), (2.428 \times 10^{-10} \text{ m}))$$

$$\rho_{\min} = 2.428 \times 10^{-10} \text{ m}$$

With this, the Coulomb logarithm evaluates to:

$$\ln \Lambda = \ln\left(\frac{\nu_T}{\max(\nu, \nu_p) \rho_{\min}}\right) = \ln\left(\frac{(476\,800 \text{ m s}^{-1})}{(2.80 \times 10^{14} \text{ s}^{-1})(2.428 \times 10^{-10} \text{ m})}\right)$$

$$\ln \Lambda = 1.948$$

Either approach for evaluating the logarithm can be taken. Although their result differs by 37% in this case, the discrepancy decreases at higher temperatures, and the discrepancy's effect on the peak absorption coefficient is no greater than 10% on both the temperature at which the peak occurs and the value of the peak. The absorption coefficient α can now be calculated:

$$\begin{aligned}\alpha &= \frac{7.8 \times 10^{-7} Z n_e^2 \ln \Lambda}{\nu^2 (k_B T_e)^{3/2}} \left(1 - \frac{\nu_p^2}{\nu^2}\right)^{-1/2} \\ &= \frac{7.8 \times 10^{-7} (1) (9.8612 \times 10^{17} \text{ cm}^{-3})^2 \ln \Lambda}{(2.80 \times 10^{14} \text{ s}^{-1})^2 (1.239 \text{ eV})^{3/2}} \left(1 - \frac{(8.92 \times 10^{12} \text{ s}^{-1})^2}{(2.80 \times 10^{14} \text{ s}^{-1})^2}\right)^{-1/2} \\ &= (7.019 \text{ m}^{-1}) \ln \Lambda \\ \alpha &= \begin{cases} 18.7 \text{ m}^{-1} & \text{for } \ln \Lambda = 2.669 \\ 13.7 \text{ m}^{-1} & \text{for } \ln \Lambda = 1.948 \end{cases}\end{aligned}$$

Appendix G

LSP shot procedure

This procedure was published as a living document on a collaboration platform accessible to personnel associated with this project. It is reproduced here in its most up-to-date state at the time of publication.

LSP Shot Procedure

This checklist is used for starting up, using, then shutting down the Laser-Sustained Plasma (LSP) experiment to perform an LSP test. This checklist assumes the laser has already been aligned.

Not all components are used for all experiments (e.g., spark-igniter). Avoid setting them up if not necessary.

STARTUP PROCEDURE

1. Power on triggering and monitoring station
 1. Turn on delay generators, oscilloscope
 2. Oscilloscope trigger should be set to “Normal” mode
 3. Turn on laser in LOCAL mode
 4. Verify that timing delays have the correct value **and** unit (ms)
 5. Verify that delay generators, camera, and laser are connected according to wiring diagram
2. Setup camera
 1. Turn on camera
 2. Connect to camera using Yellow Cat 6 cable
 3. Start PFV4 software and acquire live camera feed
 4. Calibrate sensor
 5. Remove lens cap

G. LSP SHOT PROCEDURE

6. Attach ND Filter and UV-IR Cut Filter to lens
 7. Adjust camera position and focus to frame the LSP ignition point (spark-plug tips) at a 300 mm focal length
 - i** Use low-light mode, set the lens aperture to f/4, set the ND Filter to minimum, and use additional lighting if needed
 8. Turn off low-light mode, set the camera frame rate to 10000 fps
 9. Set the aperture to f/22 and the ND filter to the maximum level
3. Setup power meter
 1. The black rubber protective cap should be on
 2. Plug in the power meter's fan power supply and ensure the fan is running
 3. Turn on the BLU emitter (blue button)
 4. Connect to the power meter on the PC Gentec-EO software using the Bluetooth dongle (attached to blue USB extension cord)
 - i** For best results, leave the Bluetooth dongle within the test area
 5. Remove the black rubber protective cap and allow the power meter's signal to stabilize
 6. Set the wavelength to 1070 nm and perform the zeroing procedure
 7. Set the power meter to "SSE (J)" (Single Shot Energy) mode
 8. Suggested: set the display mode to "Statistics"
 9. If applicable, set your acquisition settings (filename, etc.)
 4. Setup spectrometer
 1. Use a laser pointer and a 100 micron fiber attached to the fiber mount to ensure the fiber tip is pointed at the ignition point, then re-attach the spectrometer fiber (10 micron) to the fiber mount
 2. Connect to the spectrometer via USB and start the OceanView Lite software, in "Quick View" mode
 3. Click "Create dark background spectrum"
 4. Set the integration time to 4 ms and the trigger mode to "Edge"
 5. Setup pressure transducer
 1. If the transducer is already mounted, all that is needed is to turn on the signal conditioner and check that the Channel 1 indicator is green
 6. Prepare test area
 1. Ensure the laser protection panels (2) are installed over the beam path between the collimator and the test section
 2. Ensure that the collimator cap is **OFF** and no obstacle is present in the beam path. Use the guide laser to check.

G. LSP SHOT PROCEDURE

3. Pressurize the test section to the target pressure. If performing a flowing test, pressurize the feed lines upstream of the solenoid valve, and set the valve's safety switch to the FIRE mode

i Before pressurizing to target pressure, flush the air from the test section by filling it with argon to 5 bar then venting it to 1.5 bar, repeating this process three times.

⚠ The laser windows are rated for a maximum internal pressure of 20 bar. Do not exceed this pressure. Some tolerance for overpressure (~1 bar) is available in order to let the system stabilize to 20 bar, but do not run tests in overpressure conditions. *Destructive testing has not been performed to determine the actual failure pressure.*

4. Plug in the spark igniter to the mains

⚠ The igniter is now ON and will spark when receiving a signal

5. Exit the area enclosed by the laser safety curtains and close them

The experiment is now ready to be run.

RUNNING THE EXPERIMENT

1. Perform a final check on the control station to verify the timings and connections of the delay generators, oscilloscope, and laser.
2. Prepare the laser
 1. Restart the laser in REMOTE mode
 2. Connect to the laser via the router, using the Black Cat 6 cable
 3. Use the laser's web interface to set up the pulse. Check the following settings:
 - HW Emission Control should be ENABLED
 - Pulse Mode should be ENABLED**i** For more information on the web interface, consult the laser user guide
 4. Set the pulse power setpoint to the desired value
 5. Set the pulse duration to the desired value
3. Connect to camera using Yellow Cat 6 cable, and confirm connection in PFV4
4. Click "Record" in PFV4. The button should read "Ready"
5. Set the spectrometer save settings by clicking "Configure graph saving" in OceanView, entering the appropriate LSP shot identifier code as the BaseName, click "Apply"
6. Click the "Save graph to files" icon in OceanView—this should turn the button red.
7. **All personnel present in the laboratory**, regardless of their involvement in the experiment, must be equipped with laser safety goggles rated for 1070 nm beyond this step

G. LSP SHOT PROCEDURE

8. Turn on the laboratory's laser warning light (confirm visually) and ensure the door is closed
 - **Entering/exiting the laboratory is not permitted beyond this step**
9. Disengage the laser's front-panel E-stop. Call out "Safety OFF".
10. Find the power supply switch wired in the back of the laser. Flick the switch ON then OFF. Call out "Laser is ARMED".
 - **This starts the laser's main power supply, this is indicated by a louder fan volume and the green button on the front panel being lit up**
 - ⚠ **The laser is now armed** - it will emit a laser pulse when the trigger signal is active
11. The experiment is ready to run, go through the following checklist before firing:
 - Curtains are **CLOSED**
 - Laboratory warning light is **ON**
 - Laser is **ARMED**
 - Camera is **READY**
 - Power meter monitor is active and awaiting pulses
 - All delay generators are **ON**
 - Oscilloscope is **ON**
 - ALL LAB PERSONNEL IS WEARING LASER SAFETY GOGGLES**
12. If performing a flowing test, use the valve switch near the control station to initiate flow. Allow for 5 seconds for the flow to stabilize, or up to 45 seconds for the pressure transducer signal to return to 0.
13. You may press the MAN TRIG button to emit a laser pulse. Watch the ceiling above the test area to spot the flash of a successful LSP ignition
14. Press the front panel E-stop to safe the laser. Call out "SAFE".
15. Regardless of ignition, the camera will have recorded footage. To perform a new shot, resume from step 4

■ **If at any point after step 6, someone must remove their safety glasses, enter, or leave the lab, press the E-stop to safe the laser. Resume procedure from step 5.**

SHUTDOWN PROCEDURE

1. Press the laser's front-panel E-stop
 - **Laboratory personnel is now free to remove their laser safety glasses, and can freely enter/leave the lab**
2. Disable laser warning light
3. Open the laser safety curtains
4. Unplug the igniter

G. LSP SHOT PROCEDURE

5. Vent the test section
6. Shut off the camera
7. Shut off the power meter, unplug its fan, and place the rubber protective cap back on
8. Screw on the collimator cap
9. Switch off the delay generators and the oscilloscope
10. Switch off the laser, place the keys in the “Miscellaneous” drawer of the component cabinet

Appendix H

Laser Pulse Shapes

Table H.1 tabulates the various programmed stepped-pulse shapes used in this project, including their total energy and precise duration.

Table H.1: Programmed pulse specifications. The symbol n_{sp} is the laser setpoint; t , t_{high} , and t_{low} are the total pulse, high setpoint, and low setpoint durations, respectively; and E is the pulse energy.

ID	High n_{sp} [-]	Low n_{sp} [-]	t [ms]	t_{high} [ms]	t_{low} [ms]	E [J]
1L7_15	1.000	0.070	15.001	0.997	14.004	6.086
1L10_15	1.000	0.100	15.001	0.997	14.004	7.369
1L20_15	0.999	0.200	15.739	0.997	14.742	12.148
05L7_15	0.999	0.070	15.239	0.497	14.742	4.704
05L8.5_15	0.999	0.085	15.239	0.497	14.742	5.388
05L10.5_15	1.000	0.105	15.242	0.497	14.746	6.297
05L10_15	1.000	0.100	15.242	0.497	14.746	6.056
05L11_15	1.000	0.113	15.242	0.497	14.746	6.667
05L13_15	1.000	0.129	15.242	0.497	14.746	7.408
05L16_15	1.000	0.162	15.239	0.497	14.742	8.868
05L17.8_15	1.000	0.178	15.239	0.497	14.742	9.609
05L20_15	1.000	0.200	15.239	0.497	14.742	10.608
05L33_15	1.000	0.330	15.239	0.497	14.742	16.512
05L50_15	0.999	0.500	15.239	0.497	14.742	24.229
05L67_14	1.000	0.670	14.000	0.497	13.504	29.392
05L80_12	0.999	0.800	11.999	0.497	11.502	29.868

Appendix I

Properties of relevant substances

The thermodynamic and mechanical properties (at 290 K and 1 bar) of substances relevant to this project are tabulated below for convenience.

Table I.1: Thermodynamic and mechanical properties of selected substances. The density ρ , specific heats at constant volume c_V and pressure c_p , thermal conductivity k , molar mass \mathcal{M} , yield strength σ_y , and melting point T_{melt} are provided.

	Argon	304 Steel	6061-T6 Aluminum	Tungsten	Unit
ρ	1.66	8000	2700	19 300	kg m^{-3}
c_V	312	-	-	-	$\text{J kg}^{-1} \text{K}^{-1}$
c_p	522	500	896	132	$\text{J kg}^{-1} \text{K}^{-1}$
k	0.0173	16.2	167	163	$\text{W m}^{-1} \text{K}^{-1}$
\mathcal{M}	39.9	-	-	184	kg kmol^{-1}
σ_y	-	215	276	750	MPa
T_{melt}	83.8	1700	890	3700	K
Reference	[1]	[2]	[3]	[4, 5]	

- [1] E. W. Lemmon, I. H. Bell, M. L. Huber, and M. O. McLinden, "Thermophysical Properties of Fluid Systems," in *NIST Chemistry WebBook, NIST Standard Reference Database Number 69*, P. J. Linstrom and W. G. Mallard, Eds., Gaithersburg, MD: National Institute of Standards and Technology, 2023. [Online]. Available: <https://doi.org/10.18434/T4D303>.
- [2] MatWeb. "304 Stainless Steel," Online Materials Information Resource - MatWeb. (), [Online]. Available: <https://www.matweb.com/search/datasheet.aspx?MatGUID=abc4415b0f8b490387e3c922237098da> (visited on 2023-12-13).
- [3] Aerospace Specification Metals Inc and MatWeb. "ASM Material Data Sheet," Online Materials Information Resource - MatWeb. (), [Online]. Available: <https://asm.matweb.com/search/SpecificMaterial.asp?bassnum=ma6061t6> (visited on 2023-12-13).
- [4] Royal Society of Chemistry. "Tungsten - Element information, properties and uses | Periodic Table," Periodic Table - Royal Society of Chemistry. (2023), [Online]. Available: <https://www.rsc.org/tudelft.idm.oclc.org/periodic-table/element/74/tungsten>.
- [5] MatWeb. "Tungsten, W," Online Materials Information Resource - MatWeb. (), [Online]. Available: https://www.matweb.com/search/datasheet_print.aspx?matguid=41e0851d2f3c417ba69ea0188fa570e3 (visited on 2023-12-13).